**Brownian Dynamics Study on Ferrofluids using Iterative Constraints
to Satisfy Maxwell's Equations**

BY

SEAN HYUN DUBINA
B.S., University of Maryland, 2009

THESIS

Submitted as partial fulfillment of the requirements
for the degree of Doctor of Philosophy in Chemical Engineering
in the Graduate College of the
University of Illinois at Chicago, 2017

Chicago, Illinois

Defense Committee:

       Lewis E. Wedgewood, Chair and Advisor
       Ludwig C. Nitsche
       Vivek Sharma
       Ying Liu
       Andrew Tillotson, New York University Abu Dhabi

This thesis is dedicated in memory of my grandparents, Dr. Patrick and Mrs. Rosemarie Ahern, who actively fostered education in their community as well as their family.

ACKNOWLEDGMENTS

TABLE OF CONTENTS

TABLE OF CONTENTS (continued)

LIST OF TABLES

LIST OF FIGURES

LIST OF SYMBOLS

Fluid Properties

ρ	Density
$\boldsymbol{g}$	Gravitational acceleration
p	Pressure
η	Viscosity of the fluid
η^{m}	Spin viscosity contribution
$\dot{\gamma}$	Shear rate of the ambient fluid
k	Boltzmann's constant
T	Absolute temperature of the fluid

Brownian Particle Parameters

m_w	Mass of a Brownian particle
a	Radius of particle including the steric layer
a_s	Radius of particle excluding the steric layer
d	Diameter of particle including the steric layer
d_s	Diameter of particle excluding the steric layer
δ	Thickness of the steric layer
n_s	Quantity of surfactant constituents per unit area on particle surfaces

Energies, Forces, and Torques

$E_{\alpha\beta}^{\mathrm{m}}$	Energy of particle-particle interactions
$E_{\alpha\beta}^{\mathrm{v}}$	Energy of steric interactions
E_{α}^{h}	Energy of particle-field interactions
$\boldsymbol{F}_{\alpha\beta}^{\mathrm{m}}$	Magnetic force acting on particle α by nearby particles β
$\boldsymbol{T}_{\alpha\beta}^{\mathrm{m}}$	Magnetic torque acting on particle α by nearby particles β
$\boldsymbol{F}_{\alpha\beta}^{\mathrm{v}}$	Steric force due to overlapping of particle α by particles β
$\boldsymbol{F}_{\alpha}^{\mathrm{h}}$	Force on particle α by the applied magnetic field
$\boldsymbol{T}_{\alpha}^{\mathrm{h}}$	Torque due to deviation of particle α from the applied magnetic field
$\boldsymbol{F}_{\alpha}^{\mathrm{P}}$	Force of particle α acting on the surrounding fluid
$\boldsymbol{T}_{\alpha}^{\mathrm{P}}$	Torque of particle α acting on the surrounding fluid
$\boldsymbol{F}_{\alpha}^{\mathrm{f}}$	Force of the surrounding fluid on particle α
$\boldsymbol{T}_{\alpha}^{\mathrm{f}}$	Torque of the surrounding fluid acting on particle α
$\boldsymbol{F}_{\alpha}^{\mathrm{b}}$	Force of the Brownian motion of particle α
$\boldsymbol{T}_{\alpha}^{\mathrm{b}}$	Torque of the Brownian motion of particle α

Brownian Parameters

$\Delta\boldsymbol{v}_{\alpha}^{\mathrm{B}}$	Brownian velocity of particle α
$\Delta\boldsymbol{r}_{\alpha}^{\mathrm{B}}$	Brownian displacement of particle α
$\Delta\boldsymbol{\omega}_{\alpha}^{\mathrm{B}}$	Brownian angular velocity of particle α
$\Delta\boldsymbol{\varphi}_{\alpha}^{\mathrm{B}}$	Brownian rotation of particle α
$\boldsymbol{r}_n$	Randomly-generated position vector

Particle Diffusion Properties

$\boldsymbol{r}_\alpha$	Position vector of particle α
$\boldsymbol{r}_{\alpha\beta}$	Position vector from particle α to particle β
$\boldsymbol{d}_{\alpha\beta}$	Unit direction vector from particle α to particle β
$\boldsymbol{m}_\alpha$	Magnetic dipole moment of particle α
$\boldsymbol{n}_\alpha$	Dipole moment vector of particle α
$\boldsymbol{\varphi}_\alpha$	Dipole orientation of particle α
$\boldsymbol{v}_\alpha$	Velocity vector of particle α
$\boldsymbol{v}_\alpha^\infty$	Velocity vector of particle α in the absence of particle β
$\boldsymbol{v}_{\alpha\beta}$	Velocity vector of particle α affected by particle β
$\boldsymbol{\omega}_\alpha$	Angular velocity of particle α

Hydrodynamic Properties

$\mathbf{E}$	Rate-of-strain tensor
$\boldsymbol{\Delta}^\infty$	Symmetric part of the rate-of-strain tensor
$\mathbf{a}$	Second-rank tensor of the mobility tensor
$\mathbf{b}$	Second-rank tensor of the mobility tensor
$\mathbf{c}$	Second-rank tensor of the mobility tensor
$\mathbf{g}$	Third-rank tensor of the mobility tensor
$\mathbf{h}$	Third-rank tensor of the mobility tensor
$\mathbf{k}$	Fourth-rank tensor of the mobility tensor
$\mathbf{M}$	Mobility matrix
$\widehat{\mathbf{M}}$	Truncated mobility matrix
$\boldsymbol{S}$	Stresslet tensor
$\boldsymbol{F}$	Force exerted on the fluid by a particle
$\boldsymbol{T}$	Torque exerted on the fluid by a particle
$\boldsymbol{U}$	Velocity of the fluid in the absence of particles
$\boldsymbol{\Omega}$	Angular velocity of the fluid in the absence of particles
$x_{\alpha\beta}^{\mathrm{a}}$	Mobility function of the second-rank tensor $\mathbf{a}$
$y_{\alpha\beta}^{\mathrm{a}}$	Mobility function of the second-rank tensor $\mathbf{a}$
$y_{\alpha\beta}^{\mathrm{b}}$	Mobility function of the second-rank tensor $\mathbf{b}$
$x_{\alpha\beta}^{\mathrm{c}}$	Mobility function of the second-rank tensor $\mathbf{c}$
$y_{\alpha\beta}^{\mathrm{c}}$	Mobility function of the second-rank tensor $\mathbf{c}$
$x_{\alpha\beta}^{\mathrm{g}}$	Mobility function of the third-rank tensor $\mathbf{g}$
$y_{\alpha\beta}^{\mathrm{g}}$	Mobility function of the third-rank tensor $\mathbf{g}$
$y_{\alpha\beta}^{\mathrm{h}}$	Mobility function of the third-rank tensor $\mathbf{h}$
ξ_f	Far-field dimensionless parameter
ξ_n	Near-field dimensionless parameter
$\boldsymbol{d}$	Unit directional vector between particles α and β

Diffusivities

$\boldsymbol{D}_{\alpha\beta}$	Diffusivity tensor between particle α and particle β
$\boldsymbol{D}^{\mathrm{T}}$	Translational diffusivity tensor
$\boldsymbol{D}^{\mathrm{R}}$	Rotational diffusivity tensor
$\boldsymbol{D}^{\mathrm{C}}$	Coupled diffusivity tensor
D_0	Diffusion coefficient at infinite dilution
D_0^t	Translational diffusion coefficient at infinite dilution
D_0^r	Rotational diffusion coefficient at infinite dilution

Quaternion Properties

$\boldsymbol{A}$	Rotation matrix
$\boldsymbol{V}_{\mathrm{principal}}$	Principal velocity vector
$\boldsymbol{V}_{\mathrm{lab}}$	Lab velocity vector
χ	Quaternion parameter
μ	Quaternion parameter
κ	Quaternion parameter
ζ	Quaternion parameter
θ	Goldstein Euler angles
ψ	Goldstein Euler angles
ϕ	Goldstein Euler angles
$\boldsymbol{\omega}_p$	Principal angular velocity

Cutoff and Wall Parameters

r_{coff}	Cutoff radius/distance for particle-particle interactions
$r_{\mathrm{coff}}^{(\mathrm{hydro})}$	Cutoff radius for hydrodynamic interactions
$\Delta\boldsymbol{r}_\alpha$	Overlap adjustment for particle α
$r_{w\alpha}$	Distance between wall particle w and particle α
r_{over}	Overlap displacement of particle α over wall particle w
Δr_{min}	Minimum distance from the center of a particle to the center of a wall particle
$\boldsymbol{d}_{w\alpha}$	Unit direction vector from wall particle w to particle α
N_w	Total number of w wall particles

Simulation Parameters

L	Length of a side of the cubic simulation volume
L_{c}	Length of a side of the local cubic constraint volumes
N	Total number of particles in the system
t	Simulation time
Δt	Time-step
N_t	Number of elapsed time-steps

LIST OF SYMBOLS (continued)

Properties of Magnetism

μ_0	Permeability of free space
K_m	Relative permeability of material
χ_m	Magnetic susceptibility of material
$\boldsymbol{B}$	Induction field
$\boldsymbol{M}$	Magnetization
$\boldsymbol{M}_S$	Saturation magnetization
h	Cutoff radius of particle contribution to the local field $\boldsymbol{M}$
W	Radial weighting function
$\boldsymbol{H}$	Magnetic field
$\boldsymbol{H}_0$	Externally-applied magnetic field
$\widehat{\boldsymbol{H}}$	Demagnetizing field
$\boldsymbol{e}_i$	Unit directional vector with direction index i
C_L	Constant for non-uniform $\boldsymbol{H}_0$ field
C_x	Constant for non-uniform $\boldsymbol{H}_0$ field
C_y	Constant for non-uniform $\boldsymbol{H}_0$ field

Properties of Magnetophoresis and Magnetic Separation

ρ_c	Particle number density
Φ	Separation efficiency
t_S	Separation time

General Constraint Properties

σ_j	Holonomic constraint j
d'	Total number of holonomic constraints
γ_j	Lagrange multiplier of constraint σ_j
$\tilde{G}_{jl}$	Modified metric matrix of dimension $d' \times d'$
$\tilde{g}_{jl}$	Metrix matrix of dimension $d' \times d'$
$\boldsymbol{q}_\alpha^{\text{UN}}$	Unconstrained generalized coordinate vector of particle α
$\boldsymbol{q}_\alpha^{\text{CON}}$	Constrained generalized coordinate vector of particle α
$\boldsymbol{r}_\alpha^{\text{UN}}$	Unconstrained center of mass position vector of particle α
$\boldsymbol{r}_\alpha^{\text{CON}}$	Constrained center of mass position vector of particle α
$\boldsymbol{\varphi}_\alpha^{\text{UN}}$	Unconstrained dipole orientation of particle α
$\boldsymbol{\varphi}_\alpha^{\text{CON}}$	Constrained dipole orientation of particle α
$\widehat{\boldsymbol{n}}, \boldsymbol{n}_S$	Surface normal vector
$\boldsymbol{F}_\alpha^{\text{CON,T}}$	Center of mass constraint force of particle α
$\boldsymbol{F}_\alpha^{\text{CON,R}}$	Orientational constraint force of particle α

Constraint Setup Parameters

$\boldsymbol{M}_k$	Magnetization at node k
$\boldsymbol{S}_k$	Surface area around node k
V_k	Volume containing polarized matter at node k
$\boldsymbol{H}_k$	Magnetic field at node k
$\boldsymbol{l}$	Parametrization of curve C
$\Delta\boldsymbol{l}$	Change in the linearization along C
S	Surface of a specific volume with boundary C
C	Curve enclosing surface S

Constraint Properties for Maxwell's Equations

σ_G	Constraint for Gauss's Law
σ_A	Constraint for Ampère's Law
d'_G	Number of holonomic constraints for Gauss's Law
d'_A	Number of holonomic constraints for Ampère's Law
k	Node index for Gauss's Law
k', l	Node index for Ampère's Law
N_k	Total number of k nodes
$N_{k'}$	Total number of k' nodes
$r_{k\alpha}$	Distance between node k and particle α

Dimensionless Numbers

λ	Ratio of magnetic particle-particle force to Brownian force
ξ	Ratio of the magnetic field force to Brownian force
λ_v	Value of surfactant constituents on particle surface
d_δ	Ratio of steric layer thickness δ to the radius of the solid part of the particle a_s
s_δ	Ratio of the surface-to-surface separation between two particles to the diameter of the solid part of a particle
R_m	Ratio of magnetic particle-particle force to hydrodynamic shear force
R_v	Ratio of steric repulsion force to hydrodynamic shear torque
R_h	Ratio of the magnetic field torque to hydrodynamic torque
Pe	Péclet number

Mathematic Quantities

$\boldsymbol{\delta}_i$	Unit vector with directional index i
δ_{ij}	Kronecker delta with directional indices i and j
I	Identity matrix

LIST OF ABBREVIATIONS

AIP   American Institute of Physics

FHD   Ferrohydrodynamics

HGMS   High-gradient magnetic separation

LGMS   Low-gradient magnetic separation

MP   Magnetophoresis

MR   Magnetorheological

PCF   Pair correlation function

PND   Particle number density

SUMMARY

A study on the behavior of dense suspensions of magnetic nanoscale ferroparticles was carried out by employing a particulate Brownian dynamics modeling approach with an iterative constraint method that ensured that the magnetostatic forms of Maxwell's equations (i.e. Gauss's Law and Ampère's Law) were continuously met while the suspension progresses. FORTRAN simulations were executed under varying parameter groups to observe a collection of hundreds of magnetic particles with fixed orientation dipoles leading up to and at steady-state. These parameter groups controlled the forces of particle-particle interactions, shearing, steric repulsion, and Brownian fluctuations that individual ferroparticles could experience. Effects from magnetic fields and hydrodynamic interactions were also included to induce realistic ferrofluid behavior.

Testing under uniform magnetic fields with activated constraints exhibited reduced trends in the spin viscosity when compared to trials that disregarded the constraint algorithm. Although the dispersion activity developed similarly in both cases, the chaining ultimately progressed to a lesser extent in the constraint model than in the unconstrained. Consequently, separation due to magnetic field gradients occurred at a decreased rate under the constraint method, since cooperative magnetophoresis is less effective due to weakened magnetoviscous effects. Thus, aggregation and magnetic separation modeling of ferrofluid colloidal suspensions without adherence to Maxwell's equations is inaccurate.

1. INTRODUCTION

1.1 <u>**Ferrofluids and the Study of Ferrohydrodynamics**</u>

The study of ferrohydrodynamics (FHD) began in the 1960's and is concerned with "the mechanics of fluid motion influenced by strong forces of magnetic polarization" (Rosensweig, 1985), notably in systems without induced electric currents. The novel idea of a magnetic fluid arose when scientists of the National Aeronautics and Space Administration were attempting to control liquids in space. It was further motivated with the goal of extracting work from heat without using mechanical parts. As a result, colloidal magnetic fluids known as ferrofluids were developed when they were acknowledged for their vast and revolutionary uses.

A ferrofluid is a colloidal suspension composed of nanoscale (3-15 nm), ferromagnetic, single-domain particles suspended in a continuous medium called the liquid carrier, which is oftentimes a petroleum oil or water. Each particle is coated with a dispersant molecular layer that prevents undesirable or irreversible clumping, especially when there are no magnetic sources present. In constrast to a magnetorheological (MR) fluid, which consists of micron-sized particles that only become magnetized in the presence of an applied magnetic field, ferrofluids contain particles with permanently-embedded magnetic dipoles at high concentrations. A dipole is considered a pair of equal and opposite point poles (typically called the "North" and "South" domains) separated by a small distance. For most MR fluids, the magnetostatic repulsion between particles is not sufficient enough to overcome van der Waals forces and thus, irreversibly aggregate, even in the absence of applied fields. Conversely, because of the dispersant molecular layer and Brownian motion, ferrofluids do not unexpectedly clump or settle out, although small concentration gradients can result from extended exposure to a magnetic field. Micron-sized ferroparticle clusters can be synthesized by compacting numerous ferrofluidic nanoparticles into

shells composed of organic (or sometimes inorganic) materials. A typical ferrofluid, which must be artificially manufactured, is an opaque solution that contains 10^5 particles per cubic micrometer. Transmission electron microscopy is usually implemented to verify the average particle diameter or polydispersity of ferrofluid particulate suspensions. The particles can be composed of iron, nickel, cobalt, and many of their alloys. Some rare earth metals and certain intermetallics, such as gold-vanadium, are also viable options.

1.2 **Ferrofluid Applications**

Because ferrofluids have a unique response to magnetic force fields, they have been utilized in a wide range of applications. Most of the attention has been centered around the remote positioning and control of ferrofluids using external magnetic fields. A single drop of ferrofluid can be used as zero-leakage rotary seals (Schinteie *et al*., 2013), act as pressure seals and sensors (Ravaud *et al*., 2010), applied as lubricants in bearings (Kumar *et al*., 1993), piloted in the body to bring drugs to a target site (Ganguly *et al.*, 2005; Kim and Dobson, 2009), or serve as a blood tracer in noninvasive measurements of the circulatory system (Newbower, 1973). With biofunctional coatings, ferrofluidic particles can operate as transport carriers of biomaterials via magnetofection (Furlani, 2010). Microfluidic systems manipulate magnetic particles to mobilize or impede biomaterials for detection, separation, or mixing with reagents (Nguyen, 2011). Larger volumes of ferrofluid are employed in sink-float processes, where industrial scrap metals are separated using the high specific gravity imparted to a pool of ferrofluid subjected to an appropriate magnetic field. Ferrofluids can serve as detecting agents when locating magnetic domains in alloys or crystals (Lebedev *et al*., 2002; Raj *et al*., 1995) or utilized as ink for high-speed, inexpensive, silent printers (Tiberto *et al*., 2013). For gas-fluidized beds, in order to reduce the fluid mechanical

instability, ferrofluids are used to prevent the appearance of bubbles and thus, eliminate solids back mixing and gas bypassing (Rosenweig, 1995). Research on the beds has led to improved catalytic reactors (Lai *et al*., 2011; Pourjavadi *et al*., 2012), particulate filtration (Wu *et al*., 2011; Yavuz *et al*., 2009), and separation processes (Mizuno *et al*., 2013; Zeng *et al*., 2013). Other applications include function as a contrast medium in diagnostics (Arsalani *et al*., 2012; Rümenapp *et al*., 2012) or production of magnetically responsive enzyme supports and immobilized microorganisms (Chen *et al*., 2012). Increasing interest in these kinds of applications will progress towards many novel usages, especially *in vivo*.

1.3   **Purpose of Simulation**

Computational simulations have been known to model the behavior of ferrofluid systems. More specifically, particulate models are known to be effective for portraying mesoscale magnetic suspensions undergoing separation, manipulation, and assembly. A comprehensive simulation routine is conducted to model ferrofluids under shear flow in uniformly and nonuniformly applied magnetic fields based on mesh-free techniques. This procedure is based on a Brownian dynamics method and will include a constraint algorithm to ensure application of elementary physics principles that govern magnetic fluids. The proposed simulation technique will eventually have a much broader application for other means to implement ferrofluids and therefore, will have a much wider impact in understanding magnetic fluids. Results from the study will be compared to existing relevant data and will allow for a basis of validity and insight into the behavior of subcontinuum medium in the realm of FHD.

2. LITERATURE REVIEW

2.1   **<u>Fundamentals of Ferrohydrodynamics</u>**

Elementary concepts of FHD have been compiled by Rosensweig (1985). He explains that the primary type of ferrohydrodynamical magnetic fluid, termed "colloidal ferrofluid," can retain liquid fluidity in intense applied magnetic fields. A dispersant molecular layer (also known as a surfactant) prevents particles from sticking to one other, which can be due to molecular attraction between the suspended particles and the dipole-dipole interaction inherent to magnetic material. Thermal agitation inhibits settling of the particles and keeps them suspended in the liquid carrier via Brownian motion. Furthermore, because colloidal magnetic fluids are composed of solid, single-domain particles with no long-range order present amongst particles, they demonstrate a behavior known as superparamagnetism. In the absence of an applied magnetic field, superparamagnetic materials have an average particle magnetization of zero, whereas in low to moderate magnetic fields, the magnetization is much larger when compared to paramagnetism. Superparamagnetic materials, despite particle size, have found numerous usages for their separation capabilities and reusability in most systems. They provide an advantage when considering limitations due to fouling or larger magnetic sorption substances in commercial contexts (Yavuz *et al*., 2006). Within the class of superparamagnetic materials, ferromagnetic solids are comprised of domains in which each contains the magnetic moments of individual atoms that are oriented in a fixed direction. Ferromagnetic material is broken up into domains so as to obtain a minimal field energy state. Single ferrofluid particles tend to exhibit ferromagnetism. When ferromagnetic material is magnetized in one direction, the field energy becomes substantial. Even so, the domains are not permanent since it requires energy to generate boundaries that separate them. In 1928, Werner Heisenberg explained that when the spins on adjacent atoms within

domains switch from parallel to antiparallel alignment, there is a corresponding change in the electron charge distribution of the atoms that modifies the system's electrostatic energy. Ferromagnetism, in this case, would be when the spin magnetic moments, which contribute to the molecular field, are energetically more favorable when situated in a parallel configuration. Other magnetic behaviors include antiferromagnetism (occurs when there is no net magnetic moment), ferrimagnetism (unequal moments alternate from atom to atom which results in a net moment smaller than those in typical ferromagnetic materials), paramagnetism (no long-range ordering in the molecular moments), and the weakest type of magnetic behavior known as diamagnetism (molecular moments oppose the applied magnetic field). These behaviors are outlined in Table I.

TABLE I

TYPES OF MAGNETISM

Magnetic Behavior	Ordering of Atomic Moments	Examples of Material
Paramagnetism		Al, Mn, O
Ferromagnetism		Fe, Ni, Co
Antiferromagnetism		FeO, NiO, FeMn
Ferrimagnetism		Fe_3O_4, Fe_7S_8, $MnFe_2O_4$
Diamagnetism		C, H, N

2.2   <u>**Magnetism**</u>

Magnetostatic principles that govern ferrofluids can be defined by fundamental magnetic properties. Magnetic fields that can be generated by currents are typically denoted as the induction field $\boldsymbol{B}$. The induction field $\boldsymbol{B}$ has units of tesla and is sometimes called the magnetic flux density. However, when these fields pass through magnetic materials, ambiguities arise about which segment of the induction field results from external influences and which comes from the material itself. Thus, the former component of the field due to external influences is embodied by the magnetic field $\boldsymbol{H}$ and usually possesses units of amperes per meter. It indicates the driving magnetic influence from external sources within a material, independent of the material's magnetic response. In a vacuum, the $\boldsymbol{H}$-field would represent the force that acts on a north-seeking point pole. The latter component of the field is designated by the magnetization $\boldsymbol{M}$ and has the same units as $\boldsymbol{H}$. It is considered the material's magnetic response and often characterized by a volume average of magnetic particle dipoles. The most general law comparing the three field vectors is:

$$\boldsymbol{B} = \mu_0(\boldsymbol{H} + \boldsymbol{M}) \qquad [2.1]$$

Here, μ_0 is the permeability of free space. Thus, in magnetic materials, $\boldsymbol{B}$ is not solely related to $\boldsymbol{H}$ due to the magnetization term $\boldsymbol{M}$ and $\boldsymbol{B} \neq \boldsymbol{H}$. Another, widespread form of the relationship between $\boldsymbol{B}$ and $\boldsymbol{H}$ is:

$$\boldsymbol{B} = \mu_m \boldsymbol{H} \qquad [2.2]$$

where

$$\mu_m = K_m \mu_0 \qquad [2.3]$$

Here, K_m is the relative permeability of the material and assesses the ratio of magnetization to the applied magnetic field. Magnetic materials with large, positive relative permeabilities have internal magnetizations that respond well to an external magnetic field. When the field is in a vacuum or

passing through a material that does not react to the **H**-field by generating a corresponding **M**, $K_m = 1$. Relative permeability is compared to the value of 1 when using the magnetic susceptibility:

$$\chi_m = K_m - 1 \qquad\qquad\qquad [2.4]$$

The magnetic susceptibility is very close to 0 in paramagnetic and diamagnetic materials. Moreover, these quantities may be very large in ferromagnetic materials.

2.3   **Magnetophoresis and Magnetic Separation**

When nonuniform magnetic fields are applied to magnetic fluids, the magnetic material undergoes a migration phenomenon known as magnetophoresis. Magnetophoresis (MP) describes the diffusive behavior of magnetic particles when they are manipulated by a magnetic force in the presence of locally-applied magnetic field gradients. It is a central mechanism of magnetic separation techniques, which are more rapid and effective than filtration or centrifugation methods. Gradients are primarily caused by differences in magnetism (often characterized by disparities in susceptibilities). Magnetophoresis differs from electrophoresis or dielectrophoresis methods, which exploit electric currents to control electrically-conductive materials in suspensions, or electromagnetophoresis, a phenomenon that combines both magnetism and electricity with migration analysis (Watarai *et al*., 2004), and should not be confused with negative MP, which involves mixtures of nonmagnetic and magnetic particles (Liang and Xuan, 2012). When the magnetic field gradient is directed perpendicularly to the flow direction, MP occurs when the ferroparticles are driven towards explicit regions for extraction from the liquid carrier. While they move, the magnetic particles behave in one of two ways: cooperatively or noncooperatively. Cooperative MP occurs when the particle aggregation enhances the magnetic migration while

noncooperative MP involves the diffusion of individual particles. For particles in cooperative MP, they can be envisioned as inducing a magnetic gradient between themselves and the fluid. As the ferroparticles form larger colloids, they become more magnetically responsive and consequently, the thicker chains drift faster than thinner aggregates. Therefore, magnetic particle-particle effects and hydrodynamic interactions can accelerate the migration of particle chains. Particle dimensions are frequently adjusted according to this idea (e.g. decreasing the particle diameter will raise available sorptive areas and aggregation). However, doing so is not so simple since changes in particle size alter domain-dependency, magnetic susceptibility, paramagnetism, and material cost.

Magnetic separation processes are becoming the most suitable procedures for extraction and purification in complex suspensions. Popular separation applications that employ MP include wastewater treatment, magnetic-particle imaging, and pollutant removal via fractionation methods or microfluidic devices (Watarai *et al*., 2004; Yavuz *et al*., 2009). Although uses in drug delivery and protein isolation exist, the efficacy and purity of cell capture, as well as the reusability of recovered cells, are limited. Primary concerns with therapeutic treatments include reactive constituents (like those that are unfavorably responsive to other cell populations) and unwarranted aggregation (which can have negative symptoms that impact biocompatibility) (Furlani, 2010).

Most magnetic separations can be categorized into two types: high-gradient magnetic separation (HGMS) and low-gradient magnetic separation (LGMS). Traditionally, HGMS involves flowing a suspension through a column (sometimes containing a packed bed) with magnetically-susceptible wires providing strong magnetic gradients generally larger than 1000 T/m. Other convenient magnetic sources have been composed of rare-earth metals or electromagnets. Since the field gradients tend to be high, the separation is quick. Researchers have performed magnetic chromatography experiments to successfully correlate particle size with

HGMS efficiency (Moeser *et al*., 2004). However, it has proven difficult to generate accurate theoretical models for optimization purposes. Indeed, there will always be unanticipated, complicating factors in experimentation (such as polydispersity or changes in viscosity) that affect the agreement between theoretical and experimental studies, especially at such strong magnetic field gradients (Andreu *et al*., 2011). Additionally, HGMS of individual ferrofluid nanoparticles has not been extensively studied. Alternatively, LGMS allows for more dense suspensions and separation is preferably driven by cooperative MP with magnetic gradients in the range of 1-1000 T/m. This makes it strongly dependent on particle properties. Still, the disadvantage is that the process takes relatively longer than HGMS. LGMS research is also not as prominent as that of HGMS.

2.4   **Magnetostatic Maxwell's Equations**

The focus of this study is to further develop existing simulations to ensure that certain constraints (given by Maxwell's Equations of magnetostatics) that act on the system are satisfied. Most readily this means that the divergence of the induction field must equal zero:

$$\nabla \cdot \boldsymbol{B} = 0 \qquad\qquad [2.5]$$

and the curl of the magnetic field must be zero:

$$\nabla \times \boldsymbol{H} = \boldsymbol{0} \qquad\qquad [2.6]$$

Equation [2.5] is known as Gauss's Law and equation [2.6] is recognized as Ampère's Law. Gauss's Law ensures that there are no free magnetic poles while Ampère's Law establishes that the tangential components of the magnetic field are zero, especially when there are no current flows. Upon examination of equation [2.1], it quickly leads to the revelation that the divergence of

the **M**-field and the divergence of the **H**-field must be equal and opposite. Consequently, equation [2.5] becomes:

$$-\nabla \cdot \boldsymbol{H} = \nabla \cdot \boldsymbol{M} \qquad [2.7]$$

When the **H**-field applied is uniform or divergence-free, the equation simplifies further:

$$\nabla \cdot \boldsymbol{M} = 0 \qquad [2.8]$$

Therefore, in the presence of a uniform or divergence-free magnetic field, only the material response **M**-field must be solenoidal.

2.5 **Ferrofluid Simulations**

The conventional approach to ferrofluid modeling corresponds to a dispersion of magnetic particles that is so dilute that the interparticle interactions are weak or the particle contribution to the total field that animates all particles is negligible. However, this assumption is inadequate since many applications, such as drug delivery, require more concentrated ferromagnetic dispersions. It also simplifies detailed descriptions of external conditions by stating that the system was placed at a given location in a field **H**, rather than declaring that the experiment was performed at a particular distance and orientation with respect to a magnet. One of the disadvantages to adopting methods with smoothed particle distributions or volume-averaged concentrations is that they neglect interparticle exchanges and are consequently ineffective in representing dense particulate configurations. This is notably observed when high concentrations of ferroparticles congregate in an area of a volume more than another, like during magnetic separation. Research has yet to provide comprehensive and quantitative tracking of individual particles in dense suspensions for the analysis of behavior in complex geometries and inhomogeneous magnetic fields.

Traditionally, ferrofluids have been treated as continuum systems where the magnetic particles are inseparable from the carrier fluid and an additional body force is appended to the Navier-Stokes equation to account for the relationship between the applied magnetic field and the fluid's magnetization (Kružík and Prohl, 2006; Shliomis, 1974). There is generally no electric field in the fluid but rather a polarization force that affects the bodies of the particles, which requires material magnetization in the presence of magnetic field gradients. Rosensweig (1985) proposed the "quasi-equilibrium" approach, which assumes that the local magnetization is in persistent equilibrium with the local magnetic field via a simply proportional relation. Shliomis (1974) had expressed this relationship in terms of the Langevin function and the saturation magnetization of the magnetic material M_S. However, since magnetization is not directly related to the magnetic field due to properties like magnetic hysteresis, the relationship differs from other models by specific confines and accuracy. And though useful in studying various effects, the approximation did not account for all FHD behavior, such as the magnetoviscous effect. Magnetoviscous effects emerge in the form of an enhanced effective shear viscosity due to excess dissipation when a flowing ferrofluid is subjected to a magnetic field (Odenbach, 2002). Furthermore, the "quasi-equilibrium" approach did not address the orientation of the microstructure induced by the application of external magnetic fields or the details of fluid-particulate-boundary substructure at extremely small length scales. Thus, magnetization, often modeled by a relaxation equation that assumes noninteracting particles in the absence of flow, has been incorrectly assumed.

Ferrofluid studies have adequately recognized the effects of applied magnetic fields on the structure and material properties of the ferrofluid. Yet, many simulations have assumed that there is no complete interplay between the applied magnetic field and the ferrofluid's quasistationary magnetization. Inhomogeneities in particle concentration also have significant impacts on

magnetic force and average particle velocity, strongly suggesting that the diffusive behavior is highly-linked to the Maxwell's equations. For recent ferrofluid simulation techniques, the applied magnetic fields are assumed to be homogeneous and simply proportional to the corresponding local magnetizations (Papadopoulos *et al*., 2012). However, experimentally-founded magnetic fields cannot be described by simple analytical expressions. These concerns are detected in small local deviations between experiments and theory (Sinha *et al*., 2007). As most studies observe a linear magnetic response in ferroparticles, they tend to negate how the magnetization of the particles has an effect on everything else. Additionally, when a linear relationship relates the particle magnetization to the externally-applied magnetic field, the particles are typically paramagnetic rather than superparamagnetic. These simplifications may prove appropriate for MR fluids but are highly inadequate for ferrofluids because – while the induced magnetic dipole in MR fluids is free to orient within the particle and generally stays aligned with the field – the orientation of the magnetic moment in ferrofluid particles is altered by any force or interaction that affects the particles' orientation and hence, its embedded dipole. Several effects are known to influence the local magnetization. Besides the magnetic interactions between the ferroparticles, others include particle tumbling initiated by hydrodynamic effects through the local flow field, orientation changes produced by nonisotropic media (e.g., biological tissue, small channels, ferroparticle crowding, etc.), and Brownian influences that tend to cause particle orientations to evolve and relax towards a uniform distribution. In this study, additional effects on the particles' orientations will be included.

3. METHODOLOGY

3.1 <u>Suspension Rheology</u>

3.1.1 <u>Fluid Dynamics of the Liquid Carrier</u>

Brownian motion is the thermal agitation by the random motion of the liquid carrier's molecules that keeps the particles suspended within the solution and is observed in functional fluids such as ferrofluids. Ordinary molecular dynamics methods are practical for particles that are no larger than the molecules of the surrounding medium. However, ferroparticles (or their potential colloid formations) tend to be much larger and thus, require simulations that have a longer characteristic Brownian motion time than characteristic molecular motion time. Therefore, the liquid carrier is viewed as a continuum. The Brownian dynamics method assumes that the medium suspending the ferrofluid particles is incompressible and Newtonian. For this particular type of medium, the change of an arbitrarily-sized volume of mass in the fluid can be derived from the mass conservation law to express the equation of continuity:

$$\frac{\partial \rho}{\partial t} + \rho \nabla \cdot \boldsymbol{v} = 0 \qquad [3.1]$$

where ρ is density, t is time, and $\boldsymbol{v}$ is velocity. If the fluid is incompressible (constant ρ), then equation [3.1] reduces to:

$$\nabla \cdot \boldsymbol{v} = 0 \qquad [3.2]$$

From Newton's second law, which details the conservation of momentum, an equation is derived that governs the motion of the fluid:

$$\rho \frac{D\boldsymbol{v}}{Dt} = -\nabla p + \eta \nabla^2 \boldsymbol{v} + \rho \boldsymbol{g} \qquad [3.3]$$

Here, $\frac{D}{Dt}$ is the substantial derivative, p is pressure, η is viscosity, and $\boldsymbol{g}$ is the gravitational acceleration. This expression is known as the Navier-Stokes equation. For colloidal dispersions,

the left-hand side of the Navier-Stokes equation, which describes inertia, can typically be ignored. In addition, the gravitational term is considered negligible. As a result, equation [3.3] reduces to the Stokes equation:

$$\nabla p = \eta \nabla^2 \boldsymbol{v} \qquad\qquad [3.4]$$

The Stokes equation, combined with the continuity equation in equation [3.2] and taken under specific conditions, can be used to acquire an expression for the flow field. For example, under steady flow, equation [3.3] becomes:

$$0 = \nabla^2 \boldsymbol{v} \qquad\qquad [3.5]$$

Boundary conditions contingent on geometry are required to determine an expression for $\boldsymbol{v}$. Thus, equation [3.5] will be resolved in a later section when the relevant information is provided.

3.1.2 **Hydrodynamic Interactions**

When observing a system of suspended particles under fluid flow, hydrodynamic interactions must be accounted for in their behavior. This is especially valid for dense particulate models with aggregation behavior. Hydrodynamic interactions occur when a particle moves about and agitates the fluid in the neighborhood of other particles, even when transported by the fluid motion. The resultant field of the moving particle is conveyed through the solvent and affects the hydrodynamic force, torque, and stresslet of the other particles.

For a spherical particle, the force by the particle on the fluid is solely dependent on the translational velocity, the torque depends just on the angular velocity, and the rate-of-strain tensor is reliant only on the stresslet. Furthermore, the fluid velocity is considerably higher than the relative velocity between a particle and the fluid (i.e. Reynolds number Re satisfies Re $\ll$ 1). Thus, Stokes equation allows for linear analytical solutions of the flow field. As a result, the relationship

between a particle's velocity $\boldsymbol{v}$ and angular velocity $\boldsymbol{\omega}$, the stresslet $\boldsymbol{S}$, the force $\boldsymbol{F}$ and torque $\boldsymbol{T}$ applied to the fluid by a particle, and the rate-of-strain $\mathbf{E}$ is established as:

$$\begin{bmatrix} \boldsymbol{v} - \boldsymbol{U} \\ \boldsymbol{\omega} - \boldsymbol{\Omega} \\ \boldsymbol{S}/\eta \end{bmatrix} = \mathbf{M} \begin{bmatrix} \boldsymbol{F}/\eta \\ \boldsymbol{T}/\eta \\ \mathbf{E} \end{bmatrix} = \begin{bmatrix} \mathrm{a} & \tilde{\mathrm{b}} & \tilde{\mathrm{g}} \\ \mathrm{b} & \mathrm{c} & \tilde{\mathrm{h}} \\ \mathrm{g} & \mathrm{h} & \mathrm{k} \end{bmatrix} \begin{bmatrix} \boldsymbol{F}/\eta \\ \boldsymbol{T}/\eta \\ \mathbf{E} \end{bmatrix} \qquad [3.6]$$

where $\boldsymbol{U}$ and $\boldsymbol{\Omega}$ are the solvent's velocity and angular velocity vectors for an applied flow field in the absence of particles, respectively. The mobility matrix $\mathbf{M}$ consists of the second-rank tensors $\mathbf{a}$, $\mathbf{b}$, and $\mathbf{c}$, third-rank tensors $\mathbf{g}$ and $\mathbf{h}$, and fourth-rank tensor $\mathbf{k}$. Equation [3.6] is conveyed in mobility formulation, expressing the velocity, angular velocity, and stresslet of the particle with dependence on the force, torque, and rate-of-strain tensor, respectively. The other tensors are defined as:

$$\tilde{\mathbf{b}} = \mathbf{b}^t$$

$$\tilde{\mathrm{g}}_{ijk} = \mathrm{g}_{jki}$$

$$\tilde{\mathrm{h}}_{ijk} = \mathrm{h}_{jki}$$

where a superscript 't' symbolizes a matrix transpose operation. For the fourth-rank tensor $\mathbf{k}$:

$$\mathrm{k}_{ijkl} = \mathrm{k}_{klij}$$

Furthermore, it should be noted that the $\mathbf{a}$ and $\mathbf{c}$ tensors are symmetric. To evaluate the mobility tensors, Kim and Karilla (1991) devised a numerical method to calculate them as a function of scalar mobility functions. As an example, the $\mathbf{a}_{12}$ mobility tensor between particle $\alpha = 1$ and $\beta = 2$ is expressed as:

$$\mathbf{a}_{12} = x_{12}^{\mathrm{a}} d_1 d_2 + y_{12}^{\mathrm{a}} (\mathbf{I} - d_1 d_2) \qquad [3.7]$$

in which $\boldsymbol{d}$ is the unit directional vector between particles 1 and 2. The x_{12}^{a} and y_{12}^{a} values are the scalar mobility functions and depend on the distance between particles. They are typically

tabulated. For spheres of identical radii, the general form of the mobility functions and corresponding values are provided in Appendix A.

Expanding equation [3.6] to a two-particle system where the particles are nearly-touching yields:

$$
\begin{bmatrix}
v_1 - U(r_1) \\
v_2 - U(r_2) \\
\omega_1 - \Omega \\
\omega_2 - \Omega \\
S_1/\eta \\
S_2/\eta
\end{bmatrix}
=
\begin{bmatrix}
a_{11} & a_{12} & \tilde{b}_{11} & \tilde{b}_{12} & \tilde{g}_1 \\
a_{21} & a_{22} & \tilde{b}_{21} & \tilde{b}_{22} & \tilde{g}_2 \\
b_{11} & b_{12} & c_{11} & c_{12} & \tilde{h}_1 \\
b_{21} & b_{22} & c_{21} & c_{22} & \tilde{h}_2 \\
g_{11} & g_{12} & h_{11} & h_{12} & k_1 \\
g_{21} & g_{22} & h_{21} & h_{22} & k_2
\end{bmatrix}
\begin{bmatrix}
F_1/\eta \\
F_2/\eta \\
T_1/\eta \\
T_2/\eta \\
E
\end{bmatrix}
\qquad [3.8]
$$

Consequently, the expression can be extended further to a system involving three or more particles and is demonstrated in the next section.

3.1.3 **Additivity of Velocities**

Two approximation methods have been developed that simulate multibody hydrodynamic interactions in a dense colloidal dispersion. Both methods are capable of evaluating essential attributes of a ferrofluid, to a reasonable extent. The first, called the approximation of the additivity of forces, is more effective with smaller systems that consist of a modest amount of particles (~50 or less). It is also best applied to accurately model the lubrication effect, which results when particles are in extremely close proximity. This generates a substantial hydrodynamic interaction between the particles. However, with the second approximation known as the additivity of forces, complications arise when calculating the inverse of the resistance matrix. The present study relies, instead, on the approximation of the additivity of velocities (Satoh *et al*., 1998). With this approach, no inverse matrix calculation is necessary and larger systems can be simulated as a more ideal representation of a dense colloidal dispersion. And since the main focus of the current model

is the aggregation behavior in a flow field, the lubrication effect is deemed irrelevant. Therefore, to consider multibody hydrodynamic interactions, the approximation of the additivity of velocities is employed.

From equation [3.8], one can observe the velocity of a particle α as:

$$\boldsymbol{v}_\alpha - \boldsymbol{U}(\boldsymbol{r}_\alpha) = \frac{1}{\eta}\left(\mathsf{a}_{\alpha\alpha} \cdot \boldsymbol{F}_\alpha + \mathsf{a}_{\alpha\beta} \cdot \boldsymbol{F}_\beta + \tilde{\mathsf{b}}_{\alpha\alpha} \cdot \boldsymbol{T}_\alpha + \tilde{\mathsf{b}}_{\alpha\beta} \cdot \boldsymbol{T}_\beta\right) + \tilde{\mathsf{g}}_\alpha{:}\mathsf{E} \qquad [3.9]$$

It is clear that the contributions in the absence of particle β can be separated from the sum of the ones due to particle β:

$$\boldsymbol{v}_\alpha = \boldsymbol{v}_\alpha^\infty + \sum_{\beta=1(\neq\alpha)}^{N} \Delta\boldsymbol{v}_{\alpha\beta} \qquad [3.10]$$

in which N is the total number of ferrofluid particles and:

$$\boldsymbol{v}_\alpha^\infty = \boldsymbol{U}(\boldsymbol{r}_\alpha) + \frac{1}{\eta}\left(\mathsf{a}_{\alpha\alpha}^\infty \cdot \boldsymbol{F}_\alpha + \tilde{\mathsf{b}}_{\alpha\alpha}^\infty \cdot \boldsymbol{T}_\alpha\right) + \tilde{\mathsf{g}}_\alpha^\infty{:}\mathsf{E}$$

$$\Delta\boldsymbol{v}_{\alpha\beta} = \frac{1}{\eta}\left[(\mathsf{a}_{\alpha\alpha} - \mathsf{a}_{\alpha\alpha}^\infty) \cdot \boldsymbol{F}_\alpha + \mathsf{a}_{\alpha\beta} \cdot \boldsymbol{F}_\beta + \left(\tilde{\mathsf{b}}_{\alpha\alpha} - \tilde{\mathsf{b}}_{\alpha\alpha}^\infty\right) \cdot \boldsymbol{T}_\alpha + \tilde{\mathsf{b}}_{\alpha\beta} \cdot \boldsymbol{T}_\beta\right] + (\tilde{\mathsf{g}}_\alpha - \tilde{\mathsf{g}}_\alpha^\infty){:}\mathsf{E}$$

The effects supplied from all other particles are added up first. These multibody interactions are estimated as the sum of contributions between particle pairs. Then, the "friction" term of particle α is only considered once and is not included with the other particles. The mobility tensors with superscript '∞' are those in which the particles of interest are separated by an infinite distance. Triple-body interactions are neglected in this approximation method, as is explained further when discussing steric overlap in section 3.1.7. As a result of the preceding operations, a simplistic matrix form is developed:

$$\begin{bmatrix} \boldsymbol{v}_1 - \boldsymbol{U}(\boldsymbol{r}_1) \\ \boldsymbol{v}_2 - \boldsymbol{U}(\boldsymbol{r}_2) \\ \vdots \\ \boldsymbol{v}_N - \boldsymbol{U}(\boldsymbol{r}_N) \\ \boldsymbol{\omega}_1 - \boldsymbol{\Omega} \\ \boldsymbol{\omega}_2 - \boldsymbol{\Omega} \\ \vdots \\ \boldsymbol{\omega}_N - \boldsymbol{\Omega} \end{bmatrix} = \frac{1}{\eta} \begin{bmatrix} \mathbf{a}'_{11} & \mathbf{a}_{12} & \cdots & \mathbf{a}_{1N} & \tilde{\mathbf{b}}'_{11} & \tilde{\mathbf{b}}_{12} & \cdots & \tilde{\mathbf{b}}_{1N} \\ \mathbf{a}_{21} & \mathbf{a}'_{22} & \cdots & \mathbf{a}_{2N} & \tilde{\mathbf{b}}_{21} & \tilde{\mathbf{b}}'_{22} & \cdots & \tilde{\mathbf{b}}_{2N} \\ \vdots & \vdots & & \vdots & \vdots & \vdots & & \vdots \\ \mathbf{a}_{N1} & \mathbf{a}_{N2} & \cdots & \mathbf{a}'_{NN} & \tilde{\mathbf{b}}_{N1} & \tilde{\mathbf{b}}_{N2} & \cdots & \tilde{\mathbf{b}}'_{NN} \\ \mathbf{b}'_{11} & \mathbf{b}_{12} & \cdots & \mathbf{b}_{1N} & \mathbf{c}'_{11} & \mathbf{c}_{12} & \cdots & \mathbf{c}_{1N} \\ \mathbf{b}_{21} & \mathbf{b}'_{22} & \cdots & \mathbf{b}_{2N} & \mathbf{c}_{21} & \mathbf{c}'_{22} & \cdots & \mathbf{c}_{2N} \\ \vdots & \vdots & & \vdots & \vdots & \vdots & & \vdots \\ \mathbf{b}_{N1} & \mathbf{b}_{N2} & \cdots & \mathbf{b}'_{NN} & \mathbf{c}_{N1} & \mathbf{c}_{N2} & \cdots & \mathbf{c}'_{NN} \end{bmatrix} \begin{bmatrix} \boldsymbol{F}_1 \\ \boldsymbol{F}_2 \\ \vdots \\ \boldsymbol{F}_N \\ \boldsymbol{T}_1 \\ \boldsymbol{T}_2 \\ \vdots \\ \boldsymbol{T}_N \end{bmatrix} + \begin{bmatrix} \tilde{\boldsymbol{g}}'_1 \\ \tilde{\boldsymbol{g}}'_2 \\ \vdots \\ \tilde{\boldsymbol{g}}'_N \\ \tilde{\mathbf{h}}'_1 \\ \tilde{\mathbf{h}}'_2 \\ \vdots \\ \tilde{\mathbf{h}}'_N \end{bmatrix} : \boldsymbol{E} \quad [3.11]$$

The mobility matrix in the first term of the right-hand side with the tensors $\mathbf{a}'_{11}$ to $\mathbf{c}'_{NN}$ is a truncated mobility matrix $\widehat{\mathbf{M}}$. The mobility tensors of $\mathbf{a}'_{\alpha\alpha}$ and $\tilde{\boldsymbol{g}}'_\alpha$ are interpreted as:

$$\mathbf{a}'_{\alpha\alpha} = \mathbf{a}^\infty_{\alpha\alpha} + \sum_{\beta=1(\neq\alpha)}^{N} (\mathbf{a}_{\alpha\alpha} - \mathbf{a}^\infty_{\alpha\alpha}) \qquad (\alpha = 1,2,\cdots,N) \qquad [3.12]$$

$$\tilde{\boldsymbol{g}}'_\alpha = \tilde{\boldsymbol{g}}^\infty_\alpha + \sum_{\beta=1(\neq\alpha)}^{N} (\tilde{\boldsymbol{g}}_\alpha - \tilde{\boldsymbol{g}}^\infty_\alpha) \qquad (\alpha = 1,2,\cdots,N) \qquad [3.13]$$

where parallel forms of equation [3.12] are observed for the $\tilde{\mathbf{b}}'_{\alpha\alpha}$, $\mathbf{b}'_{\alpha\alpha}$, and $\mathbf{c}'_{\alpha\alpha}$ tensors while the $\tilde{\mathbf{h}}'_\alpha$ tensor assumes a similar structure to equation [3.13]. It should be noted that $\mathbf{a}_{\alpha\alpha}$, $\tilde{\mathbf{b}}_{\alpha\alpha}$, and $\tilde{\boldsymbol{g}}_\alpha$ rely on the position of particle β. Furthermore, when the particles are rigid spheres with radius a, the mobility tensors with superscript '∞' are taken as:

$$\mathbf{a}^\infty_{\alpha\alpha} = \frac{1}{6\pi a}\mathbf{I}, \quad \tilde{\mathbf{b}}^\infty_{\alpha\alpha} = \frac{1}{4\pi a^2}\mathbf{I}, \quad \mathbf{b}^\infty_{\alpha\alpha} = \frac{1}{4\pi a^2}\mathbf{I}, \quad \mathbf{c}^\infty_{\alpha\alpha} = \frac{1}{8\pi a^3}\mathbf{I}, \quad \tilde{\boldsymbol{g}}^\infty_\alpha = 0, \quad \tilde{\mathbf{h}}^\infty_\alpha = 0$$

In the case when the forces and torques are solely dependent on the displacement and rotation respectively, the $\tilde{\mathbf{b}}^\infty_{\alpha\alpha}$ and $\mathbf{b}^\infty_{\alpha\alpha}$ tensors are set to zero.

The mobility matrix $\widehat{\mathbf{M}}$ in equation [3.11] contains information about the diffusivities. The $\mathbf{a}$ and $\mathbf{c}$ tensors are associated with the translational and rotational diffusivities, respectively, while the $\mathbf{b}$ and $\tilde{\mathbf{b}}$ tensors handle the combination of the translational and rotational diffusion. Thus, the

mobility matrix relates to the diffusion matrix $\boldsymbol{D}$ by:

$$\widehat{\mathbf{M}} = \frac{\eta}{kT}\boldsymbol{D} = \frac{\eta}{kT}\begin{pmatrix} \boldsymbol{D}^{\mathrm{T}} & \widetilde{\boldsymbol{D}}^{\mathrm{C}} \\ \boldsymbol{D}^{\mathrm{C}} & \boldsymbol{D}^{\mathrm{R}} \end{pmatrix} \qquad [3.14]$$

and accordingly:

$$\mathsf{a} = \frac{\eta}{kT}\boldsymbol{D}^{\mathrm{T}}, \quad \mathsf{c} = \frac{\eta}{kT}\boldsymbol{D}^{\mathrm{R}}, \quad \mathsf{b} = \frac{\eta}{kT}\boldsymbol{D}^{\mathrm{C}}, \quad \widetilde{\mathsf{b}} = \frac{\eta}{kT}\widetilde{\boldsymbol{D}}^{\mathrm{C}} \qquad [3.15]$$

where $\boldsymbol{D}^{\mathrm{T}}$ is the translational diffusivity tensor, $\boldsymbol{D}^{\mathrm{R}}$ is the rotational diffusivity tensor, $\boldsymbol{D}^{\mathrm{C}}$ is the coupled diffusivity tensor, k is Boltzmann's constant, and T is the absolute temperature of the fluid. Tensors $\boldsymbol{D}^{\mathrm{C}}$ and $\widetilde{\boldsymbol{D}}^{\mathrm{C}}$ are related by:

$$\widetilde{\boldsymbol{D}}^{\mathrm{C}} = (\boldsymbol{D}^{\mathrm{C}})^{t}$$

In the absence of hydrodynamic interactions between particles, the diffusivity tensors would simply become:

$$\boldsymbol{D} = D_0 \delta_{ij}\mathbf{I}$$

where D_0 is the diffusion coefficient at infinite dilution, $\mathbf{I}$ is the unit matrix, and δ_{ij} is the Kronecker delta which is defined by:

$$\delta_{ij} = \begin{cases} 0 & \text{if } i \neq j \\ 1 & \text{if } i = j \end{cases}$$

3.1.4 **Energies, Forces, and Torques of Interacting Magnetic Particles**

In colloidal suspensions, several forces regulate the dynamics that describe particle behavior, especially those not resulting from the surrounding solvent. When considering nonhydrodynamic interactions, a ferromagnetic particle induces two energies due to its permanent dipole: particle-particle magnetic interaction energy and particle-field interaction energy. The former is due to the attractive and repulsive nature between particles while the latter develops from a particle's response to an external magnetic field. A third, known as the steric interaction energy,

arises from the presence of the particle's surfactant monolayer. The energy equations for particle-particle, particle-field, and steric interactions are given, respectively, as:

$$E_{\alpha\beta}^{m} = \frac{\mu_0}{4\pi} \left[\frac{m_\alpha \cdot m_\beta}{r_{\alpha\beta}^3} - \frac{3}{r_{\alpha\beta}^5} (m_\alpha \cdot r_{\alpha\beta})(m_\beta \cdot r_{\alpha\beta}) \right] \qquad [3.16]$$

$$E_\alpha^{h} = -\mu_0 (m_\alpha \cdot H) \qquad [3.17]$$

$$E_{\alpha\beta}^{v} = \frac{1}{2}\pi d_s^2 n_s kT \left[2 - \frac{s_\delta + 2}{d_\delta} \ln\left(\frac{1 + d_\delta}{1 + s_\delta/2}\right) - \frac{s_\delta}{d_\delta} \right] \qquad [3.18]$$

where m_α is the magnetic dipole moment of particle α, $r_{\alpha\beta}$ is the direction vector from particle α to particle β, $r_{\alpha\beta} = |r_{\alpha\beta}|$, d_s is the particle diameter excluding the steric layer, n_s is the quantity of surfactant elements per unit area on the particle's surface, and μ_0 is the permeability of free space. In equation [3.18], $d_\delta = 2\delta/d_s$, which represents the ratio of the surfactant monolayer thickness to the radius of the solid part of the particle, δ is the thickness of the steric layer, and s_δ is the ratio of the surface-to-surface separation (excluding surfactant layers) between two particles to the diameter of the solid part of a particle, equal to $2(r_{\alpha\beta}/d_s - 1)$. From the gradient of the energies, the corresponding forces and torques are derived as:

$$F_{\alpha\beta}^{m} = -\frac{3\mu_0 m^2}{4\pi r_{\alpha\beta}^4} \left\{ \begin{array}{c} -(n_\alpha \cdot n_\beta)d_{\alpha\beta} + 5(n_\alpha \cdot d_{\alpha\beta})(n_\beta \cdot d_{\alpha\beta})d_{\alpha\beta} \\ -[(n_\beta \cdot d_{\alpha\beta})n_\alpha + (n_\alpha \cdot d_{\alpha\beta})n_\beta] \end{array} \right\} \qquad [3.19]$$

$$T_{\alpha\beta}^{m} = -\frac{\mu_0 m^2}{4\pi r_{\alpha\beta}^3} \left[n_\alpha \times n_\beta - 3(n_\beta \cdot d_{\alpha\beta})n_\alpha \times d_{\alpha\beta} \right] \qquad [3.20]$$

$$F_\alpha^{h} = \mu_0 m H \nabla(n_\alpha \cdot h) \qquad [3.21]$$

$$T_\alpha^{h} = \mu_0 m H n_\alpha \times h \qquad [3.22]$$

$$F_{\alpha\beta}^{v} = \frac{1}{2}\pi d_s^2 n_s kT \frac{1}{\delta} d_{\alpha\beta} \ln\left(\frac{d}{r_{\alpha\beta}}\right) \qquad (d_s \leq r_{\alpha\beta} \leq d) \qquad [3.23]$$

in which $\boldsymbol{d}_{\alpha\beta}$ denotes the unit direction vector of the interparticle vector $\boldsymbol{r}_{\alpha\beta}$, $\boldsymbol{n}_\alpha$ represents the unit direction vector of the magnetic dipole moment $\boldsymbol{m}_\alpha$, $m = |\boldsymbol{m}_\alpha|$, the unit vector $\boldsymbol{h}$ signifies that of the magnetic field vector $\boldsymbol{H}$, $H = |\boldsymbol{H}|$, and $d(= 2a)$ is the diameter that includes the steric layer thickness. In the above-mentioned equations, $\boldsymbol{F}^{\mathrm{m}}$ and $\boldsymbol{T}^{\mathrm{m}}$ result from magnetic interactions of adjacent particle β on particle α, $\boldsymbol{F}^{\mathrm{h}}$ and $\boldsymbol{T}^{\mathrm{h}}$ are due to the sway of an applied magnetic field on particle α, and $\boldsymbol{F}^{\mathrm{v}}$ represents the steric repulsion force of particle β on particle α.

3.1.5 **The Langevin Equation**

For simulations of two or more particles spanning large time sets and subject to Brownian motion, particle-particle forces, and macroscopic flow activity, numerical integration is typically employed. To describe the Brownian motion of a colloidal system of N particles with multibody hydrodynamic interactions between them, a generalized Langevin equation is considered:

$$m_w \frac{d\boldsymbol{v}_\alpha}{dt} = \boldsymbol{F}_\alpha^{\mathrm{P}} + \boldsymbol{F}_\alpha^{\mathrm{f}} + \boldsymbol{F}_\alpha^{\mathrm{b}} \qquad [3.24]$$

where m_w is the particle's mass, $\boldsymbol{F}_\alpha^{\mathrm{P}}$ is the force of nonhydrodynamic interactions such as those of the other particles on the one of interest, $\boldsymbol{F}_\alpha^{\mathrm{f}}$ is the force of the fluid on particle α, and $\boldsymbol{F}_\alpha^{\mathrm{b}}$ is the force of the Brownian motion of particle α. The above Langevin equation describes the translational momentum balance of a dense particle dispersion that undergoes interparticle hydrodynamic interactions. The force $\boldsymbol{F}_\alpha^{\mathrm{P}}$ and torque $\boldsymbol{T}_\alpha^{\mathrm{P}}$ acting on particle α are:

$$\boldsymbol{F}_\alpha^{\mathrm{P}} = \sum_{\beta=1(\neq\alpha)}^{N} \left(\boldsymbol{F}_{\alpha\beta}^{\mathrm{m}} + \boldsymbol{F}_{\alpha\beta}^{\mathrm{v}} \right) + \boldsymbol{F}_\alpha^{\mathrm{h}}$$

$$[3.25]$$

$$\boldsymbol{T}_\alpha^{\mathrm{P}} = \sum_{\beta=1(\neq\alpha)}^{N} \boldsymbol{T}_{\alpha\beta}^{\mathrm{m}} + \boldsymbol{T}_\alpha^{\mathrm{h}}$$

where the forces and torques defined in equations [3.19] to [3.23] are administered. For $\boldsymbol{F}_\alpha^{\text{f}}$, equation [3.11] yields:

$$\boldsymbol{F}_\alpha^{\text{f}} = -\eta \sum_{\beta=1}^{N} \widehat{\mathbf{M}}_{\alpha\beta}^{-1} \cdot \left\{ \left[\boldsymbol{v}_\beta - \boldsymbol{U}(\boldsymbol{r}_\beta) \right] - \tilde{\mathbf{g}}'_\beta : \mathbf{E} \right\} \qquad [3.26]$$

As for the Brownian motion force, it is characterized with:

$$\langle \boldsymbol{F}_\alpha^{\text{b}}(t) \rangle = 0 , \qquad \langle \boldsymbol{F}_\alpha^{\text{b}}(t) \boldsymbol{F}_\beta^{\text{b}}(t') \rangle = 2\eta kT \widehat{\mathbf{M}}_{\alpha\beta}^{-1} \delta(t - t') \qquad [3.27]$$

A similar procedure for the torques is employed when regarding the equation of rotational motion.

Since both the translational and rotational momentums are considered in the Brownian dynamics model, the equation of motion can be represented in a generalized matrix form:

$$\begin{bmatrix} m_w \, d\boldsymbol{v}/dt \\ I \, d\boldsymbol{\omega}/dt \end{bmatrix} = \begin{bmatrix} \boldsymbol{F}^{\text{P}} \\ \boldsymbol{T}^{\text{P}} \end{bmatrix} - kT \begin{bmatrix} \boldsymbol{D}^{\text{T}} & \widetilde{\boldsymbol{D}}^{\text{C}} \\ \boldsymbol{D}^{\text{C}} & \boldsymbol{D}^{\text{R}} \end{bmatrix}^{-1} \left\{ \begin{bmatrix} \boldsymbol{v} - \boldsymbol{U}(\boldsymbol{r}) \\ \boldsymbol{\omega} - \boldsymbol{\Omega} \end{bmatrix} - \begin{bmatrix} \tilde{\mathbf{g}}' \\ \tilde{\mathbf{h}}' \end{bmatrix} : \mathbf{E} \right\} + \begin{bmatrix} \boldsymbol{F}^{\text{b}} \\ \boldsymbol{T}^{\text{b}} \end{bmatrix} \qquad [3.28]$$

Here, the relationship in [3.14] is used to convert the mobility matrix and pose the expression in terms of the diffusivity tensors. Then, by multiplying both sides with $\boldsymbol{D}/kT$, summing the equation with respect to β, and applying a mathematical manipulation algorithm proposed by Ermak and McCammon (1978), equations for the change in translational and rotational displacement can be obtained. First, the translational velocity of Brownian ferroparticle α at time t is derived:

$$\begin{aligned} \boldsymbol{v}_\alpha(t) = \boldsymbol{U}(\boldsymbol{r}_\alpha) &+ \frac{1}{kT} \sum_{\beta=1}^{N} \boldsymbol{D}_{\alpha\beta}^{\text{T}}(t) \cdot \boldsymbol{F}_\beta^{\text{P}}(t) + \frac{1}{kT} \sum_{\beta=1}^{N} \widetilde{\boldsymbol{D}}_{\alpha\beta}^{\text{C}}(t) \cdot \boldsymbol{T}_\beta^{\text{P}}(t) \\ &+ \sum_{\beta=1(\neq\alpha)}^{N} \tilde{\mathbf{g}}_\alpha(t) : \boldsymbol{\Delta}^\infty + \sum_{\beta=1}^{N} \frac{\partial}{\partial \boldsymbol{r}_\beta} \cdot \boldsymbol{D}_{\alpha\beta}^{\text{T}}(t) + \Delta \boldsymbol{v}_\alpha^{\text{B}}(t) \end{aligned} \qquad [3.29]$$

where $\boldsymbol{\Delta}^\infty$ is the symmetric part of the rate-of-strain tensor. If the forward finite difference approximation to $\boldsymbol{v}_\alpha = d\boldsymbol{r}_\alpha/dt$ is utilized, then the change in the translational displacement of particle α can be expressed as:

$$r_\alpha(t + \Delta t) = r_\alpha(t)$$

$$+ \left\{ U(r_\alpha) + \frac{1}{kT} \sum_{\beta=1}^{N} D_{\alpha\beta}^{\mathrm{T}}(t) \cdot F_\beta^{\mathrm{P}}(t) \right.$$

$$+ \frac{1}{kT} \sum_{\beta=1}^{N} \widetilde{D}_{\alpha\beta}^{\mathrm{C}}(t) \cdot T_\beta^{\mathrm{P}}(t) + \sum_{\beta=1(\neq\alpha)}^{N} \widetilde{g}_\alpha(t) : \Delta^\infty \qquad [3.30]$$

$$\left. + \sum_{\beta=1}^{N} \frac{\partial}{\partial r_\beta} \cdot D_{\alpha\beta}^{\mathrm{T}}(t) \right\} \Delta t + \Delta r_\alpha^{\mathrm{B}}(t)$$

in which the $[(\nabla \cdot D^{\mathrm{T}})\Delta t]$-term adjusts for the spatial dependency of the diffusivity by establishing a drift velocity that moves the particles in the direction of the region of higher mobility. The Brownian motion term $\Delta r_\alpha^{\mathrm{B}}$ is characterized by zero mean:

$$\langle \Delta r_\alpha^{\mathrm{B}} \rangle = 0 \qquad [3.31]$$

and variance:

$$\langle (\Delta r_\alpha^{\mathrm{B}})(\Delta r_\beta^{\mathrm{B}}) \rangle = 2 D_{\alpha\beta}^{\mathrm{T}} \Delta t \qquad [3.32]$$

When considering the diffusivity of a single particle, the self-diffusion tensors appear as:

$$D_{\alpha\alpha}^{\mathrm{T}} = \frac{kT}{6\pi\eta a} I, \quad D_{\alpha\alpha}^{\mathrm{R}} = \frac{kT}{8\pi\eta a^3} I, \quad D_{\alpha\alpha}^{\mathrm{C}} = \frac{kT}{4\pi\eta a^2} I \qquad [3.33]$$

By substituting $D_{\alpha\alpha}^{\mathrm{T}}$ into equation [3.32] and solving $\Delta r_\alpha^{\mathrm{B}}$ using a random number vector r_n that is characterized by zero mean and variance equal to $\frac{1}{4}$, an expression for the Brownian displacement term can be derived:

$$\Delta r_\alpha^{\mathrm{B}} = \sqrt{\frac{4kT\Delta t}{3\pi\eta a}} \, r_n \qquad [3.34]$$

Concerning the rotation, the angular velocity of particle α at time t is derived:

$$\boldsymbol{\omega}_\alpha(t) = \boldsymbol{\Omega} + \frac{1}{kT}\sum_{\beta=1}^{N} \boldsymbol{D}_{\alpha\beta}^{\mathrm{C}}(t) \cdot \boldsymbol{F}_\beta^{\mathrm{P}}(t) + \frac{1}{kT}\sum_{\beta=1}^{N} \boldsymbol{D}_{\alpha\beta}^{\mathrm{R}}(t) \cdot \boldsymbol{T}_\beta^{\mathrm{P}}(t)$$
$$+ \sum_{\beta=1(\neq\alpha)}^{N} \tilde{\mathrm{h}}_\alpha(t) : \boldsymbol{\Delta}^\infty + \sum_{\beta=1}^{N} \frac{\partial}{\partial \boldsymbol{r}_\beta} \cdot \boldsymbol{D}_{\alpha\beta}^{\mathrm{C}}(t) + \Delta\boldsymbol{\omega}_\alpha^{\mathrm{B}}(t)$$

[3.35]

Similar to the operation for translational velocity, if the forward finite difference approximation to $\boldsymbol{\omega}_\alpha = d\boldsymbol{\varphi}_\alpha/dt$ is used, then the change in the orientation angle of particle α can be expressed as:

$$\boldsymbol{\varphi}_\alpha(t + \Delta t) = \boldsymbol{\varphi}_\alpha(t)$$
$$+ \left\{ \boldsymbol{\Omega} + \frac{1}{kT}\sum_{\beta=1}^{N} \boldsymbol{D}_{\alpha\beta}^{\mathrm{C}}(t) \cdot \boldsymbol{F}_\beta^{\mathrm{P}}(t) + \frac{1}{kT}\sum_{\beta=1}^{N} \boldsymbol{D}_{\alpha\beta}^{\mathrm{R}}(t) \cdot \boldsymbol{T}_\beta^{\mathrm{P}}(t) \right.$$
$$\left. + \sum_{\beta=1(\neq\alpha)}^{N} \tilde{\mathrm{h}}_\alpha(t) : \boldsymbol{\Delta}^\infty + \sum_{\beta=1}^{N} \frac{\partial}{\partial \boldsymbol{r}_\beta} \cdot \boldsymbol{D}_{\alpha\beta}^{\mathrm{C}}(t) \right\} \Delta t + \Delta\boldsymbol{\varphi}_\alpha^{\mathrm{B}}(t)$$

[3.36]

This equation can be converted to an expression that describes the change in the dipole orientation $\boldsymbol{n}_\alpha$ by multiplying both sides by $[\times \boldsymbol{n}_\alpha]$. The Brownian motion term $\Delta\boldsymbol{\varphi}_\alpha^{\mathrm{B}}$ is characterized by zero mean:

$$\langle \Delta\boldsymbol{\varphi}_\alpha^{\mathrm{B}} \rangle = 0$$

[3.37]

and variance:

$$\langle (\Delta\boldsymbol{\varphi}_\alpha^{\mathrm{B}})(\Delta\boldsymbol{\varphi}_\beta^{\mathrm{B}}) \rangle = 2\boldsymbol{D}_{\alpha\beta}^{\mathrm{R}}\Delta t$$

[3.38]

By substituting $\boldsymbol{D}_{\alpha\alpha}^{\mathrm{R}}$ from equation [3.33] into equation [3.38] and solving $\Delta\boldsymbol{\varphi}_\alpha^{\mathrm{B}}$ by exploiting a similar procedure used to solve equation [3.34], an expression for the Brownian rotation term is:

$$\Delta\boldsymbol{\varphi}_\alpha^{\mathrm{B}} = \sqrt{\frac{kT\Delta t}{\pi\eta a^3}}\, \boldsymbol{r}_n$$

[3.39]

Additionally, the Brownian displacement and rotation are ultimately linked via:

$$\langle (\Delta\boldsymbol{r}_\alpha^{\mathrm{B}})(\Delta\boldsymbol{\varphi}_\beta^{\mathrm{B}}) \rangle = 2\tilde{\boldsymbol{D}}_{\alpha\beta}^{\mathrm{C}}\Delta t$$

[3.40]

Under a simple shear flow:

$$U(r) = \Omega \times r + \Delta^\infty \cdot r \qquad [3.41]$$

in which a linear flow field exhibits:

$$\Omega = \frac{1}{2} \nabla \times v = -\frac{\dot{\gamma}}{2} \begin{bmatrix} 0 \\ 0 \\ 1 \end{bmatrix} \qquad [3.42]$$

and the symmetric part of the rate-of-strain tensor is:

$$\Delta^\infty = \frac{1}{2} (\nabla v \times \nabla v^t) = \frac{\dot{\gamma}}{2} \begin{bmatrix} 0 & 1 & 0 \\ 1 & 0 & 0 \\ 0 & 0 & 0 \end{bmatrix} \qquad [3.43]$$

where $\dot{\gamma}$ is the shear rate.

3.1.6 **Quaternions**

To bypass the inefficient use of Euler angles and the intrinsic singularity at $\theta = 0$, Evans and Murad (1977) developed a method by means of a set of four parameters used in the equations of motion called quaternions:

$$\begin{aligned}
\chi &= \cos\left(\frac{\theta}{2}\right) \cdot \cos\left(\frac{\psi + \phi}{2}\right) \\
\mu &= \sin\left(\frac{\theta}{2}\right) \cdot \cos\left(\frac{\psi - \phi}{2}\right) \\
\kappa &= \sin\left(\frac{\theta}{2}\right) \cdot \sin\left(\frac{\psi - \phi}{2}\right) \\
\zeta &= \cos\left(\frac{\theta}{2}\right) \cdot \sin\left(\frac{\psi + \phi}{2}\right)
\end{aligned} \qquad [3.44]$$

where θ, ψ, and ϕ are Goldstein Euler angles (Goldstein, 1971). One can see from this equation that the quaternions are not independent and rely on the relationship:

$$\chi^2 + \mu^2 + \kappa^2 + \zeta^2 = 1 \qquad [3.45]$$

Evans and Murad (1977) specifically built up this method in carrying out molecular dynamics calculations for solving rigid body equations and will be utilized in the ferrofluid model. In order

to free the equations of motion from singularities, the quaternions present an orthogonal and Euclidean representation of orientation space. This results in a reduction of computation time when compared to a conventional Euler angle procedure. The principal velocity vector $\boldsymbol{V}_{\text{principal}}$ is related to the lab velocity vector $\boldsymbol{V}_{\text{lab}}$ through:

$$\boldsymbol{V}_{\text{principal}} = \boldsymbol{A} \cdot \boldsymbol{V}_{\text{lab}} \qquad \text{[3.46]}$$

where the rotation matrix $\boldsymbol{A}$ is given by:

$$\boldsymbol{A} = \begin{bmatrix} \mu^2 - \kappa^2 + \chi^2 - \zeta^2 & 2(\zeta\chi - \kappa\mu) & 2(\mu\zeta + \kappa\chi) \\ -2(\kappa\mu + \zeta\chi) & \kappa^2 - \mu^2 + \chi^2 - \zeta^2 & 2(\mu\chi - \kappa\zeta) \\ 2(\mu\zeta - \kappa\chi) & -2(\kappa\zeta + \mu\chi) & \zeta^2 - \kappa^2 + \chi^2 - \mu^2 \end{bmatrix} \qquad \text{[3.47]}$$

The quaternion time derivatives can be calculated by employing an equation that connects the principal angular velocity $\boldsymbol{\omega}_p$ and quaternions:

$$\begin{bmatrix} \dot{\kappa} \\ \dot{\mu} \\ \dot{\zeta} \\ \dot{\chi} \end{bmatrix} = \frac{1}{2} \begin{bmatrix} -\zeta & -\chi & \mu & \kappa \\ \chi & -\zeta & -\kappa & \mu \\ \kappa & \mu & \chi & \zeta \\ -\mu & \kappa & -\zeta & \chi \end{bmatrix} \begin{bmatrix} \omega_{px} \\ \omega_{py} \\ \omega_{pz} \\ 0 \end{bmatrix} \qquad \text{[3.48]}$$

where the dot above a quaternion indicates a time-rate and will be designated as the "quaternion velocities." The large matrix on the right-hand side is orthogonal and determining the inverse is simple. The quaternion velocities and time-step Δt are used to estimate the quaternions at $t + \Delta t$ and subsequently, the Euler angles at $t + \Delta t$. Therefore, the equations of motion become singularity-free.

3.1.7 **Steric Overlap and Cutoff Radii**

In terms of the approximations used to simulate the ferrofluid colloidal dispersion, when the method of approximation of the additivity of forces is considered, the resistance functions become considerably large as the particles approach to nearly-touching, preventing particle overlap. Conversely, the near-field mobility functions utilized by the approximation of the additivity of velocities do not exhibit this behavior. But because the method is an approximation, restrictions may be enforced. Therefore, the ferrofluid particle model has a steric layer rather than a solid one. The surfactant layer is a small fraction of the total radius of the solid portion of a particle. Mobility functions for this distinct particle have not yet been derived. However, for that reason, the mobility functions for a solid particle of diameter d are used instead. In order to apply this procedure, the hydrodynamic interactions between ferrofluid particles are neglected when the steric layers overlap. Since the repulsive influence of the overlap dominates the lubrication effect, this assumption does not disrupt the formation or development of aggregate structures. To implement this idea, when particles α and β are far enough away from each other, the introduction of a cutoff radius for hydrodynamic interactions $r_{\text{coff}}^{(\text{hydro})}$ prevents unsolicited and inaccurate aggregation behavior. This is accomplished by setting a distance where hydrodynamic interactions are ignored if the particle-particle distance $r_{\alpha\beta}$ exceeds it. Thus, the hydrodynamic interactions between particles α and β are developed while ignoring the influence of a third particle. Specifically, if α and β are far enough away from each other that a third particle positions itself between the two, the effect of particle β on particle α will be screened by the third, leading to unlikely aggregation behavior. A diagram of this is examined in Figure 1. From the illustration, particle "1" is able to interact with particle "2". However, because particle "3" is not within the cutoff radius $r_{\text{coff}}^{(\text{hydro})}$ around particle "1," it is neglected in the hydrodynamics for "1," especially

since it is screened by particle "2". Additionally, because the model consists of a strongly interacting system due to magnetostatic forces, the far-field effect eventually becomes negligible as a consequence of the cutoff radius for hydrodynamic interactions. And also, loss of the positive definiteness of the mobility matrix is typically caused by a collection of second or third nearest particles grouping around a specified particle. Considering the positive definiteness of the mobility matrix in the approximation of the additivity of velocities, we can amend any issues that could arise by respecting $r_{\text{coff}}^{(\text{hydro})}$ (Satoh *et al.*, 1998). For ferrofluids, electrorheological fluids, or other strongly interacting systems, this assumption satisfies the positive definiteness of the mobility matrix.
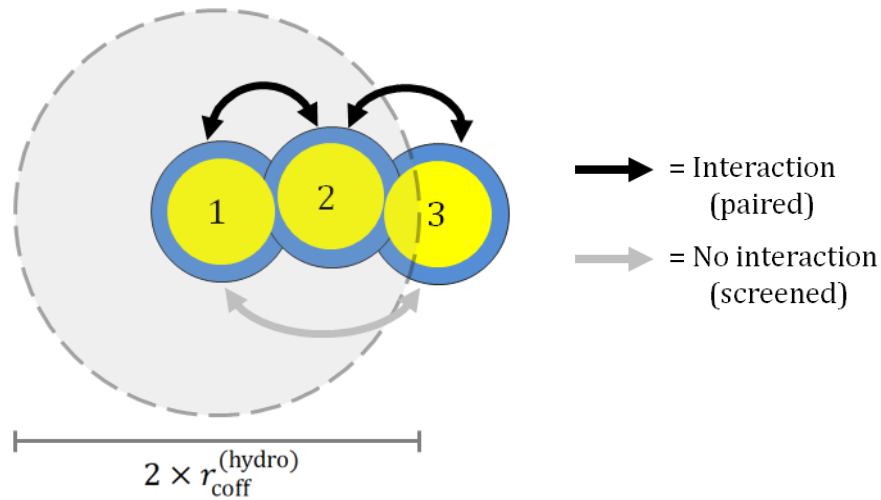
Figure 1. Cutoff radius for hydrodynamics $r_{\text{coff}}^{(\text{hydro})}$ preventing triple-particle interplay among three particles.

The general cutoff radius r_coff differs from the cutoff radius for hydrodynamic interactions, as it represents the distance where particle-particle interactions are neglected. These effects include magnetic particle-particle attraction and nonhydrodynamic interactions. Beyond r_coff , interaction energies between two particles can be considered insignificant and do not need to be calculated. Since there are typically $(N-1)$ calculations per particle for a total of $N(N-1)$ computations, the cutoff radius for particle-particle interactions drastically reduces the number of neighbors with which a particle can interact and thus, lessens the computational time. The reduction, however, is not particularly substantial considering that the model checks the distance between every particle couple to judge whether or not a pair resides within the range of r_coff . Nevertheless, a "neighbor list" algorithm may be added to further reduce the amount of calculations for r_coff .

In the event that two particles have overlap beyond their steric layers, the spheres are adjusted by:

$$\Delta \boldsymbol{r}_\alpha = \frac{\boldsymbol{d}_{\alpha\beta}}{2}\left(\frac{2}{1+d_\delta} - r_{\alpha\beta}\right) \qquad [3.49]$$

where $\Delta \boldsymbol{r}_\alpha$ is the displacement that corrects the position of particle α from particle β. The resultant configuration gives rise to two particles with only overlap of their surfactant layers, as observed in Figure 2. And steric repulsion results when surfactant layer overlap occurs, activating equation [3.23]. Equation [3.49] is a modified version of one by Heyes and Melrose (1993). They viewed a particle as a solid sphere rather than one with a steric layer. The included revision allows validation of a steric monolayer around the particles.
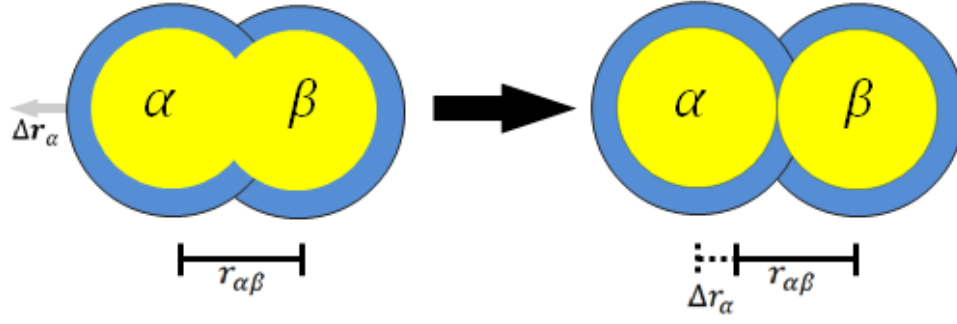
Figure 2. Steric overlap correction of particle α from particle β.

TABLE II

CUTOFF DISTANCES AND LIMITS OF PARTICLE INTERACTIONS

Interaction Range	Active Effects
$r_{\alpha\beta} < d_s$	None (due to particle-particle overlap)
$d_s < r_{\alpha\beta} < d$	Steric overlap, magnetostatic effects
$d < r_{\alpha\beta} < r_{\text{coff}}^{(\text{hydro})}$	Hydrodynamic interactions, magnetostatic effects
$r_{\text{coff}}^{(\text{hydro})} < r_{\alpha\beta} < r_{\text{coff}}$	Magnetostatic effects
$r_{\alpha\beta} > r_{\text{coff}}$	None (beyond nonhydrodynamic interactions)
$d < r_{k\alpha} < h$	Constraint procedure

The preceding limits of particle-particle interactions are summarized in Table II. In the table, $r_{k\alpha}$ is the distance from k (hereafter referred to as a "node") to particle α and h is the cutoff radius beyond which particles do not contribute to the local field.

3.1.8 **Nondimensionalization**

To nondimensionalize the model, scaling parameters for several quantities are employed: the radius a is for the length, $\dot{\gamma}^{-1}$ is for time, $\dot{\gamma}a$ is for translational velocity, the shear rate $\dot{\gamma}$ is for the rotational velocity, η is for the viscosity, $6\pi\eta\dot{\gamma}a^2$ is for force, $8\pi\eta\dot{\gamma}a^3$ is for torque, $\frac{kT}{6\pi\eta a}$ is for $\boldsymbol{D}^{\mathrm{T}}$, $\frac{kT}{8\pi\eta a^3}$ is for $\boldsymbol{D}^{\mathrm{R}}$, $\frac{kT}{4\pi\eta a^2}$ is for $\boldsymbol{D}^{\mathrm{C}}$, and $2a$ is for $\mathbf{g}$. A superscript of '$*$' indicates a dimensionless variable. By using the scaling parameters, the nondimensionalization of the force and torque equations introduced in [3.19] to [3.23] gives:

$$\boldsymbol{F}^{\mathrm{m}*}_{\alpha\beta} = -\frac{8R_{\mathrm{m}}}{r^{*\,4}_{\alpha\beta}}\left\{\begin{array}{c}-(\boldsymbol{n}_\alpha \cdot \boldsymbol{n}_\beta)\boldsymbol{d}_{\alpha\beta} + 5(\boldsymbol{n}_\alpha \cdot \boldsymbol{d}_{\alpha\beta})(\boldsymbol{n}_\beta \cdot \boldsymbol{d}_{\alpha\beta})\boldsymbol{d}_{\alpha\beta} \\ -[(\boldsymbol{n}_\beta \cdot \boldsymbol{d}_{\alpha\beta})\boldsymbol{n}_\alpha + (\boldsymbol{n}_\alpha \cdot \boldsymbol{d}_{\alpha\beta})\boldsymbol{n}_\beta]\end{array}\right\} \qquad [3.50]$$

$$\boldsymbol{T}^{\mathrm{m}*}_{\alpha\beta} = -\frac{2R_{\mathrm{m}}}{r^{*\,3}_{\alpha\beta}}\left[\boldsymbol{n}_\alpha \times \boldsymbol{n}_\beta - 3(\boldsymbol{n}_\beta \cdot \boldsymbol{d}_{\alpha\beta})\boldsymbol{n}_\alpha \times \boldsymbol{d}_{\alpha\beta}\right] \qquad [3.51]$$

$$\boldsymbol{F}^{\mathrm{h}*}_{\alpha} = \frac{4}{3}R_{\mathrm{h}}\nabla^*(\boldsymbol{n}_\alpha \cdot \boldsymbol{h}) \qquad [3.52]$$

$$\boldsymbol{T}^{\mathrm{h}*}_{\alpha} = R_{\mathrm{h}}\boldsymbol{n}_\alpha \times \boldsymbol{h} \qquad [3.53]$$

$$\boldsymbol{F}^{\mathrm{v}*}_{\alpha\beta} = R_{\mathrm{v}}\boldsymbol{d}_{\alpha\beta}\ln\left(\frac{2}{r^*_{\alpha\beta}}\right) \qquad \left(\frac{2}{1+d_\delta} \le r^*_{\alpha\beta} \le 2\right) \qquad [3.54]$$

The diffusivities become nondimensionalized through their respective scaling factors by:

$$\boldsymbol{D}^{\mathrm{T}*} = \frac{6\pi\eta a}{kT}\boldsymbol{D}^{\mathrm{T}}, \quad \boldsymbol{D}^{\mathrm{R}*} = \frac{8\pi\eta a^3}{kT}\boldsymbol{D}^{\mathrm{R}},$$

$$\boldsymbol{D}^{\mathrm{C}*} = \frac{4\pi\eta a^2}{kT}\boldsymbol{D}^{\mathrm{C}}, \quad \widetilde{\boldsymbol{D}}^{\mathrm{C}*} = \frac{4\pi\eta a^2}{kT}\widetilde{\boldsymbol{D}}^{\mathrm{C}} \qquad [3.55]$$

and the third-rank tensors become:

$$\widetilde{\mathbf{g}}^* = \frac{\widetilde{\mathbf{g}}}{2a}, \quad \widetilde{\mathbf{h}}^* = \widetilde{\mathbf{h}} \qquad [3.56]$$

Nondimensionalizing equations [3.19] to [3.23] by normalizing with the viscous force of the shear flow produces dimensionless groups of parameters. These combinations control the effect of steric,

magnetic, and Brownian influences. Varying them results in certain emphasized behaviors, which are discussed in a later section.

The scaling parameters allow nondimensionalization of equations [3.30] and [3.36] to produce the dimensionless position and angular orientation expressions. The dimensionless position is:

$$
\begin{aligned}
\boldsymbol{r}_\alpha^*(t^* + \Delta t^*) = {} & \boldsymbol{r}_\alpha^*(t^*) \\
& + \Bigg\{ \boldsymbol{U}^*(\boldsymbol{r}_\alpha^*) + \sum_{\beta=1}^{N} \boldsymbol{D}_{\alpha\beta}^{\mathrm{T}*}(t^*) \cdot \boldsymbol{F}_\beta^{\mathrm{P}*}(t^*) \\
& + 2 \sum_{\beta=1}^{N} \widetilde{\boldsymbol{D}}_{\alpha\beta}^{\mathrm{C}*}(t^*) \cdot \boldsymbol{T}_\beta^{\mathrm{P}*}(t^*) + 2 \sum_{\beta=1(\neq\alpha)}^{N} \widetilde{\mathbf{g}}_\alpha^*(t^*):\boldsymbol{\Delta}^{\infty*} \\
& + \frac{1}{\mathrm{Pe}} \sum_{\beta=1}^{N} \frac{\partial}{\partial \boldsymbol{r}_\beta^*} \cdot \boldsymbol{D}_{\alpha\beta}^{\mathrm{T}*}(t^*) \Bigg\} \Delta t^* + \Delta \boldsymbol{r}_\alpha^{\mathrm{B}*}(t^*)
\end{aligned}
\qquad [3.57]
$$

where Brownian motion is characterized by the properties:

$$
\langle \Delta \boldsymbol{r}_\alpha^{\mathrm{B}*} \rangle = 0
\qquad [3.58]
$$

$$
\langle (\Delta \boldsymbol{r}_\alpha^{\mathrm{B}*})(\Delta \boldsymbol{r}_\beta^{\mathrm{B}*}) \rangle = \frac{2}{\mathrm{Pe}} \boldsymbol{D}_{\alpha\beta}^{\mathrm{T}*} \Delta t^*
\qquad [3.59]
$$

and subsequently, the dimensionless Brownian motion term is:

$$
\Delta \boldsymbol{r}_\alpha^{\mathrm{B}*} = \sqrt{\frac{8\Delta t^*}{\mathrm{Pe}}} \, \boldsymbol{r}_n
\qquad [3.60]
$$

The dimensionless angular orientation equation is:

$$
\begin{aligned}
\boldsymbol{\varphi}_\alpha^*(t^* + \Delta t^*) = \; & \boldsymbol{\varphi}_\alpha^*(t^*) \\
& + \left\{ \boldsymbol{\Omega}^* + \frac{3}{2} \sum_{\beta=1}^{N} \boldsymbol{D}_{\alpha\beta}^{\mathrm{C}*}(t^*) \cdot \boldsymbol{F}_\beta^{\mathrm{P}*}(t^*) \right. \\
& + \frac{1}{kT} \sum_{\beta=1}^{N} \boldsymbol{D}_{\alpha\beta}^{\mathrm{R}*}(t^*) \cdot \boldsymbol{T}_\beta^{\mathrm{P}*}(t^*) + \sum_{\beta=1(\neq\alpha)}^{N} \tilde{\mathbf{h}}_\alpha^*(t^*) : \boldsymbol{\Delta}^{\infty*} \\
& \left. + \frac{3}{2\mathrm{Pe}} \sum_{\beta=1}^{N} \frac{\partial}{\partial \boldsymbol{r}_\beta^*} \cdot \boldsymbol{D}_{\alpha\beta}^{\mathrm{C}*}(t^*) \right\} \Delta t^* + \Delta \boldsymbol{\varphi}_\alpha^{\mathrm{B}*}(t^*)
\end{aligned}
\qquad [3.61]
$$

where Brownian rotation is characterized by the properties:

$$
\langle \Delta \boldsymbol{\varphi}_\alpha^{\mathrm{B}*} \rangle = 0
\qquad [3.62]
$$

$$
\langle (\Delta \boldsymbol{\varphi}_\alpha^{\mathrm{B}*})(\Delta \boldsymbol{\varphi}_\beta^{\mathrm{B}*}) \rangle = \frac{3}{2\mathrm{Pe}} \boldsymbol{D}_{\alpha\beta}^{\mathrm{R}*} \Delta t^*
\qquad [3.63]
$$

and thus, the dimensionless Brownian rotation term is:

$$
\Delta \boldsymbol{\varphi}_\alpha^{\mathrm{B}*} = \sqrt{\frac{6\Delta t^*}{\mathrm{Pe}}} \, \boldsymbol{r}_n
\qquad [3.64]
$$

Moreover the connection between the dimensionless Brownian displacement and rotation is:

$$
\langle (\Delta \boldsymbol{r}_\alpha^{\mathrm{B}*})(\Delta \boldsymbol{\varphi}_\beta^{\mathrm{B}*}) \rangle = \frac{3}{\mathrm{Pe}} \tilde{\boldsymbol{D}}_{\alpha\beta}^{\mathrm{C}*} \Delta t^*
\qquad [3.65]
$$

The dimensionless forces and torques necessary to solve equations [3.57] and [3.61] are:

$$
\boldsymbol{F}_\alpha^{\mathrm{P}*} = \sum_{\beta=1(\neq\alpha)}^{N} \left(\boldsymbol{F}_{\alpha\beta}^{\mathrm{m}*} + \boldsymbol{F}_{\alpha\beta}^{\mathrm{v}*} \right) + \boldsymbol{F}_\alpha^{\mathrm{h}*}
$$

$$
\boldsymbol{T}_\alpha^{\mathrm{P}*} = \sum_{\beta=1(\neq\alpha)}^{N} \boldsymbol{T}_{\alpha\beta}^{\mathrm{m}*} + \boldsymbol{T}_\alpha^{\mathrm{h}*}
$$

$\qquad [3.66]$

in which the individual forces and torques are drawn from equations [3.50] to [3.54].

Many dimensionless numbers result from grouping parameters and nondimensionalizing the model's equations. Quantities in equations [3.19] through [3.23] can be combined to form dimensionless groups that rely exclusively on the properties of the particles:

$$\lambda = \frac{\mu_0 m^2}{4\pi d_s^3 kT} \ , \quad \xi = \frac{\mu_0 mH}{kT} \ , \quad \lambda_v = \frac{\pi d_s^2 n_s}{2} \qquad [3.67]$$

Parameters that arise after nondimensionalization and observed in equations [3.50] to [3.54] are dimensionless groups that are defined by:

$$R_m = \frac{\mu_0 m^2}{64\pi^2 \eta a^6 \dot{\gamma}} \ , \quad R_h = \frac{\mu_0 mH}{8\pi \eta a^3 \dot{\gamma}} \ , \quad R_v = \frac{kT\lambda_v}{6\pi \eta a^2 \dot{\gamma} \delta} \qquad [3.68]$$

Here, R_m depicts the ratio of the characteristic magnetic particle-particle force to the characteristic hydrodynamic shear force, R_h represents the proportion of the characteristic particle-field torque to the characteristic hydrodynamic shear torque, and R_v signifies the ratio of the characteristic steric repulsion force to the characteristic hydrodynamic shear force. One should notice that these dimensionless groups are inversely proportional to the shear rate. They will later prove significant in managing specific effects on the particles. From the dimensionless Brownian translation and rotation in equations [3.57] and [3.61], respectively, the Péclet number appears:

$$Pe = \frac{6\pi \eta a^3 \dot{\gamma}}{kT} \qquad [3.69]$$

The Péclet number, like the prior three, is a ratio. It embodies the proportion of characteristic hydrodynamic shear force to the characteristic Brownian motion force.

The values in equation [3.67] are combined with the dimensionless groups in equation [3.68] to form ratios of dimensionless numbers:

$$\frac{R_h}{R_m} = \frac{\xi(1+d_\delta)^3}{4\lambda} \ , \quad \frac{R_v}{R_m} = \frac{\lambda_v(1+d_\delta)^4}{3\lambda d_\delta} \ , \quad \frac{1}{R_m Pe} = \frac{(1+d_\delta)^3}{3\lambda} \qquad [3.70]$$

It should be noted that from this equation, the ratios of R_h/R_m, R_v/R_m, and $1/R_\text{m}\text{Pe}$ depend only on the properties of the particle and not on those of the flow. In addition, R_h/R_m is the ratio of particle-field effects to particle-particle effects, the R_v/R_m ratio compares the steric interactions to magnetic particle-particle interactions, and $1/R_\text{m}\text{Pe}$ characterizes the thermal forces to the magnetic particle-particle effects. The assignment of these ratios is significant when preparing to execute the simulation.

3.2   **Principles of Magnetism**

3.2.1   **Maxwell's Equations**

Steady-state ferrofluids are governed by certain guidelines and must conserve essential principles of physics. When electricity (i.e. field, current) is not present, diffusion is described by magnetostatics. The present Brownian dynamics system should maintain a free magnetic field while remaining current-free throughout the volume. These concepts are embodied by the magnetostatic form of the Maxwell's equations:

$$\nabla \cdot \boldsymbol{M} = -\nabla \cdot \boldsymbol{H} \qquad\qquad [3.71]$$

$$\nabla \times \boldsymbol{H} = \boldsymbol{0} \qquad\qquad [3.72]$$

where $\boldsymbol{M}$ was identified as the volume average of the particle dipoles known as magnetization and $\boldsymbol{H}$ was defined as the magnetic field. Note that the divergence of the system's magnetization will be zero if the particle magnetizations are uniform and no internal field variations exist across the particle volumes.

3.2.2 **Magnetization**

To quantify the magnetization at any point in the system, a symmetric, radial weighting function W is used (Nitsche and Zhang, 2002):

$$W(\boldsymbol{v}, h) = 1 - 3\left(\frac{\|\boldsymbol{v}\|}{h}\right)^2 + 2\left(\frac{\|\boldsymbol{v}\|}{h}\right)^3 \qquad [3.73]$$

Here, $\|\boldsymbol{v}\|$ is the norm of the vector $\boldsymbol{v}$. The weighting function is used to calculate the magnetization via:

$$\boldsymbol{M}(\boldsymbol{r}) = \frac{1}{V}\sum_{\alpha}^{N} \boldsymbol{n}_\alpha W(\boldsymbol{v}, h) \qquad [3.74]$$

where $\boldsymbol{r}$ is the position at which the $\boldsymbol{M}$ field is being evaluated and V is the volume of the magnetized source. In this model, $\boldsymbol{v}$ is the vector between particle α and position $\boldsymbol{r}$.

3.2.3 **Magnetic Field**

The magnetic field $\boldsymbol{H}$ of the ferroparticle system is calculated as:

$$\boldsymbol{H} = \boldsymbol{H}_0 + \hat{\boldsymbol{H}} \qquad [3.75]$$

where $\boldsymbol{H}_0$ is the external magnetic field in the absence of magnetic material and is assigned in the model as:

$$\boldsymbol{H}_0 = \begin{cases} H\boldsymbol{e}_y & \text{, if uniform} \\ H\left[\left(-\dfrac{r_x}{C_L} + C_x\right)\boldsymbol{e}_x + \left(\dfrac{r_y}{C_L} + C_y\right)\boldsymbol{e}_y\right] & \text{, if nonuniform} \end{cases} \qquad [3.76]$$

in which $\boldsymbol{e}_x$ and $\boldsymbol{e}_y$ are unit directional vectors, H is the magnitude of the magnetic field strength, and C_L, C_x, and C_y are constants. In order to adhere to the principle of magnetostatics, the magnetic field should be consistent with the form of Maxwell's equations of a static field in an electrically nonconducting carrier liquid. The second term in equation [3.75] is the demagnetizing

field $\widehat{H}$. The external field generated by a spherical particle that is homogeneously magnetized is identical to that of a point dipole possessing the same total magnetic moment and originating from the sphere's center. Furthermore, the magnetic field at any arbitrary position can be acquired by assuming superposition of the fields. Thus, if particle α is within the proper range, the $\widehat{H}$ field will be calculated as:

$$\widehat{H}(r) = \sum_{\alpha}^{N} \frac{V}{4\pi|r - r_\alpha|^3} \left[-M + \frac{3[M \cdot (r - r_\alpha)](r - r_\alpha)}{|r - r_\alpha|^2} \right] \qquad [3.77]$$

where r is the position at which the $\widehat{H}$ field is being evaluated, r_α represents the vector to particle α, and V is the volume of the magnetic source centered at r. The magnetization introduced in equation [3.74] is utilized. It should be noted that the effect of the $\widehat{H}$ field is dependent on the distance to particle α from position r. As observed in equation [3.77], the effect of the field at r drops off as $|r - r_\alpha|^{-3}$.

Ultimately, one can conclude that the ferrofluid particles within the system, when manipulated by an applied magnetic source, contribute to the effective magnetic field. Only when the particles lose their magnetization and the external magnetic field is absent will $H = 0$. Otherwise, the model considers the contributions to H, even if the magnetic field is uniform (H_0 = constant).

3.2.4 **Uniform Magnetic Fields and Aggregation**

The particle-particle attraction in equation [3.19] drives the formation of chains and the aggregation behavior under uniform magnetic fields is engaged. As one can detect upon inspection of the first component in equation [3.76], when the externally-applied magnetic field is uniform, the gradient of h in equation [3.21] is zero and thus, the force due to the applied magnetic field is

disregarded in the model. During aggregation, the magnetic energy of ferroparticles achieves a peak when their moments are situated parallel to both the magnetic field and the vector connecting to another particle. Additionally, magnetoviscous effects are known to intensify with higher degrees of particle chaining. In terms of hydrodynamic interactions, however, interplay between adjacent chains (i.e. perpendicular attraction) has not proven to be a prevailing factor in ferrofluid dynamics (Zubarev, 2013).

3.2.5 **Magnetoviscous Effects**

In respect to fluid properties, ferrofluids generally possess non-Newtonian characteristics as a result of their colloidal nature. Their aggregates influence the fluid properties because of their strict compliance towards the external magnetic field. It is not just affected by the resistance caused by rotation of individual ferroparticles. Plus, unlike the viscosity of pure liquids, the viscosity of a ferrofluid typically depends on the shear rate (Odenbach, 2002). Therefore, in order to observe the effect of aggregates, the significance of the magnetic contributions to the viscosity is explored while disregarding the particle stresslet elements. Consequently, the component of the viscosity that is due to magnetic and steric interactions is:

$$\eta^{\mathrm{m}*} = \frac{\eta^{\mathrm{m}}}{\eta} = -\frac{6\pi}{L^{*3}} \sum_{\alpha=1}^{N} \sum_{\substack{\beta=1 \\ (\beta>\alpha)}}^{N} r_{\alpha\beta y}^{*} F_{\alpha\beta x}^{\mathrm{P}*} + \frac{4\pi}{L^{*3}} \sum_{\alpha=1}^{N} T_{\alpha z}^{\mathrm{P}*} \qquad [3.78]$$

Here, $\eta^{\mathrm{m}*}$ is referred to as the dimensionless viscosity contribution caused by magnetic effects. The expressions in [3.66] are applied for the dimensionless forces and torques. On the right-hand side of the above equation, the first term is a result of the magnetic and steric forces amongst the particle monolayers while the second term is caused by the torques on the particles, which includes

the influence of the applied magnetic field. Thus, in this case, forces and torques are adequate when characterizing the impact of the motion of the particle on the fluid.

3.2.6 **Nonuniform Magnetic Fields and Magnetophoresis**

When the nonuniform field in equation [3.76] is active, the particles experience the magnetophoretic force of equation [3.21]. The magnetic field and its gradient are necessary elements required to interpret the primary magnetophoretic driving force. In order to accomplish favorable magnetic separation, the magnetic force must overcome thermal fluctuations and the magnetic field source must induce large enough magnetizations to prompt sufficient MP. Besides, the farther a particle is located from the origin point of the magnetic field, the lower the influence of the force and gradient from the magnetic source.

The constants of C_L , C_x , and C_y in equation [3.76] will be appointed so that the magnetic field gradient is intentionally situated to steer the magnetic material towards the upper wall of the channel. The nonuniform magnetic field expression in equation [3.76] was devised so as to be solenoidal, which will facilitate calculations during the constraint stage of the model. Moreover, control of particle diffusion will be promoted by tweaking various parameters. For example, an optimal suspension for biomedical applications would have particles that readily conform to the magnetic field with minimal agglomeration (and consequent magnetoviscous effects would be ineffectual). This would be carried out by implementing low particle-particle interactions and high responsiveness to an externally-applied magnetic field gradient, both of which can be calibrated in this study.

3.3   **Magnetic Separation**

3.3.1   **Magnetic Separation Modeling**

This research aims to provide important insight into magnetic separation and discover practical correlations between physical characteristics and transport behaviors. So as long as the magnetophoretic velocity can be reasonably described, dimensionless number analysis can provide insight into how physical properties are affected by MP. Dimensionless number analysis provides a quick, dependable approach to studying the MP behavior of ferrofluid particles, particularly those under LGMS (Lim *et al*., 2014). Proper control of the dimensionless numbers can reveal enlightening connections between fluid flow, Brownian motion, particle-particle interactions, MP, and the properties of the nanoparticle (especially its size).

Since analytical solutions to describing the full kinetics of MP have not yet been well-established, mesoscale models have been an effective approach to interpreting magnetic nanoparticle aggregation and MP (Faraudo *et al*., 2013). Rather than studying the noncooperative behavior of individual particle trajectories, this study focuses on cooperative magnetic particle separation. Under specified conditions and parameters (established in a later section), one can assume that the magnetophoretic separation is mainly operated by the movement of clusters resulting from particle-particle interactions rather than by single components. Thus, cooperative particle grouping seems instinctively more reliable for this research because of the dependence on aggregating particle trajectory tracking under magnetic and hydrodynamic interactions. The need for incorporating means to handle the aggregation behavior and define explicit cooperative magnetophoretic effects has been a prominent issue of MP (Miguel and Pastor-Satorras, 1999).

The present work addresses magnetic separation subjected to an externally-applied magnetic field gradient via numerical modeling so as to comprehend the magnetophoretic behavior

of particulate ferrofluid suspensions in simple shear flow. The general geometry studied in this model can be visualized as the separation region of a microchannel separator, like those of an L- or T-shaped design (Wu *et al*., 2011), or as continuous flow particle sorting separation systems (Suwa and Watarai, 2011). For successful magnetic separation, the magnetophoretic force must dominate diffusive, drag, gravitational, and inertial forces. To measure the progress and effectiveness of magnetic separations, separation efficiencies and separation times are collected.

3.3.2 **Separation Efficiency**

Separation (or capture) efficiency Φ quantifies the extent of magnetic particle separation (ranging anywhere from 50% up to 100% accumulation in a specific region or location). It evaluates the proportion of separated to unseparated constituents until the separation time is reached. The ultimate goal of magnetic separation is high (if not complete) separation efficiency. With respect to the dimensionless number analysis, a favorable fraction of the suspension within a fixed expanse alongside the magnetic source boundary will be monitored under various stimuli, which involve varied particle-particle interactions, magnetic field strengths, and various shear flowrates. Particles are deemed "captured" when they drift beyond an explicit coordinate or plane. Typically, there is an area below this coordinate and far from the wall that is considered as a "wash away" region, where particles that are not in the concentrated zone near the wall are overcome with shear effects. Since these particles are not within range of magnetic influence to maintain their diffusion towards higher magnetism, they are considered "uncapturable" because they did not enter the channel inside the bounds of the capture threshold, a domain where particles are constantly dominated by forces other than MP. If a capture threshold exists, particle trajectories can usually be traced to evaluate separation efficiency, so long as the initial position of entry into

the channel is known. For now, however, any particles lost from fluid flow are retained, especially with the model's periodic boundaries and under high magnetic field gradients. And since few studies exist that analyze the optimization of intricate microchannel configurations for higher separation efficiency, the researchers have designed this model so that the simulation should be capable of accommodating inhomogeneities in the magnetic fields or across the suspension. This is an aspect that analytical solutions or homogeneous models are unable to accomplish without the assistance of piecewise functions or finite element analysis.

3.3.3 **Separation Times**

Separation time t_S measures the elapsed duration needed to attain a desirable degree of separation efficiency. It can be contingent on particle size, magnetic properties, applied field gradients, or concentration, depending on active suspension behaviors. Ongoing MP research calculates the separation time as a power law dependency (usually with particulate concentration) or as a direct relation to magnetic susceptibility and particle size (Suwa and Watarai, 2011). Because of the complicated reliance on the magnetic behavior, particle properties, and aggregation activity, separation trends are sometimes scaled by a common factor that is related to the magnetism on the magnetic particles (Schaller *et al*., 2008). For most commercial ferrofluids, separation time drops with increasing particle size or concentration and decreasing separation distance between particles. In most cases, if the product between particle size and concentration is kept constant, the anticipated separation time can be certainly reached. For this study, the separation time t_S is evaluated at the moment the model reaches full separation efficiency. Specifically, time t will elapse until the magnetic dispersion concentration at the designated

expanse bordering the wall adjacent to the magnetic source has reached a favorable ratio of the initial suspension density corresponding to the pertinent separation efficiency Φ.

3.4 **System subject to Constraints**

3.4.1 **Method of Constraints**

In order to respect the postulates discussed above in equations [3.71] and [3.72], the Brownian dynamics system adopts constraints to conserve them. Constraints are occasionally applied to particulate simulations in order to satisfy specified conditions. Ottinger (1996) explains approaches to applying constraints with stochastic differential equations (SDE), the Fokker-Planck equation, and numerical integration schemes. A functional constraint method for molecular dynamics was developed by Ryckaert *et al*. (1977), in which the equations of motion are solved simultaneously with the constraint mechanism at every time-step of the integration. The same method can be applied to a Brownian dynamics model. Liu (1989) employed a constraint procedure to a Brownian dynamics simulation in order to estimate rheological properties of Kramers freely-jointed bead-rod polymer chains. The constraints were employed to maintain constant lengths and angles. Therefore, while the present ferrofluid develops unconstrained in a simple shear flow and applied magnetic field, constraints will restructure the system to satisfy the conditions. In other words, the constraint method will "correct" the particles and prevent the model from diverging towards unrealistic behavior. Since there are two principles that need to be satisfied, a single constraint method such as the one used for polymeric fluids by Liu (1989) would be insufficient for this design.

The process used to constrain the Brownian dynamics simulation is an iterative scheme that utilizes Lagrange multipliers. In this procedure, the system is allowed to take an unconstrained time-step. Then, the coordinates of the particles will be modified via:

$$\boldsymbol{q}_\alpha^{\text{CON}} = \boldsymbol{q}_\alpha^{\text{UN}} + \sum_{j=1}^{d'} \gamma_j \frac{\partial \sigma_j}{\partial \boldsymbol{q}_\alpha} \qquad [3.79]$$

where $\boldsymbol{q}_\alpha^{\text{CON}}$ and $\boldsymbol{q}_\alpha^{\text{UN}}$ are the constrained and unconstrained generalized coordinates, respectively, and d' is the number of constraints. The second term on the right-hand side of the above equation represents the correction due to the constraint.

To authorize the correction, the system must first meet the conditions of d' holonomic constraints defined by:

$$\sigma_j(\{\boldsymbol{q}_v\}) = f(\boldsymbol{q}_1, \boldsymbol{q}_2, \cdots, \boldsymbol{q}_N) = 0 \qquad (j = 1,2,\cdots,d') \qquad [3.80]$$

in which $\boldsymbol{q}_v$ is the coordinate of particle $v = 1,2,\dots,N$ and f is a constraint function dependent on the configuration of the system. To achieve fulfillment of the constraints, an optimized solution of equation [3.80] is determined iteratively via scalar Lagrange multipliers:

$$\gamma_j = \sum_{l=1}^{d'} [\tilde{g}_{jl}]_{c'} \sigma_l \qquad (j = 1,2,\cdots,d') \qquad [3.81]$$

where the $d' \times d'$ matrix $\tilde{g}_{jl}$ is the inverse of the modified metric matrix $\tilde{G}_{jl}$ and satisfies:

$$\sum_{m=1}^{d'} \tilde{g}_{jm} \tilde{G}_{ml} = \delta_{jl} \qquad [3.82]$$

The modified metric matrix is:

$$\tilde{G}_{jl} = \sum_{\alpha=1}^{N} \frac{\partial \sigma_j}{\partial \boldsymbol{q}_\alpha} \cdot \frac{\partial \sigma_l}{\partial \boldsymbol{q}_\alpha}$$

The brackets $[\cdots]_{c\prime}$ around matrix $\widetilde{\boldsymbol{g}}$ in equation [3.81] serve as an evaluation range for position from time t to time $t + \Delta t$, manifested as $c\prime \in [0,1]$. The Lagrange multipliers are computed such that at each time-step, the constraints arrive within a suitable, specified tolerance.

3.4.2 **Preparing Maxwell's Equations for the Constraint Algorithm**

The laws discussed in equations [3.71] and [3.72] will function as the constraints and are first established by means of integral theorems. The postulate in equation [3.71] is better organized using a volume integral:

$$\sigma_G = \iiint\limits_V (\nabla \cdot \boldsymbol{M})\, dV + \iiint\limits_V (\nabla \cdot \boldsymbol{H})\, dV \qquad [3.83]$$

The integrals above suggest that integrating across a volume for an abundant number of ferroparticles would be inefficient. Consequently, the above volume integral expression can be simplified further using the Gauss-Ostrogradskii Divergence Theorem to eliminate the need to take the direct divergence of the fields:

$$\sigma_G = \oiint\limits_S (\boldsymbol{M} \cdot \widehat{\boldsymbol{n}})\, dS + \oiint\limits_S (\boldsymbol{H} \cdot \widehat{\boldsymbol{n}})\, dS \qquad [3.84]$$

where $\widehat{\boldsymbol{n}}$ is the surface normal vector and the volume integral has been reduced to a surface integral. In order to numerically calculate the integral, a zero-order approximation of this calculation is prepared:

$$\sigma_G = \sum_k (\boldsymbol{M}_k \cdot \widehat{\boldsymbol{n}})\Delta S_k + (\boldsymbol{H}_k \cdot \widehat{\boldsymbol{n}})\Delta S_k \qquad [3.85]$$

where $\boldsymbol{M}_k$ and $\boldsymbol{H}_k$ are the magnetization field and magnetic field, respectively, centered at node k. If the nodes are placed in a uniform grid on each surface of a local cubic constraint volume,

then the differential area ΔS_k will be constant for all k nodes and the integration can be rewritten as:

$$\sigma_G = \Delta S \sum_k M_k \cdot \hat{n} + H_k \cdot \hat{n}$$ [3.86]

Thus, the constraint in equation [3.71] is assessed on an average basis, as opposed to evaluating it at every possible spatial point. Figure 3a depicts a constraint volume for this particular notion.
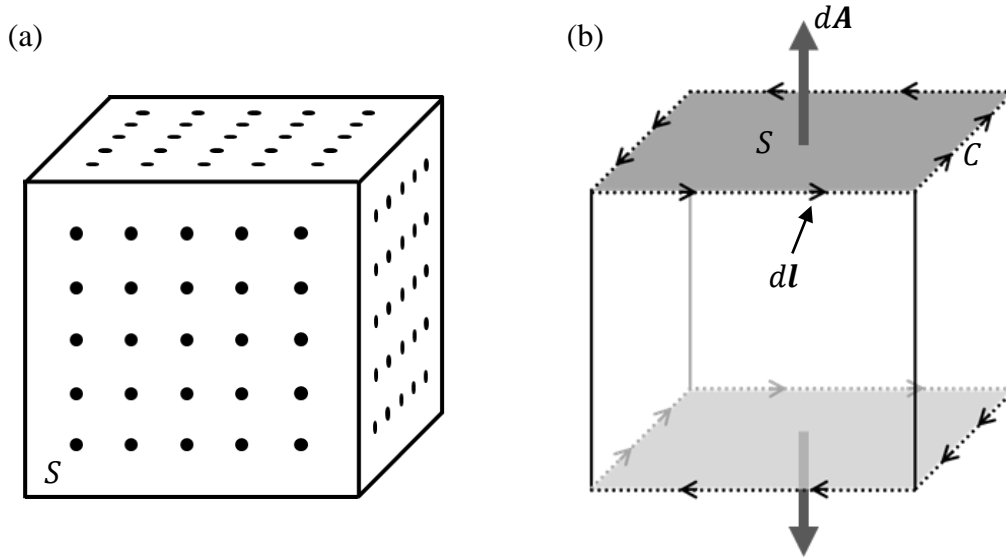
Figure 3. (a) Constraint volume for Gauss's Law with uniformly distributed nodes on the surfaces S and (b) constraint surfaces S for Ampère's Law showing linearization along C (dotted lines).

To satisfy the magnetostatic Ampère's Law in equation [3.72], one can impose the constraint by applying a surface integral over it:

$$\sigma_A = \iint\limits_S \text{curl}(\boldsymbol{H}) \cdot d\boldsymbol{A}$$

$$= \iint\limits_S (\nabla \times \boldsymbol{H}) \, d\boldsymbol{A}$$

[3.87]

where $d\boldsymbol{A}$ is the normal vector to the surface. Application of a surface integral allows for the use of Stokes' Theorem to bypass the prospect of explicitly solving the curl of the $\boldsymbol{H}$ field:

$$\sigma_A = \oint\limits_C \boldsymbol{H} \cdot d\boldsymbol{l}$$

[3.88]

where C is the curve that is capped by surface S and $\boldsymbol{l}$ is the position vector function (or the parametrization) that defines the path along C. The normal direction to the surface S dictates the positive orientation of curve C, as observed in Figure 3b. Equation [3.88] can be numerically calculated by a zero-order approximation:

$$\sigma_A = \sum_{k'} \boldsymbol{H}_{k'} \cdot \Delta \boldsymbol{l}$$

[3.89]

where $\Delta \boldsymbol{l}$ is the change in the linearization along C. At each node k' located on the path of $\boldsymbol{l}$ along C, the effective field $\boldsymbol{H}$ in equation [3.88] is evaluated using equation [3.77]. And similar to the Gauss's Law, the constraint in equation [3.72] is estimated on an average basis, rather than for every possible spatial point.

Initial examination of equation [3.81] reveals that each constraint is paired with its own Lagrange multiplier that must be iterated upon. Attempting to fulfill the constraints in equations [3.86] and [3.89] at a large number of nodes throughout the system's volume would therefore lead to slow computational schedule. In order to alleviate this issue, the constraint is not

met explicitly at every point but rather on average within the system, as outlined above. The integral theorems and numerical approximations used to simplify the constraints bring about a significant decrease in the number of nodes, thus reducing computation time. Furthermore, the weighting function allows for a spatially continuous density measurement along the node points. Ideally, more nodes could be added, further reducing the size of the "sub-cells," allowing the constraint to be met in smaller and smaller volumes and ultimately leading to a more accurate picture of the system's behavior. However, the model will consider a low number of constraints in consideration of computational limits. Moreover, when designating an externally-applied magnetic field H_0, any field can be utilized. Still, to simplify the computations, the particular H_0 field (specified in equation [3.76]) was chosen because the curl and divergence are both zero. Therefore, H_0 is neglected in the constraint calculations and equations [3.83] and [3.87] require only the divergence and curl of the remaining contributions.

3.4.3   <u>**Constraints on the Particle's Center of Mass and Dipole Orientation**</u>

While the constraint σ_j is progressing towards a reasonable solution via the Lagrange multiplier process, the center of mass positions and dipole orientations of the particles are adjusted. The constrained center of mass position of particle α is:

$$r_\alpha^{\text{CON}}(t + \Delta t) = r_\alpha^{\text{UN}}(t + \Delta t) + \beta \, \Delta t D_o^t F_\alpha^{\text{CON,T}} \qquad [3.90]$$

with r_α^{UN} as the unconstrained center of mass position of particle α introduced in equation [3.30], $\beta = \frac{1}{kT}$, Δt as the time-step, and D_0^t as the translational diffusion coefficient at infinite dilution. Under convergence conditions, the correction term observed in equation [3.79] can pose as a

constraint force for the center of mass of particle α:

$$\boldsymbol{F}_\alpha^{\text{CON,T}} = -\sum_j^{d'} \gamma_j \frac{\partial \sigma_j}{\partial \boldsymbol{r}_\alpha} \qquad [3.91]$$

The appropriate derivatives are required to process this equation and are provided in Appendix B. The constrained dipole orientation for particle α:

$$\boldsymbol{\varphi}_\alpha^{\text{CON}}(t + \Delta t) = \boldsymbol{\varphi}_\alpha^{\text{UN}}(t + \Delta t) + \beta \Delta t D_o^r \boldsymbol{T}_\alpha^{\text{CON}} \qquad [3.92]$$

where $\boldsymbol{\varphi}_\alpha^{\text{UN}}$ is the unconstrained dipole orientation of particle α presented in equation [3.36] and D_0^r is the rotational diffusion coefficient at infinite dilution. In this case, the correction term of equation [3.79] is posed as a constraint torque for the dipole orientation of particle α:

$$\boldsymbol{T}_\alpha^{\text{CON}} = \boldsymbol{r}_\alpha^{\text{UN}}(t) \times \boldsymbol{F}_\alpha^{\text{CON,R}}(\boldsymbol{\varphi}_\alpha, \gamma_j) \qquad [3.93]$$

However, rather than applying the orientational constraint force $\boldsymbol{F}_\alpha^{\text{CON,R}}$ to the particle's center of mass position, it should be related to the dipole orientation. $\boldsymbol{F}_\alpha^{\text{CON,R}}$ can be written:

$$\boldsymbol{F}_\alpha^{\text{CON,R}} = -\sum_j^{d'} \gamma_j \frac{\partial \sigma_j}{\partial \boldsymbol{\varphi}_\alpha} \qquad [3.94]$$

and uses the partial derivative of the constraint with respect to $\boldsymbol{\varphi}_\alpha$, of which are provided in Appendix B. The correction stemming from this does not imply that a constraint force shifts $\boldsymbol{\varphi}_\alpha$ to a new spatial position. Instead, $\boldsymbol{F}_\alpha^{\text{CON,R}}$ is used in conjunction with $\boldsymbol{T}_\alpha^{\text{CON}}$ to pivot $\boldsymbol{\varphi}_\alpha$ toward satisfaction of the constraint while simultaneously remaining at $\boldsymbol{r}_\alpha$. Adopting a constraint force to spatially reposition $\boldsymbol{\varphi}_\alpha$ would disagree with the one that controls $\boldsymbol{r}_\alpha$ since the dipole's resultant Cartesian position would not match the particle's constrained center of mass location.

With an outlined constraint procedure, the Maxwell's equations in [3.71] and [3.72] will be satisfied for the ferrofluid system at each time-step. When equations [3.90] and [3.92] are inserted into the constraint equations, a set of d' nonlinear equations with d' unknown Lagrange

multipliers is formed. The equations are solved iteratively with initial Lagrange multiplier values of $\gamma_j = 0$. For every time-step Δt that transpires, the iterative constraint method converges when the second term of the right-hand sides of equations [3.90] and [3.92] approach zero for all σ_j. As a consequence, the simulation can advance because the correction term is no longer needed. The particle arrangement is then finalized and the system repeats the process at time $t + \Delta t$.

4. SIMULATION PROCEDURE

4.1   Particle and System Setup

In the present model, ferrofluid particles are scrutinized under various conditions, notably under a simple planar shear flow. A collection of dipoles is randomly distributed within a simulation cube of dimension L, as portrayed in Figure 4. In this research, the constituents are not intended to represent perfectly genuine ferrofluid nanoparticles but to act as tracers that can replicate the dynamics of magnetic particles under the specified conditions. The model can be viewed as a system of secondary particles, each of which is comprised of many primary ones. Each dipole is envisioned as a sphere of radius a because of its relatively simple geometry and appearance in many colloidal systems. Spheres are known to facilitate complicated numerical techniques, even those designed with a uniform steric layer. For a spherical particle housing a fixed dipole, the orientation of strongest attraction is when dipoles are parallel, meaning the ends are attracted to their corresponding opposites. Thus, perpendicular attraction is dismissed.
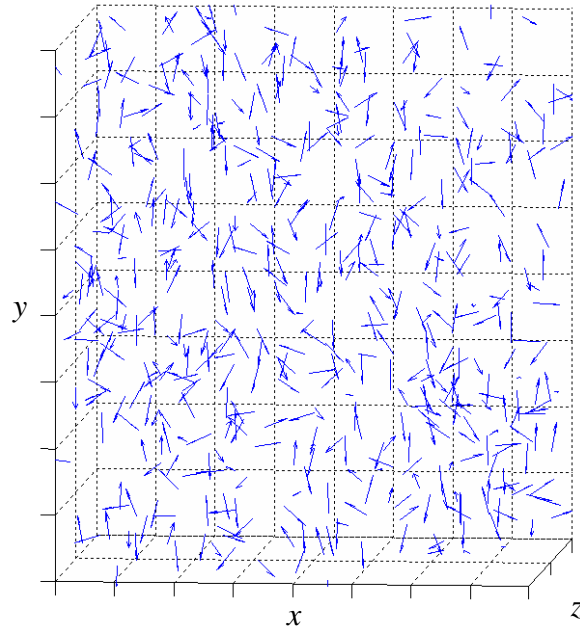
Figure 4. Initial setup of randomly positioned and
oriented magnetic dipoles.

Each spherical particle must be assessed at a reasonable size that is characteristic of
ferrofluids. As discussed previously, typical ferrofluid particles measure to within 4 to 9 nm in
diameter. For a ferrofluidic colloidal dispersion in a simulation cube, the volume fraction of solid
to fluid component is expressed as:

$$\phi = \frac{N}{L^3}\left(\frac{\pi d^3}{6}\right) \qquad [4.1]$$

Typical ferrofluids are usually produced with a number density of roughly 10^{23} particles per cubic
meter, a value of which induces a volume fraction of:

$$\phi = 10^{23}\left(\frac{\pi d^3}{6}\right) \qquad [4.2]$$

When boundary walls are introduced in the simulation, there is additional fluid present in the grooves between the wall particles. The volume fraction must then adjust to account for the supplementary fluid:

$$\phi = \frac{N}{L^3 + \frac{N_w}{4}\left(1 - \frac{\pi}{3}\right)d^3}\left(\frac{\pi d^3}{6}\right) \qquad [4.3]$$

in which N_w is the total number of wall particles, derived as:

$$N_w = \frac{L^2}{2d^2} \qquad [4.4]$$

If $N = 512$ and $L = 40a$, then $N_w = 200$ and, by using equations [4.2] and [4.3], solving for the particle size results in $d \approx 8.6$ nm, a value of which falls within the aforementioned particle size range. Concerning MP, the particle size limit at which Brownian motion will most likely force nanoparticles to break away from the influence of magnetic forces has been found to be around 5 nm (Friedman and Yellen, 2005). This is true for almost all shapes and thus, functions for biological elements like red blood cells.

4.2   **Wall Boundary Condition Setup**

To simulate a ferrofluid system between parallel plates, wall boundaries must be implemented. Two commonly used boundary models are known to imitate a solid boundary: the ideal smooth wall model and the particle-wall model. In this study, the particle-wall design is valuable for its ability to mimic solid boundary roughness in a simplistic manner, both methodically and computationally. Hence, the top and bottom *xz*-planes (located at $y = \pm 20a$) are composed of wall particles. The wall particles are set in a hexagonal packing arrangement of identical circles of radius a (when viewed in a two-dimensional plane) and are constrained from repositioning relative to one another. The wall particles are arranged in a layer with the same

thickness as the ferrofluid particles. When shear flow is active, the particles in the wall layers shift according to the shear velocity, set equal to a specified wall velocity. Because of the boundary, the ferrofluid particles are contained within the limits of the *y*-direction but are free to move between the parallel plates. The particles are prevented from breaching the wall by introducing the algorithm:

$$\Delta \boldsymbol{r}_\alpha = 2(2\boldsymbol{d}_{w\alpha} - \boldsymbol{r}_{w\alpha}) \qquad [4.5]$$

where $\Delta \boldsymbol{r}_\alpha$ is the displacement that corrects the position of particle α from the wall and $\boldsymbol{d}_{w\alpha}$ is the unit direction vector from wall particle w to particle α. However, since the wall particles are set in a hexagonal packing arrangement, a slightly modified strategy is required to account for the spaces between them. The modified procedure would shift the particle away from the wall and reflect it in the *y*-direction while its momentum is maintained in the *x*- and *z*-directions. Figure 5 demonstrates the application of the wall boundary. When a particle α overlaps the wall, the adapted method activates by analyzing the overlap distance $r_{y,over}$ of the nearest wall particle. Then, the separation is used as the reflective *y*-direction distance from the wall while maintaining the displacements in the other Cartesian directions. The *y*-component of velocity will also be reversed. It will appear as if the particle rebounded off the wall in lieu of overlapping with the wall particles. Additionally, when a particle is equally separated between three wall particles, a small bit of space allows a portion of the particle to "sink" into the wall without overlapping the wall particles. Accordingly, the minimum *y*-distance from the center of a ferrofluid particle to the center of any of the three wall particles is:

$$\Delta r_{y,min} = \frac{2a}{3}\sqrt{6}$$

Any separation less than this limit indicates overlap of the ferrofluid particle and the wall. This

was mentioned to explain the size of the grooves between wall particles and the ambient fluid that would occupy them.
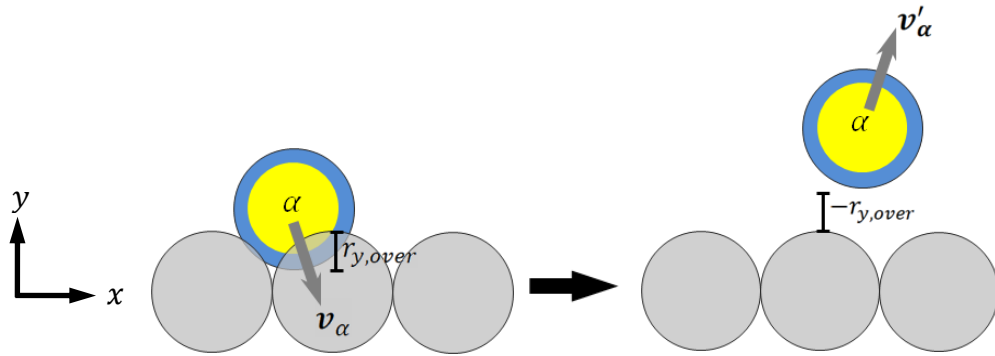
Figure 5. Activation of the boundary wall procedure due to particle intrusion into the wall (observed in the *xy*-plane).

Conversely, where there is no wall boundary, the system is considered to have a periodic boundary. The simulation cube has been defined to have periodic boundaries in the *x*- and *z*-directions, permitting the particles to diffuse freely in a continuous fluid. The boundaries are periodic because the particle concentration at the wall would infinitely increase. The number of particles remains constant within the volume in order to simulate a collection process under nonuniform fields.

4.3   **Time-steps**

So that the model remains within sensible limits and to prevent divergence, the maximum

Brownian displacement was kept significantly lower than the steric layer thickness:

$$\left|\Delta r_{\alpha}^{\mathrm{B}*}\right|_{max} = \sqrt{\frac{8\Delta\tau^*}{\mathrm{Pe}}} = 0.2d_{\delta} \qquad [4.6]$$

The characteristic time for the fluid's molecular motion is much shorter than that for the movement

of ferrofluid particles. This is because the colloidal particles are much larger than those of the

solvent. Therefore, the molecular motion of the solvent is viewed as a continuum and the

contributions due to them are absorbed into the stochastic term of equation [3.24]. Solving for $\Delta\tau^*$

in equation [4.6] leads to an expression for the characteristic time for shear flow:

$$\Delta\tau^* = 0.005d_{\delta}^2\mathrm{Pe} \qquad [4.7]$$

The time-step interval Δt^* should be much shorter than $\Delta\tau^*$, so a condition is instated to verify

that the lowest value is always designated for the time-step:

$$\Delta t^* = min(0.0001, \Delta\tau^*) \qquad [4.8]$$

This prerequisite to the model ensures that the solid parts of particles do not overlap each other or

penetrate the wall. The time-step also considers that the particle travels much less than a fraction

of a particle radius over one time increment.

4.4   **Magnetic Field Setup**

The primary magnetic field directionality is chosen to be in the positive *y*-direction, selected specifically to emulate MP (and elicit magnetic separation) in the presence of a nonuniform field. And although an *x*-component exists in the event of a nonuniform field, the *z*-components are absent in the applied magnetic fields of equation [3.76]. For a simplistic, uniform, externally-applied magnetic field, a two-dimensional vector field representation is rendered in Figure 6a. The particles under the influence of a uniform magnetic field form aggregates along the *y*-direction with dipoles pointing in the primary field direction. Under a nonuniform, externally-applied magnetic field, aggregates may form but particles are primarily expected to gather at the wall boundaries. To attain a field that would accomplish this, the magnetic field constants in equation [3.76] are set to $C_L = 100$, $C_x = 0$, and $C_y = 0.8$. The corresponding two-dimensional $\boldsymbol{H}_0$ field lines are portrayed in Figure 6b. Aminfar *et al*. (2013) also provide an informative representation of the magnetic strength contours of a similar magnetic field. Ultimately, asymmetrical particle accumulation will transpire because the field induces a gradient that forces the particles to diffuse towards the wall at $y = +20a$. Also, under these conditions, one could assume that the proposed system could be viewed as an annulus between two concentric rotating cylinders. And so, while a uniform magnetic field leads to data that interprets aggregation behavior amongst ferrofluid particles, applications with nonuniformly applied magnetic fields will facilitate the ongoing research in magnetophoretic properties of said constituents.

(a)

Uniform H_0 field $(0,h,0)$

(b)

Non-uniform H_0 field $(C_L=100, C_x=0, C_y=0.8)$

y

x

y

x
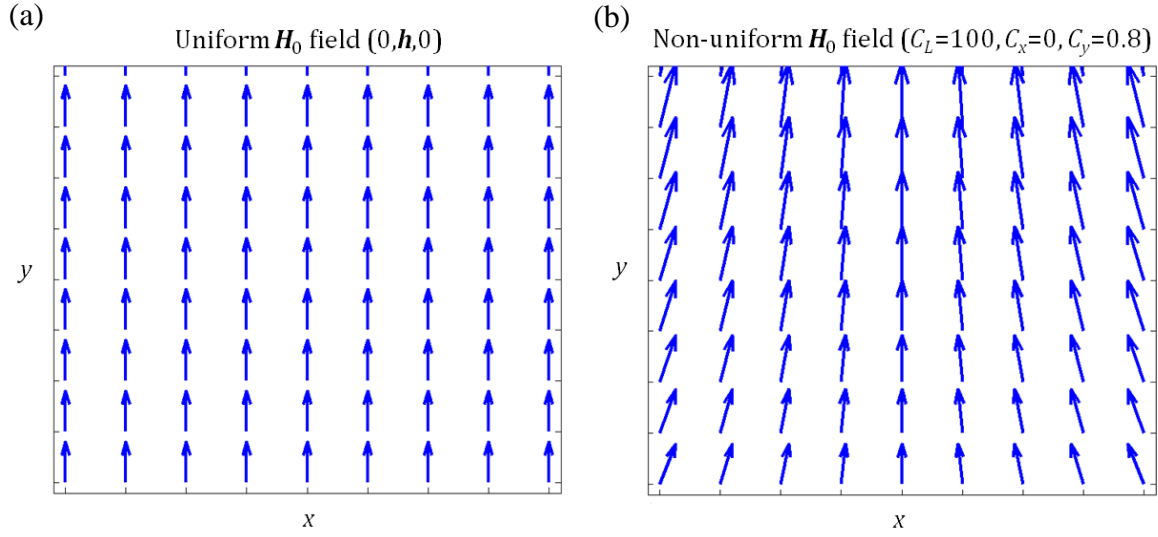
Figure 6. Two-dimensional vector field representations of the (a) uniform and (b) nonuniform applied magnetic fields H_0 for this study.

4.5   Shear Flow Profile

For the case of simple shear flow, the following boundary conditions apply with reference to the geometry of the model:

$$y = -\frac{L}{2}, v_x = -V$$

$$y = \frac{L}{2}, v_x = V$$

wherein L is the length of the simulation box and V is a constant velocity. Solving equation [3.5] under the above boundary conditions yields an expression for the specific flow field of an ambient fluid:

$$v_x = \frac{2V}{L}y \qquad\qquad [4.9]$$

A two-dimensional representation of this equation is exhibited in Figure 7c. The flow field is governed by the Stokes equations. Analytical solutions of the flow field for Stokes flow have been calculated (Bird *et al.*, 2002).

4.6   **Application of the Constraint Method**

As long as a time-step Δt elapses, the particles are allowed to interact unconstrained with each other, respond to the resultant hydrodynamics, undergo Brownian motion, drift with the shear flow, and acquiesce to the applied magnetic field. Then the constraint process for the Maxwell's equations is activated following the interactions between particles during Δt. For the constraint method to fulfill the Gauss's Law constraint $\sigma_{G,j}$ for $j = 1,2,\dots,d'_G$, the volume is split into $d'_G = 8$ equal cubes with dimensions L_c of $20a \times 20a \times 20a$, so as to represent local volumes of the system. Each surface of a local cube is populated with 16 nodes in a 4-by-4 array with a spacing of $5a$. This is roughly visualized in Figure 7a. At each node, the weighting function is employed, as described in equation [3.73], to calculate the **M** field in equation [3.74] while the **H** field in equation [3.75] is processed via equation [3.77] alongside an appropriate $\boldsymbol{H}_0$. A surface integral is then calculated for each of the eight local volumes, which allows the Gauss's Law to be satisfied over eight local constraints. Fortunately, the periodic boundaries in the *x*- and *z*-directions reduce the total number of surface integral calculations required for the *xy*- and *yz*-faces at $z = \pm 20a$ and $x = \pm 20a$, respectively. As for the magnetostatic Ampère's Law, the constraint $\sigma_{A,j}$ for $j = 1,2,\dots,d'_A$ must be met at the boundaries to ensure that the tangential component of magnetic field is continuous. At the walls boundaries, the borders surrounding the surfaces are segmented into evenly-distanced nodes. In this case, each of the $d'_A = 2$ borders contains 32 nodes, eight per side with a spacing of $5a$. This constraint design is crudely illustrated in Figure 7b, with the normal

direction to the surface dictating the positive direction of the arrows circumnavigating the boundary. Equation [3.75] is employed to calculate **H** at each node. Afterwards, a line integral is evaluated for each of the two borders, which allows the Ampère's Law to be satisfied over two local constraints. In conclusion, the system employs no more than eight local volume constraints and two boundary constraints in consideration of computational limits. Thus, the constraints are developed into viable expressions that are computationally efficient for the present study.

(a)

(b)   (c)
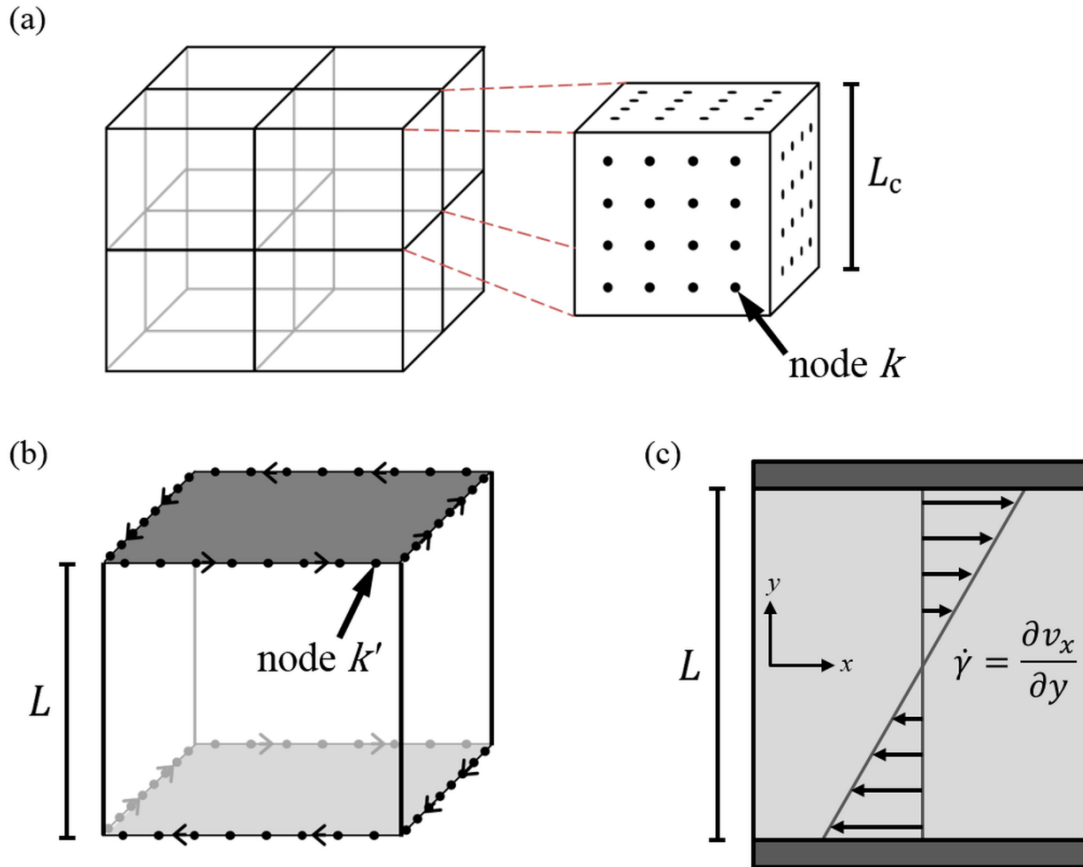
Figure 7. System representation of the (a) local constraint volumes for the Gauss's Law with nodes k and (b) local constraint boundary surfaces for the Ampère's Law with nodes k'. (c) A rough illustration of the Cartesian xy-view of planar shear flow with shear rate $\dot{\gamma}$. Reprinted from Dubina and Wedgewood (2016), with the permission of AIP Publishing.

At each time-step, all $d'(= d'_G + d'_A) = 10$ holonomic constraints must simultaneously comply within a specified limit. When the constraint method is activated, the Lagrange multipliers γ_j, as seen in equation [3.81], are found by means of an iterative procedure. In terms of solving for the constraints σ_j, equation [3.86] is used for Gauss's Law $\sigma_{G,j}$ while equation [3.89] manages Ampère's Law $\sigma_{A,j}$. The modified metric matrix $\tilde{G}_{jl}$ demonstrates the dependency of the constraints on each other and is essential for each iteration. This is because every constraint relies on the system's configuration. The derivatives of equations [3.86] and [3.89], those of which are provided in Appendix B, are required to solve for $\tilde{G}_{jl}$ and process equation [3.79]. Once the Lagrange multipliers have converged to a reasonable value, the constraint force $\boldsymbol{F}_\alpha^{\text{CON}}$ and torque $\boldsymbol{T}_\alpha^{\text{CON}}$ are determined, which are then used to compute the position $\boldsymbol{r}_\alpha^{\text{CON}}$ and dipolar vector $\boldsymbol{\varphi}_\alpha^{\text{CON}}$ of particle α within the ferrofluid system. It is then that a revised configuration is visualized and the simulation advances to the next time-step.

4.7 **System Parameters**

An assemblage of $N = 512$ unit dipoles is randomly arranged within the cubic volume characterized by dimensions L of $40a \times 40a \times 40a$. Since the volume and total particle number are dependent on other ferrofluid attributes, they are useful for calculating the ferroparticle diameter, volume fraction, or particle density, as long as these properties are within sensible ranges that are representative of conventional ferrofluid solutions. For simplicity, the center of the system coincides with the origin of a three-dimensional Cartesian coordinate system and has lower and upper ranges of $-20a$ and $+20a$, respectively. The size of this system depicts a relatively small prototype of a ferroparticle dispersion.

The model should ultimately provide extensive predictions of the impacts of particle kinetics, aggregation, shapes, and properties on valuable aspects of FHD. By controlling the values of the dimensionless numbers introduced from equations [3.67] to [3.69], specific effects can be monitored. However, before dictating particle-particle magnetic interactions, particle-field response, aggregation behavior, Brownian motion influence, and shear flow impact, dimensionless numbers must be regulated by virtue of the ratios introduced in equation [3.70]. When the simulation is compiled with $\lambda = (3, 5, 7, 9)$, the ratios of R_v/R_m and $1/(R_m Pe)$ result in $(158.67, 95.200, 68.002, 52.891)$ and $(0.244, 0.146, 0.105, 0.0814)$, respectively. The ratio of R_h/R_m will be maintained around 3.3, a magnitude that was found to support the assumption of a strong magnetic field. The dimensionless property λ primarily determines the degree to which the magnetostatic particle-particle and particle-field interactions overwhelm the Brownian motion effects. Most importantly, for $\lambda = 9$, magnetostatic interactions dominate nearly all Brownian motion effects, thus enabling chain formation amongst particles and along the y-direction. Hence, this property will be analyzed over the others in the present study. Under this constant, $\xi = 54.07$ for $R_h/R_m = 3.3$ and the steric attributes of d_δ and λ_v are held constant at 0.3 and 150, respectively. The parameters are outlined in Table III below.

TABLE III

PARAMETER SETS FOR FERROPARTICLE SIMULATIONS[a]

λ	R_m	$(R_\mathrm{m}\mathrm{Pe})^{-1}$	$R_\mathrm{v}/R_\mathrm{m}$	Δt^* $(\times 10^5)$	ξ
3	50	0.2441	158.672	3.687	18.025
5	50	0.1465	95.2033	6.145	30.041
7	50	0.1046	68.0024	8.603	42.057
9	1	0.08137	52.8907	10.00	54.074
9	10	0.08137	52.8907	10.00	54.074
9	25	0.08137	52.8907	10.00	54.074
9	50	0.08137	52.8907	10.00	54.074
9	100	0.08137	52.8907	5.530	54.074

[a] Under constants $d_\delta = 0.3$, $\lambda_\mathrm{v} = 150$, and $R_\mathrm{h}/R_\mathrm{m} = 3.3$.

In regards to the cutoff distances in Table II, they were assigned reasonable values that boost the computation speed. The cutoff radius for particle-particle interactions r_coff is set at $16a$. For the cutoff distance concerning hydrodynamic interactions $r_\mathrm{coff}^{(\mathrm{hydro})}$, it is set at $3.8a$, which prevents triple-particle interplay. The cutoff radius for the constraint method h is simply set to that of the cutoff distance for particle-particle interactions. In doing so, the entirety of the system volume is incorporated when calculating the constraints.

5. RESULTS

5.1 <u>**Constraint Trends and Comparison**</u>

While the simulation advanced by a time-step, the constraints were continually satisfied over all runtimes. The particles were impacted by an applied magnetic field, Brownian motions, interparticle interactions, and shear flow effects before the constraints were initiated. Then, to ensure that the Maxwell's equations are continuously met, the constraint equations in [3.86] and [3.89] were tracked for models with and without an activated constraint method. The two simulations were run under a uniform magnetic field with parameters of $\lambda = 9$ and $R_\mathrm{m} = 50$. They were also simultaneously executed over 300,000 nondimensional time-steps N_t $(= t/\Delta t)$, which was an ample amount of time for an initially randomized ferroparticle system to reach a steady-state. For $d'_G = 8$ constraints to satisfy Gauss's Law, Figure 8a illustrates the trends between a model whose magnetic field is divergence-free to one that is not. The simulation with an activated constraint procedure has abided by Gauss's Law and consequently, produces a trend line at zero while the other fluctuates uncontrollably. The latter situation would be acceptable for macroscopic simulations. However, for time-steps as small as the ones used in this Brownian dynamics study, it is unreliable since the fields must be solenoidal at each time-step. A similar situation applies for the satisfaction of the magnetostatic Ampère's Law. For $d'_A = 2$ constraints representing Ampère's Law, Figure 8b compares results with a magnetic field that is curl-free compared to another that is not. It is apparent that the fluctuations for Ampère's Law are less wild than those of Gauss's Law, which may be due to the range of the boundary surfaces as opposed to the reach of the local constraint volumes. More importantly, the trends demonstrate a curl-free magnetic field throughout the volume. These observations were consistent across all simulations under the parameter sets of Table III and nonuniform fields. Thus, the constraint algorithm has provided a

means to comply with the governing Maxwell's equations while the system advances. Additionally, the trends lacking the constraint method are comparable to Brownian dynamics results by other researchers.
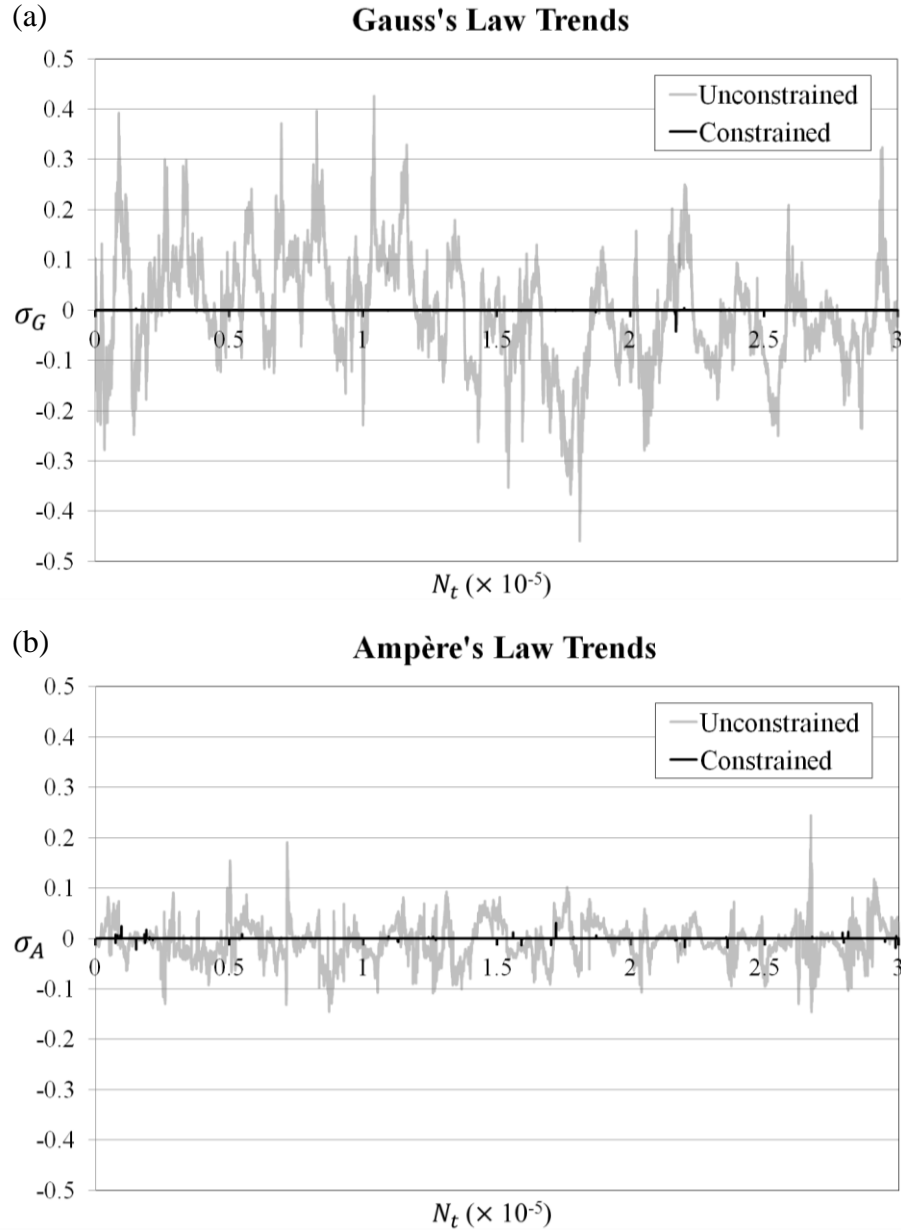
Figure 8. Trend of (a) Gauss's Law and (b) the magnetostatic Ampère's Law ($\lambda = 9$, $R_\mathrm{m} = 50$). Adapted from Dubina and Wedgewood (2016), with the permission of AIP Publishing.

5.2   **Uniform Magnetic Fields**

5.2.1   **Steady-state Particle Distributions**

A steady-state representation of the system provides a means of observing the general behavior of ferrofluids. A three-dimensional illustration of the particles distributed throughout the volume at any given time can roughly illustrate chain formation and particle diffusion. To inspect the aggregates further, distinct rectangular prisms of the volume (henceforth identified as "slices") scrutinize particles in a localized volume. To define an *xy*-slice, for example, only the particles that reside between two square *xy*-planes are considered. In this study, *xy*-, *yz*-, and *xz*-slices examined particles within Cartesian spaces enclosed between *xy*-, *yz*-, and *xz*-planes, respectively, each of dimensions $40a \times 40a$. Specifically, *xy*-slices were placed at $z = -2.5a$ and $z = +2.5a$, *yz*-slices situated at $x = -2.5a$ and $x = +2.5a$, and *xz*-slices sited at $y = -2.5a$ and $y = +2.5a$. The coordinates were chosen in order to observe particle activity around the center of the system volume. Moreover, while the *xy*- and *yz*-slices emphasize the chaining that forms along the *y*-direction, the *xz*-slice inspects any dipoles shifting away from the magnetic field bearing. Thus, with the spatial particle distributions and their slices, one can scrutinize the aggregation behavior of ferrofluid particles as the model progresses. In addition, note that slices may not display complete chains due to adjacent particles that are located just beyond the boundaries of the slice. Also, the position vector $\boldsymbol{r}$ and coordinates are divided by a to generate their respective dimensionless forms. As a reminder, the superscript '*' represents the dimensionless form of properties.

After running the Brownian dynamics simulations for $N_t = 300{,}000$ time-steps, spatial distributions and planar slices characterize the resultant ferrofluid particle activity. Under values of $\lambda = 9$ and $R_{\mathrm{m}} = 50$, and with an activated constraint algorithm, strong magnetostatic attractions

are known to invalidate the Brownian dynamic effects. For the case of a shear fluid flow, Figure 9a demonstrates a particle distribution that has reached steady-state. Though the dipoles still remain visibly aligned in the magnetic field direction and are hardly skewed by the viscous shear torques, the magnetically-attracted particle chains reveal a slight slant due to the shear flow profile. When viewing any planar slice of Figure 9a, chains are better perceived. The *xy*- and *yz*-slices portrayed in Figures 9b and 9c, respectively, verify the general observations previously stated of the entire particle distribution. The *xy*-slice in Figure 9b accentuates the aforementioned slanting effect of the viscous shear forces on the particle chains. In Figure 9c, the *yz*-slice does not depict a diagonal lean in the aggregates because the shear flow moves in the *x*-direction and relies solely on the *y*-position. And finally, the *xz*-slice in Figure 9d confirms a prevailing magnetic field influence since hardly any dipoles shifted away from the *y*-direction. Thus, the internal structures of the chains exhibit typical ferrofluid agglomeration behavior in the presence of shear-flowing (or stagnant) ambient fluid.

Figure 9. (a) Spatial particle distribution under a uniform magnetic field ($\lambda = 9$, $R_\mathrm{m} = 50$). The corresponding (b) *xy*-, (c) *yz*-, and (d) *xz*-slices provide comprehensive views of the strong chaining behavior. Strong particle aggregation is observed under these parameters. Reproduced from Dubina and Wedgewood (2016), with the permission of AIP Publishing.

Under a decreased R_m value, the quotient of magnetostatic effects to viscous shear forces is reduced while maintaining the previously-stated ratios of dimensionless numbers. This was accomplished by setting the R_m dimensionless number to 1, which corresponds to relatively weak magnetostatic interactions. A proportionately lower R_h follows to uphold the constant R_h/R_m ratio. The particular value for R_m preserves the dominance of magnetic particle-particle attraction over Brownian motion. However, with diminished R_m, the Péclet number becomes 12.29 and the viscous shear forces possess a much greater impact on chain evolution. Thus, Figure 10a exhibits a nearly complete deficiency of aggregated particle chains present after $N_t = 300{,}000$ time-steps, compared to Figure 9a. The magnetic interplay between particles was not capable enough to generate consistent agglomeration, even when the applied magnetic field was substantial enough to keep the particle dipoles somewhat directed in the primary y-direction. Additionally, the dipoles are leaning noticeably away from the magnetic field direction due to the shear flow forces. The slices in Figure 10 support these notions. There is considerable inclining of the dipoles in the shear flow direction in Figure 10b but none observed by the yz-slice in Figure 10c. Since the external magnetic field was still stronger than the Brownian rotation, the dipoles in Figure 10d are not directed in the z-direction. Also, though most of the dipoles are obstructed by the particle size in the xz-slice, one can notice slight traces of them pointed in the x-direction due to viscous shear.
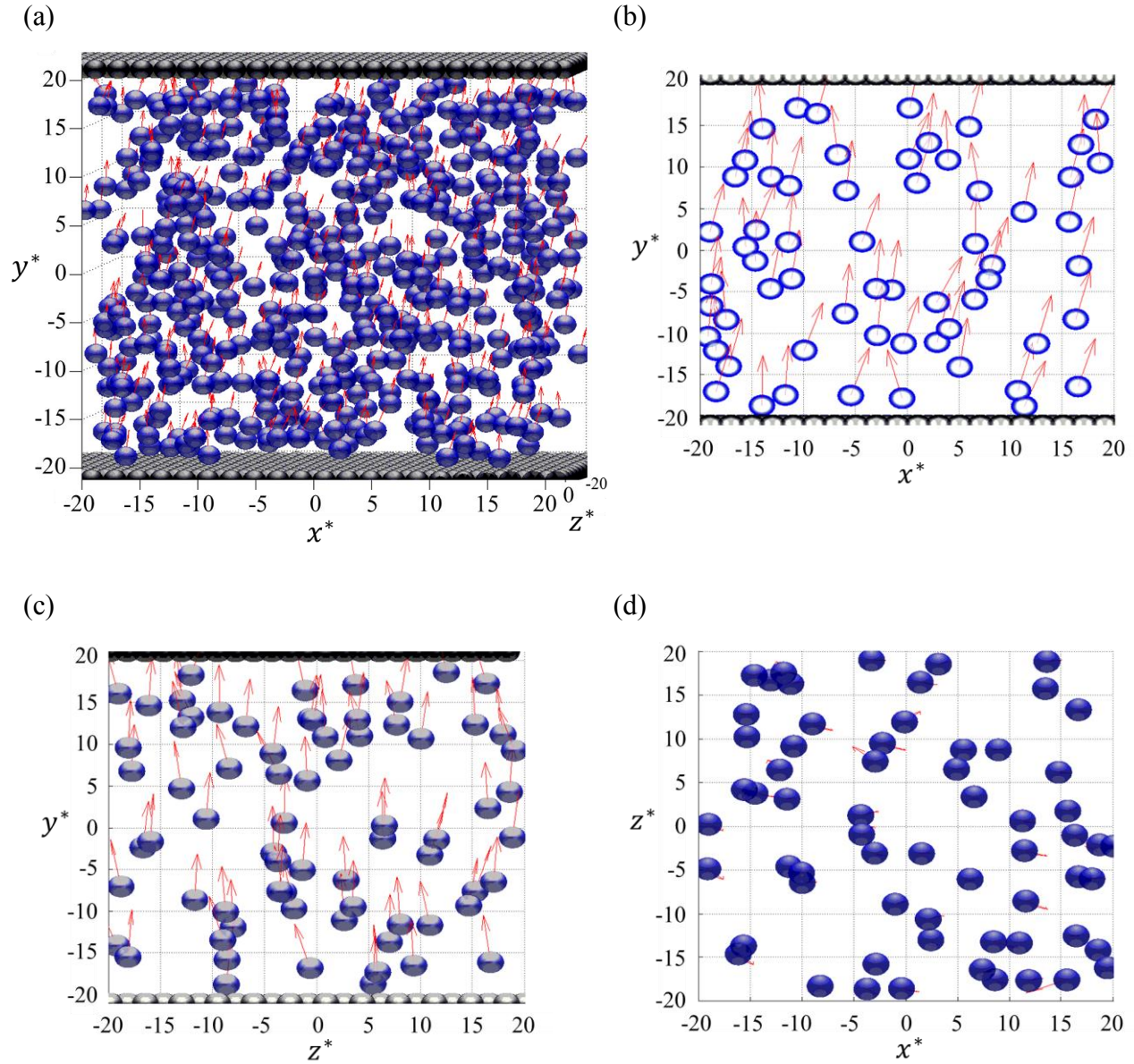
Figure 10. (a) Spatial particle distribution under a uniform magnetic field ($\lambda = 9$, $R_\mathrm{m} = 1$). The corresponding (b) xy-, (c) yz-, and (d) xz-slices provide comprehensive views of the strong shearing effects and lack of agglomeration. Weak particle aggregation but strong shearing effects are observed under these parameters. Reproduced from Dubina and Wedgewood (2016), with the permission of AIP Publishing.

Under a substantially large R_{m} value, the impact of the magnetic particle-particle and applied field effects increases. In this case, R_{m} was increased to 100, imposing a rise in the ratio of magnetostatic effects to viscous shear forces while preserving the aforementioned ratios of dimensionless numbers. Subsequently, an elevated R_{h} ensues to maintain the fixed $R_{\mathrm{h}}/R_{\mathrm{m}}$ ratio. Consequently, chaining activity was expected to flourish under these parameters. As exemplified by Figure 11a, the chains appear denser. The particles were also not affected by the viscous shear forces, primarily due to the low Péclet value and dominant magnetic particle-field interactions. Observing the *xy*-slice in Figure 11b confirms that the chains were not affected by the shear flow and do not tilt like the aggregates in Figure 9b. And because the ambient fluid had hardly any bearing on the particles, the *yz*-slice in Figure 11c exhibits a similar trend to the *xy*-slice. In terms of the *xz*-slice in Figure 11d, it exhibits no unusual behavior and affirms the prior observations. Thus, the applied magnetic field was effective enough to overcome the viscous shear forces and induced long particle chain aggregation solely along the *y*-direction.

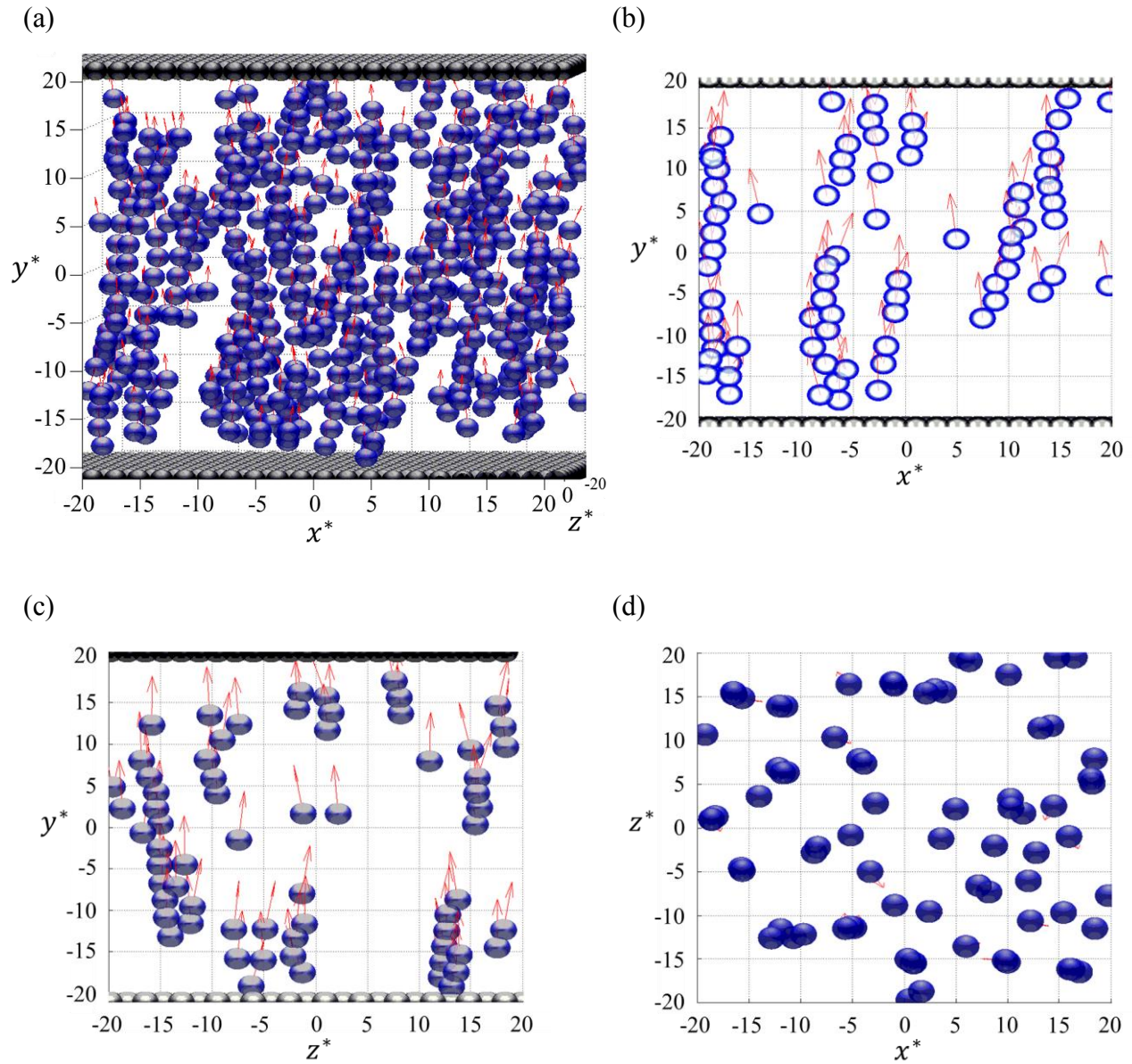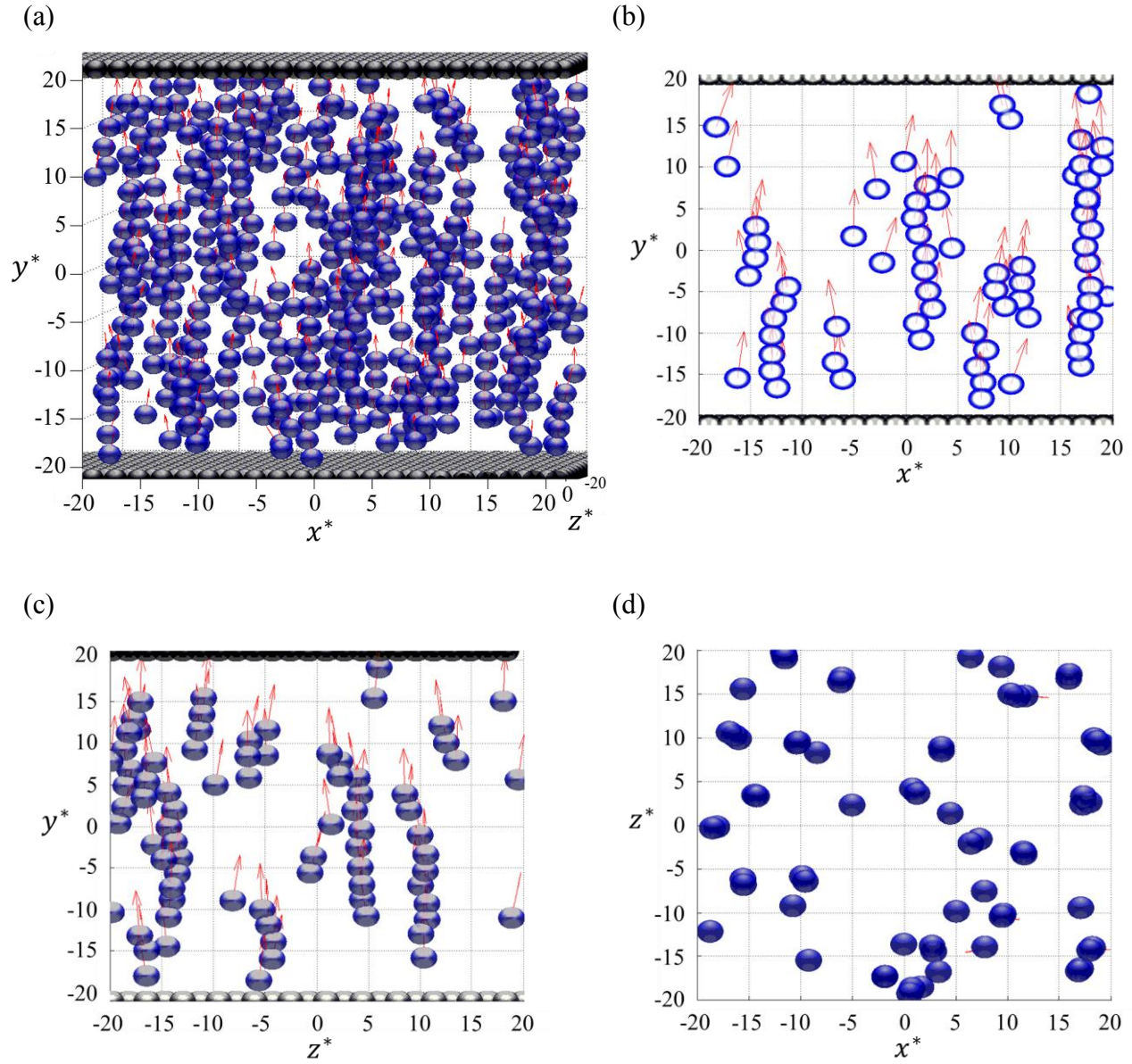Figure 11. (a) Spatial particle distribution under a uniform magnetic field ($\lambda = 9$, $R_{\mathrm{m}} = 100$). The corresponding (b) *xy*-, (c) *yz*-, and (d) *xz*-slices provide comprehensive views of the powerful chaining behavior. Significantly strong particle aggregation is observed under these parameters. Reproduced from Dubina and Wedgewood (2016), with the permission of AIP Publishing.

Alternatively, a value of $\lambda = 3$ indicates prevailing Brownian motion. This will alter the dimensionless ratios, according to the equations in [3.70]. The thermal energy disbands any particle pairs, despite the strong magnetic attractions, and overpowers the viscous shear forces. In Figure 12a, after $N_t = 300,000$ time-steps, the particles appear sporadically dispersed. However, since the uniform external magnetic field primarily affected the torque on the particles, and when the R_h value is high enough, the rotational Brownian torque was not enough to overcome it. This observation is further verified when the model is supervised under a nonuniform magnetic field or low R_h constant. Additionally, the shear torque was not substantial enough to offset the dipoles completely, as embodied by a low Péclet number. The planar slices, again, allow a closer look at the internal structure. Both Figures 12b and 12c reveal minimal aggregation with dipoles steered in the direction of the field. Figure 12d suggests some deviation of the dipole away from the field direction when compared to the other parameter sets, though not considerable when claiming Brownian rotation responsible.
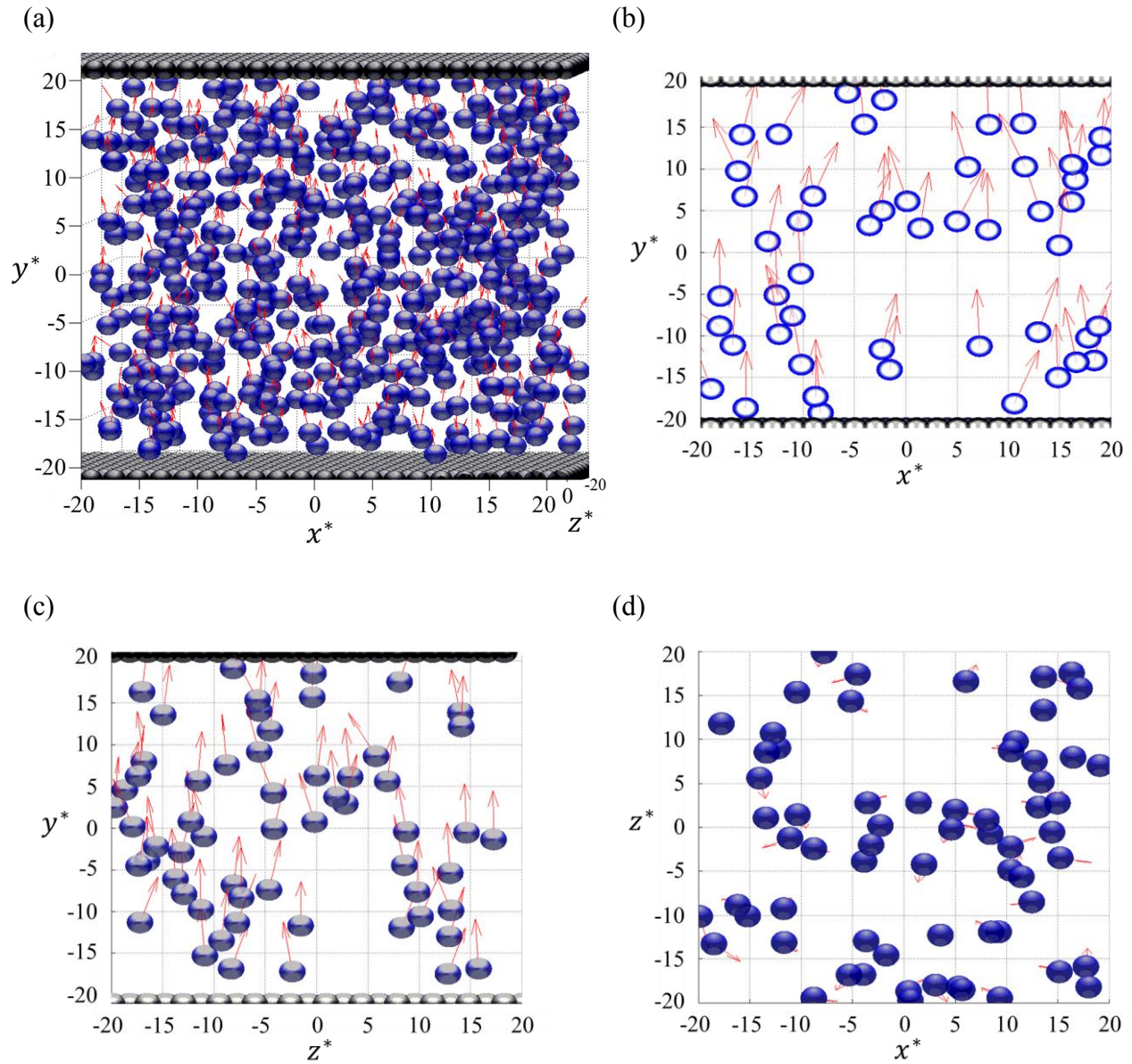
Figure 12. (a) Spatial particle distribution under a uniform magnetic field ($\lambda = 3$, $R_\mathrm{m} = 50$). The corresponding (b) xy-, (c) yz-, and (d) xz-slices provide comprehensive views of the prevalent Brownian effects and inadequate chaining. Dominating Brownian effects and weak particle aggregation are observed under these parameters. Reproduced from Dubina and Wedgewood (2016), with the permission of AIP Publishing.

Based on the four parameter groups that were tested above and because of Brownian motion, the aggregates can be said to have loose internal structures, even when the particles form long chains. The Brownian motion, though trivial compared to the magnetostatic effects, is not entirely absent in the simulations. These thermal fluctuations tend to moderately disturb the orientations of the magnetic moments in the presence of an externally-applied field, which may occasionally lead to crooked chaining or interparticle separation. However, this effect is not a notable concern because it does not occur enough to separate chains unless the parameters designate otherwise.

5.2.2 **Pair Correlations**

Although the spatial distribution of the volume appears to demonstrate the aggregation behavior of particles under the influence of an external magnetic field, one must closely analyze the structure of the chains. A pair correlation function (PCF) provides a method of quantifying the chain formation in the models. Peaks on a PCF graph characterize the probability of the number of particles adjacent to a particle α and the direction they align relative to the applied magnetic field. The PCF functions are not dependent on the dipole direction. The algorithm involves measuring the angle θ and distance r from particle α to others. The angle θ designates the deviation from the magnetic field and is measured from the center-to-center vector of a particle pair to the primary magnetic field direction $\boldsymbol{H}_0$. The distance r is taken from the center of particle α to any adjoining particles. A demonstration of this design is rendered in Figure 13. The values are added up and plotted in a pair correlation graph. The peaks equate to the probability of chain lengths at angles θ. A peak does not explicitly signify the extent of chain size but rather expresses the capacity of other particles within proximity of each ferroparticle.
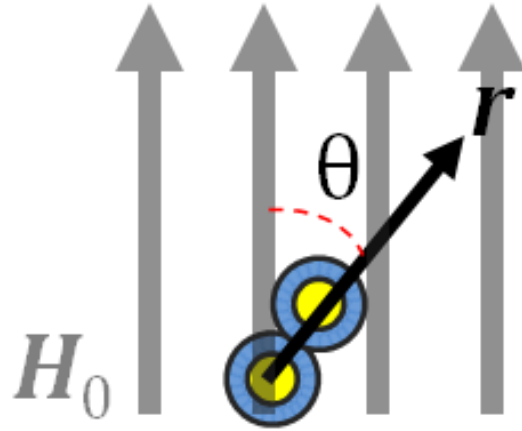
Figure 13. Visualization of the explanation for
the pair correlation scheme.

The PCF graph for a run under values of $\lambda = 9$ and $R_\mathrm{m} = 50$ demonstrates substantial

peaks along $\theta = 5 - 15°$ and verifies the chaining behavior due to strong magnetic interactions

between particles and vigorous agglomeration tendencies. A majority of the peaks in Figure 14

emerge along $\theta \approx 10°$ because of the strong influence due to the external magnetic field and

minimal deviation away from it. The most notable quantities range from $r = 2$ to $r = 6$ since the

PCF detected long chains of ferrofluid particles. The highest peaks at $r = 2$ demonstrate that most

of the particles paired well with each other, meaning that the pairing was dominant between

twosomes. Peaks around $r = 3$ and $r = 4$ suggest long particle chains along the direction of the

field, observed in Figure 9a. And although most of the peaks materialize along $\theta \approx 10°$, some

appear at greater angles due to the viscous shear. Almost all of the particle pairs that were perturbed

by the shear flow measure within $30°$ from the field direction. For those that were angled beyond

that were found to be in close proximity to each other rather than coupled by magnetic particle-particle attraction. Therefore, residual quantities may occur beyond 30°.
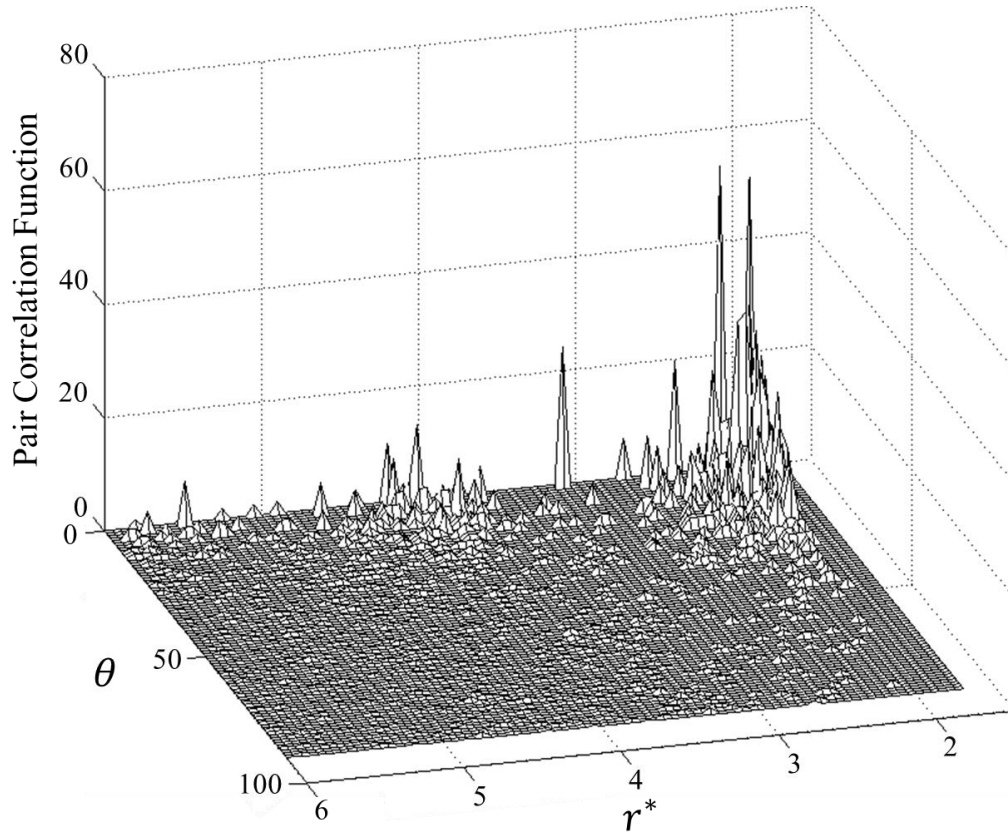
Figure 14. Graph of the pair correlation function ($\lambda = 9$, $R_\mathrm{m} = 50$). Large pair correlation functions under these parameters indicate a notable extent of particle chaining. Reprinted from Dubina and Wedgewood (2016), with the permission of AIP Publishing.

In regards to a decreased R_m value of 1, the resultant PCF plot in Figure 15 exhibits much lower peaks when compared to Figure 14 above. This is due to the viscous shear forces that dispersed any particles attempting to form chains. As mentioned before, under these parameters, the effects due to shear flow considerably outweighed those from magnetostatic attraction. The peaks previously detected at $r = 2$ are hardly noticeable now as a result of significant viscous shearing. Peaks also deviate away from $\theta \approx 10°$ due to existing chains that separated because of the shear flow profile. Thus, the PCF graph for the simulation is practically flat, which reflects the analysis stated of Figure 10a.
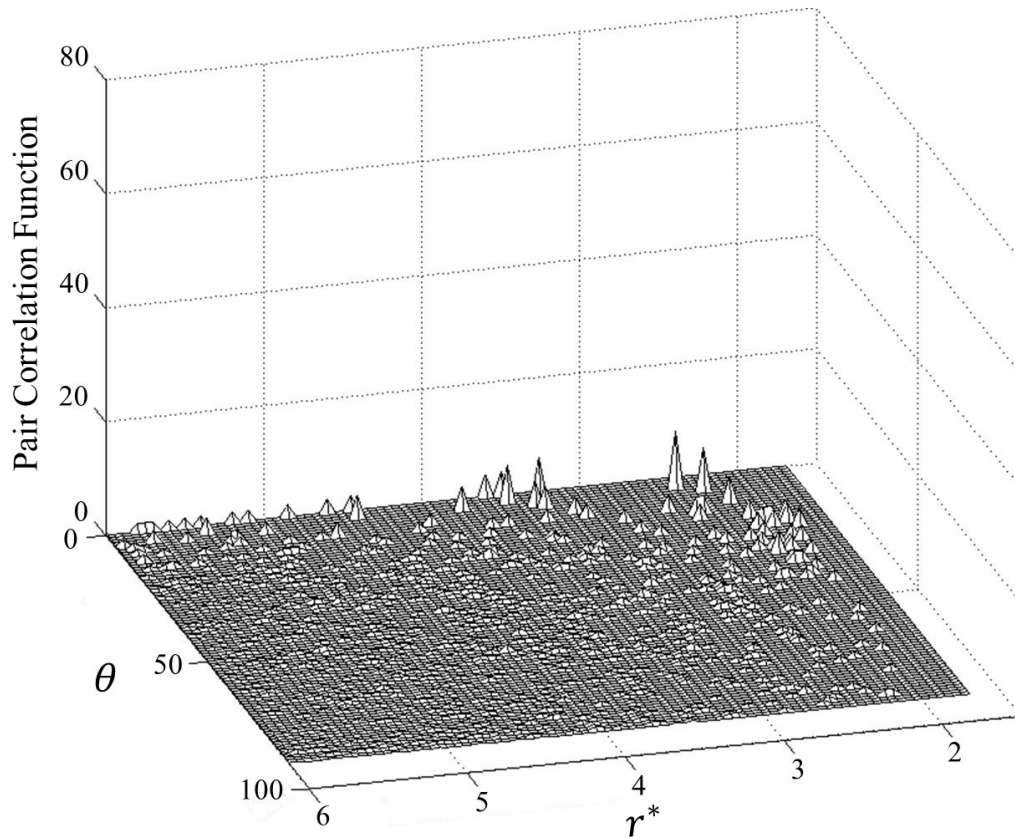
Figure 15. Graph of the pair correlation function ($\lambda = 9$, $R_m = 1$). Sparse traces of pair correlation quantities under this parameter set implies effective shearing that inhibits magnetic particle interactions. Reprinted from Dubina and Wedgewood (2016), with the permission of AIP Publishing.

For the run with $R_m = 100$, the peaks in Figure 16 are much higher than those of Figure 14. This emphasizes the high R_h constant (and by virtue, a high R_m number) that enabled a stronger external magnetic field which overshadowed viscous shear and Brownian motion. Consequently, the likeliness for particle pairing increased. And because the shear flow had less of an impact under this parameter set, the aggregates were considerably less angled. In this event, the peaks appear around $\theta = 0 - 10°$, less than the ones in Figure 14.
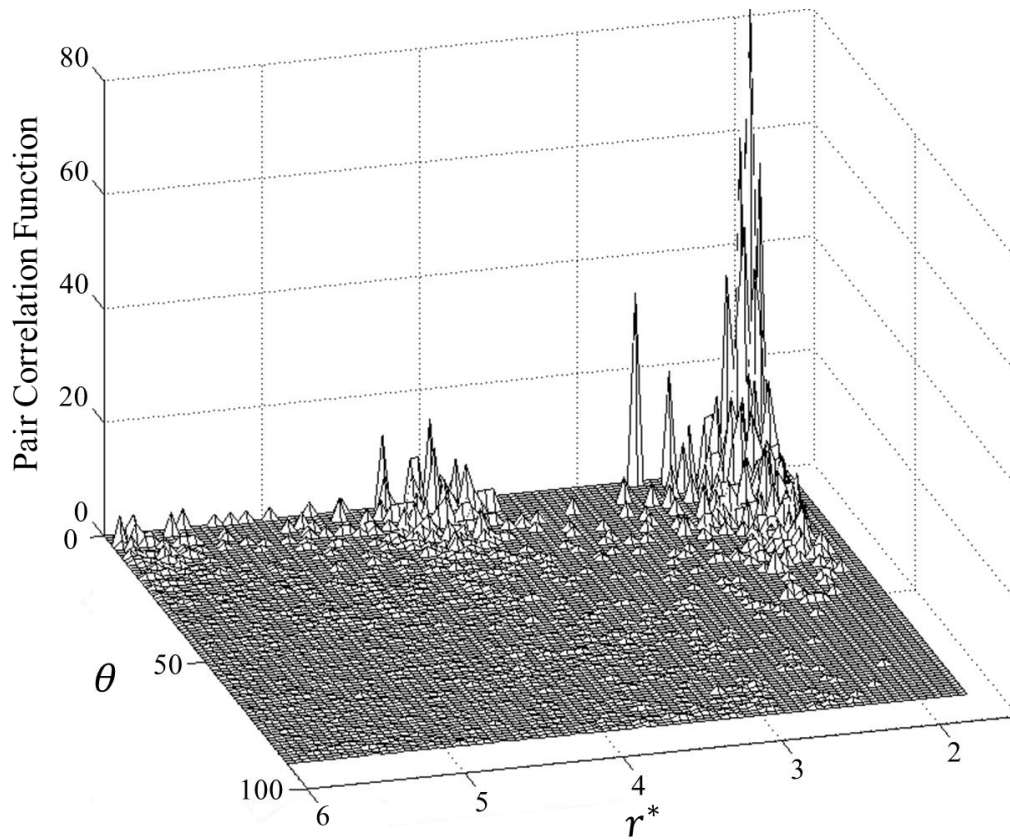
Figure 16. Graph of the pair correlation function ($\lambda = 9$, $R_m = 100$). High pair correlation peaks under these parameters designate exceptional levels of particle aggregation. Reprinted from Dubina and Wedgewood (2016), with the permission of AIP Publishing.

In the case of dominant Brownian motion simulated by a low value of λ, one would expect the PCF to generate no visible peaks. The thermal motion hindered any potential agglomeration and thus, the PCF should be a flat plane of low probability. Figure 17 characterizes the PCF for a run under $\lambda = 3$. As indicated, the deficiency of peaks implies that chaining was not present in the system volume at equilibrium. The results are similar to the PCF presented in Figure 15. And, analogous to the results of $R_{\mathrm{m}} = 1$, the most visible remnants of peaks seen in Figure 17 are predominantly along $\theta = 0$ since the applied magnetic field was not entirely obscured and allowed for some residual particle clusters to momentarily surface.
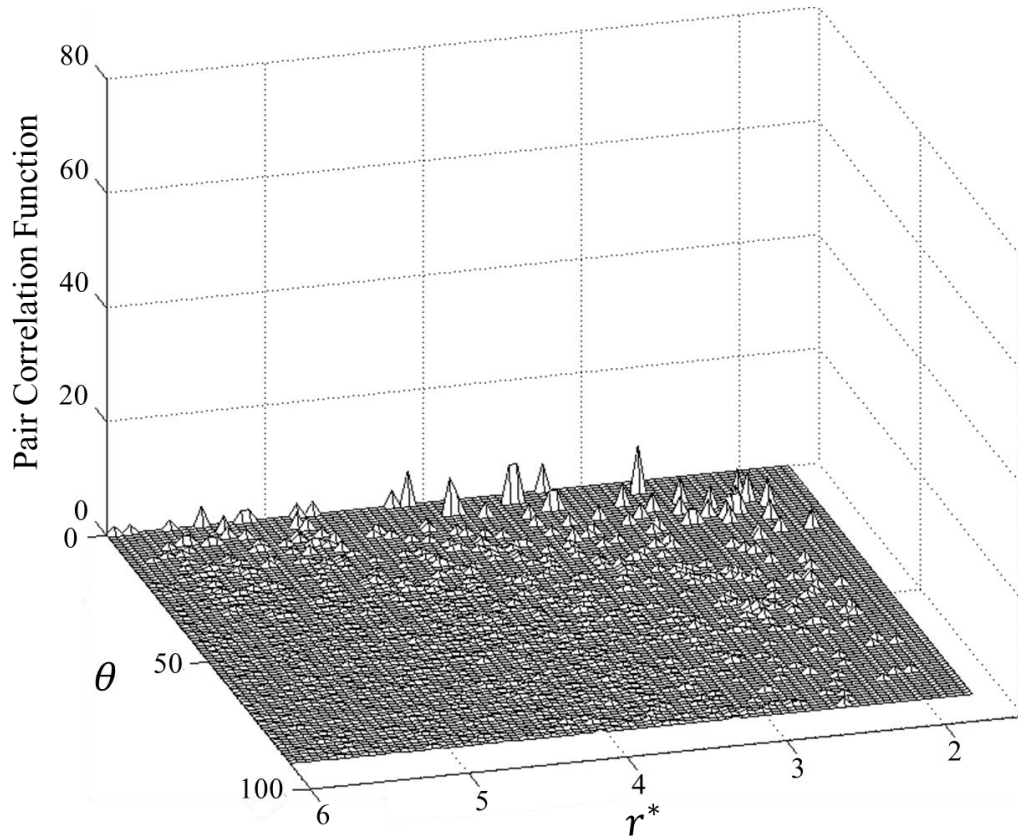
Figure 17. Graph of the pair correlation function ($\lambda = 3$, $R_{\mathrm{m}} = 50$). A lack of pair correlation measurements with these parameters suggests that the Brownian forces overpowered particle chain development. Reprinted from Dubina and Wedgewood (2016), with the permission of AIP Publishing.

With these PCF graphs, the descriptions inferred of the chaining in the particle distributions of the previous section are verified.

5.2.3 **Magnetoviscous Effects**

From the models that have replicated exceptional chaining conduct, one can observe how the particle chains have affected the local ferrofluid behavior. Since there are distinct chains that conform to the applied magnetic field (and viscous shear forces), the dimensionless viscosity, introduced in equation [3.78], is employed to evaluate the effects of the aggregates on the non-Newtonian fluid property. The dimensionless viscosity contribution was time-averaged up to and at steady-state for each parameter set and simulation run.

Several λ values are observed under a constant R_{m} to monitor the importance of magnetic particle-particle interactions on the magnetoviscosity of the suspension. These trends depict the spin viscosities of models both with and without activated constraints and are displayed in Figure 18. Error bars around the data points signify the standard deviation. In both constraint instances, when decreasing toward $\lambda = 3$, the measured viscosity differences approach zero and the variation in the time-averages are minimal, conveying familiar ferromagnetic behavior. The data comprised of triangular elements denote the magnetoviscous changes analyzed under unconstrained conditions. When the constraint procedure is incorporated, however, the $\langle \eta^{\mathrm{m}*} \rangle$ trend abated. Designated by square symbols, this decline demonstrates that the Maxwell's equations are not entirely satisfied, which verifies that the physics should be meticulously upheld (as verified in Figure 8). The comparison to systems lacking activated constraints indicates that the contribution to the spin viscosity is comparably lower than other studies suggest.
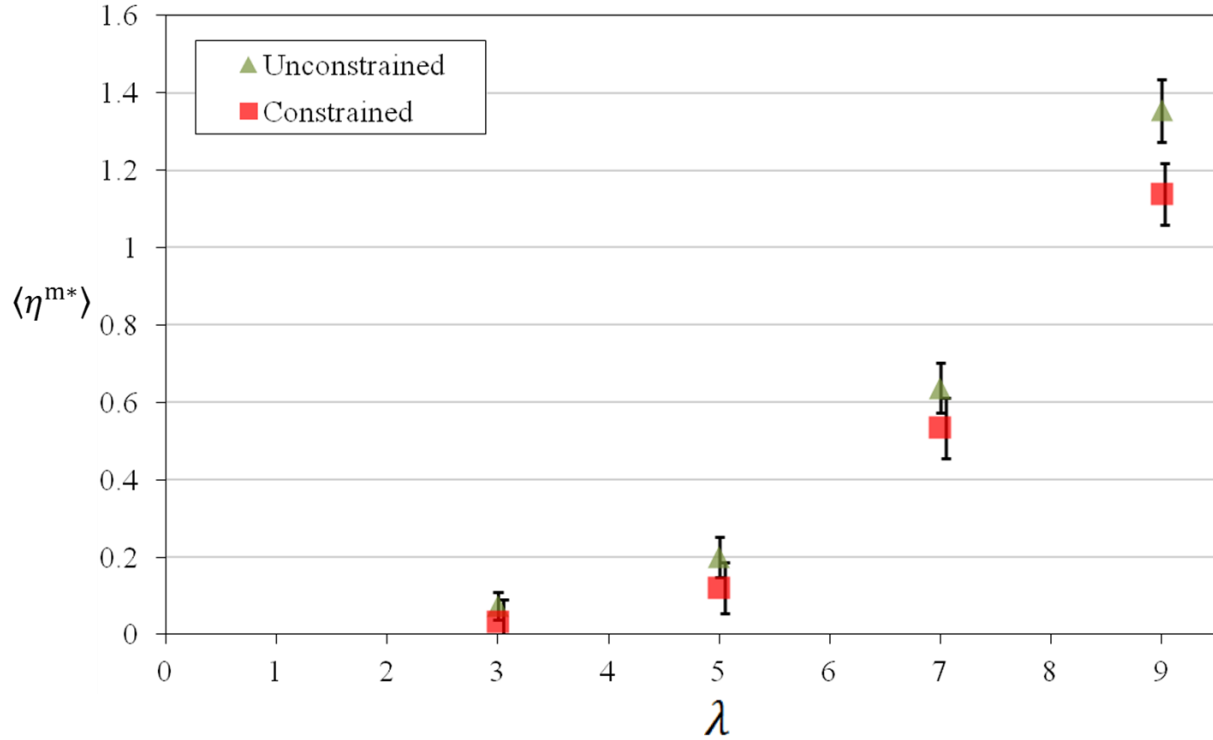
Figure 18. Spin viscosity dependence on magnetic particle-particle effects ($R_{\mathrm{m}} = 50$).

Increasing dimensionless number R_{m} under a constant λ varies the significance of the shearing and supplies an understanding of how the shear flow manipulates the non-Newtonian viscosity development. Figure 19 exhibits three separate trends. Similar to the information in Figure 18, when decreasing toward $R_{\mathrm{m}} = 1$, the measured viscosities converge toward a value of zero and discrepancies in the time-averages become trivial. The first set of points marked by triangles possesses a deactivated constraint procedure and is akin to existing simulated results (Satoh *et al.*, 1998). The square-shaped characters symbolize the second operation in which the study's constraint method was implemented. This outcome reiterates the interpretation expressed of Figure 18 when inferring that the Maxwell's equations need to be appropriately heeded. The

third trend (embodied by hollow circles and accompanied by a gray line in Figure 19) is representative of experiments involving a magnetic fluid rheometer designed to discern the magnetoviscosity contributions over scenarios of various shear rates and applied magnetic fields (Odenbach and Störk, 1998). Evidently, the constrained occurrences coincide quite well with the experimental data, corroborating the conclusions stated of the constraint algorithm. The results support the observations that, again, the magnetic component of the spin viscosity is not as extensive as previously realized and not all effects on the particle dipole are always integrated in particulate ferrofluid research.
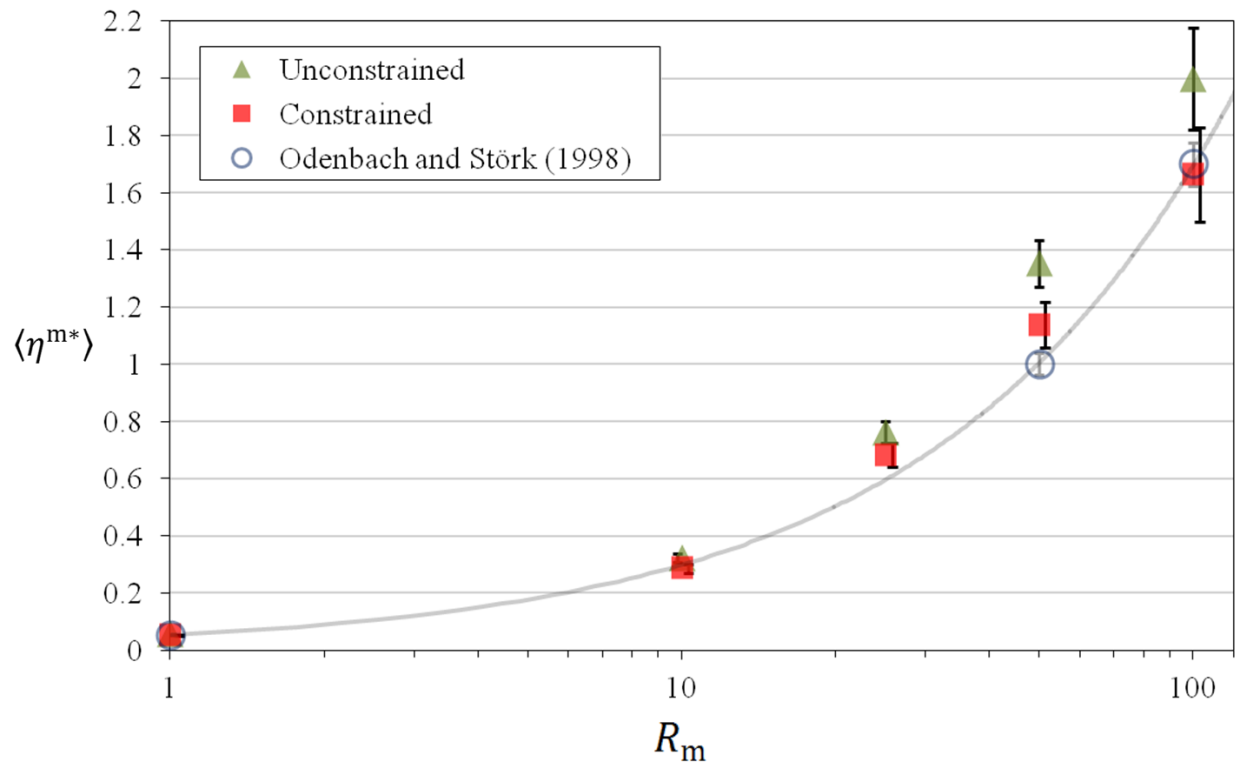
Figure 19. Effect of shear flow on spin viscosity ($\lambda = 9$). The gray line corresponds to the best-fitting trend line for the data from Odenbach and Störk (1998).

5.3   **Nonuniform Magnetic Fields**

5.3.1   **Steady-state Particle Distributions**

Three-dimensional steady-state representations of the particle distributions not only reveal aggregation behavior but can also epitomize the repercussions of MP. However, slices of localized volume are unnecessary for this section since the instantaneous snapshots will not contribute any pertinent information on the diffusion. Therefore, particle chaining will not be the central focus of this section although MP is assumed to be cooperative.

A constraint model that has reached steady-state for parameters of $\lambda = 3$ and $R_\mathrm{m} = 50$ is displayed in Figure 20. Although MP is visibly effective in transporting the particles towards the magnetic source at the top of the channel, it is still inadequate for achieving thorough magnetic separation. Even though the dipoles are pointed in the proper field directions (according to Figure 8) with no perceivable deviations, other effects are more forceful than particle-field interplay. Because of the high $R_\mathrm{v}/R_\mathrm{m}$ ratio at this distinct value of λ, Brownian motion and steric repulsion are identified as the causes. Therefore, MP is limited under these parameters.
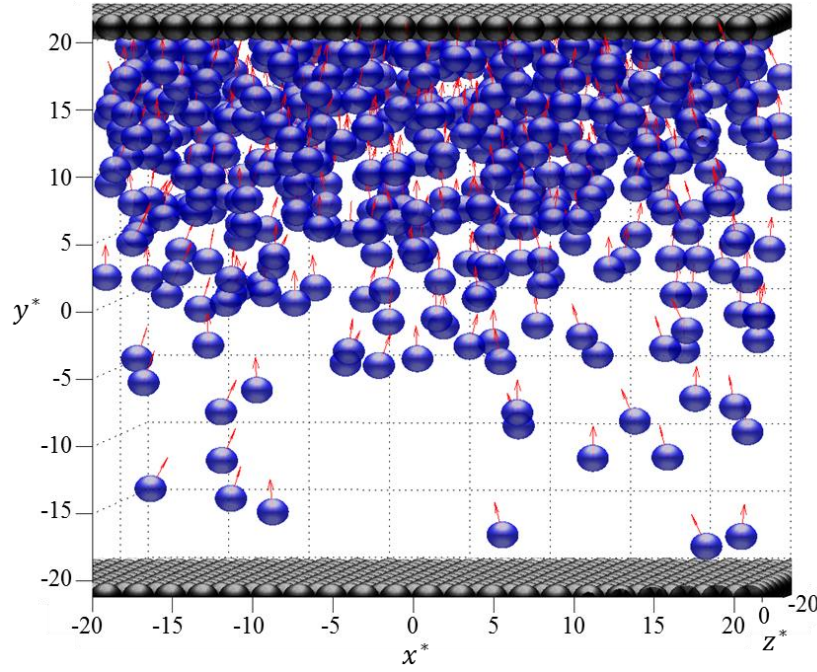
Figure 20. Spatial particle distribution under a magnetic field gradient ($\lambda = 3$, $R_\mathrm{m} = 50$). Brownian and steric effects prevent a considerable magnitude of particles from approaching the top of the channel.

When lowering the influence of Brownian motion by increasing the quantity of λ, Figure 21 demonstrates that the MP is more successful in magnetic separation. Compared to above, particles appear less sporadically-dispersed, dipole directions are more consistent with the magnetic field, and a greater density of magnetic constituents is occupying the upper half of the channel. Still, even at steady-state, there are noteworthy traces of uncaptured particles remaining around $y = 0$. Similar to the conditions under $\lambda = 3$, this model would not be sufficient for complete magnetic separation.
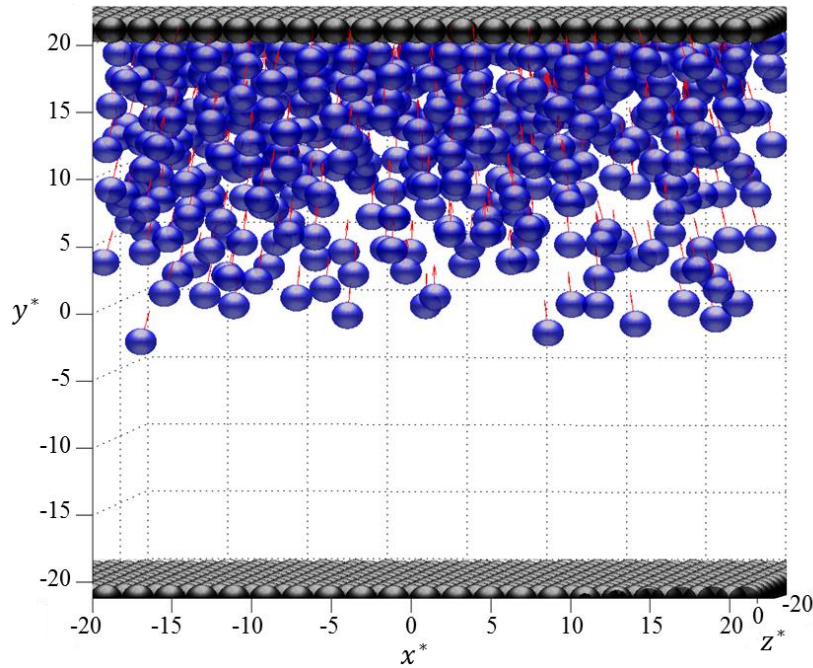
Figure 21. Spatial particle distribution under a magnetic field gradient ($\lambda = 5$, $R_{\mathrm{m}} = 50$). Many particles are captured but complete separation has not been achieved under these parameters.

Increasing the value of λ proves more prosperous, as one observes superior separation at the top of the channel in Figure 22. In this case, there is minimal particle presence around $y = 0$ and imperceptible evidence of strong Brownian fluctuation. Furthermore, at $\lambda = 9$, all other distributions (i.e. $R_\mathrm{m} = 1, 10, 25, 100$ in Table III) were discovered to be identical to Figure 22 at steady-state, so it can be referred to in those instances. This was understandable since the extent of steric repulsion and Brownian motion at $\lambda = 9$ were minimized, as perceived.
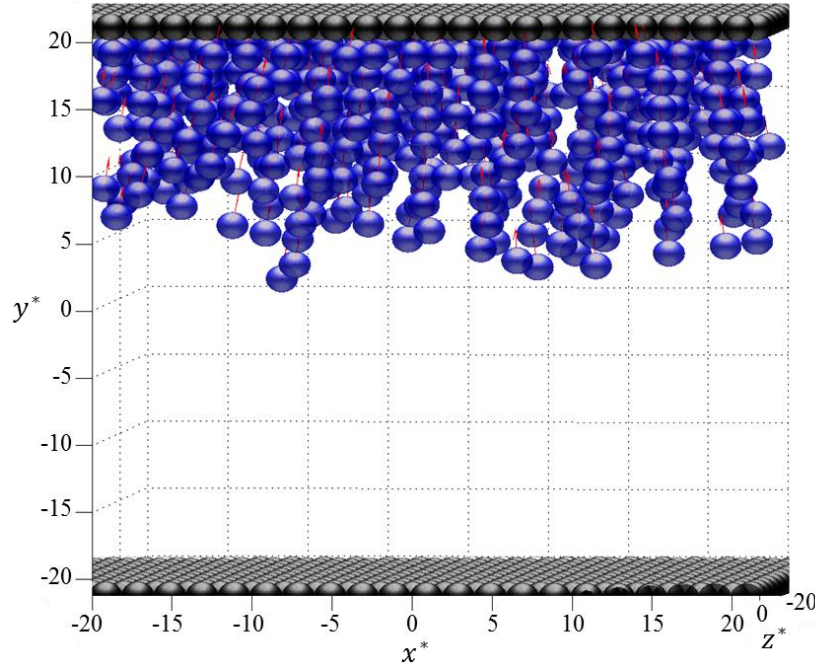
Figure 22. Spatial particle distribution under a magnetic field gradient ($\lambda = 9$, $R_\mathrm{m} = 50$). Through these parameters, magnetophoresis appeared to handily transport the particles with little impedance.

5.3.2 <u>**Particle Number Densities**</u>

Particle number density (PND) profiles supply a means to observe the progression towards steady-state magnetic separation via MP over time. The central objective for these plots requires data on the accumulation of particles at the top of the channel. At each *y*-coordinate, *xz*-planar volumes are allocated to determine the number density ρ_c in that particular region. Since, in this research, MP largely ensues in the *y*-direction, any diffusion in the *x*-direction is neglected for the PND profiles. A smoothed, two-dimensional plot is then derived to display the PND from the bottom of the channel $(y = -20a)$ to the top $(y = +20a)$, where the magnetic source is presumably located. This is generated at every increment of 10,000 time-steps until steady-state is attained, which allows an additional depth to the graphs that provides further understanding to the duration of magnetic separation under specific conditions.

As one can view in Figure 23, the particle population arises as an evenly-distributed (yet, with randomly-oriented dipoles) dispersion across the *y*-direction at $t = 0$. Then, as the magnetic gradient field is administered across the volume for $t > 0$, the particle assembly begins to shift toward regions of higher magnetism. With parameters of $\lambda = 3$ and $R_\mathrm{m} = 50$, the applied magnetic field and its gradient are not capable enough to impel every particle towards the area of higher magnetism at the top of the channel, which was evident in Figure 20. Note that near the bottom of the channel, number densities are always nonzero as time elapses beyond steady-state, verifying that the Brownian motion and steric repulsion hindered packing of magnetic particles at (and near) the maximum height once the concentration reached its limit.
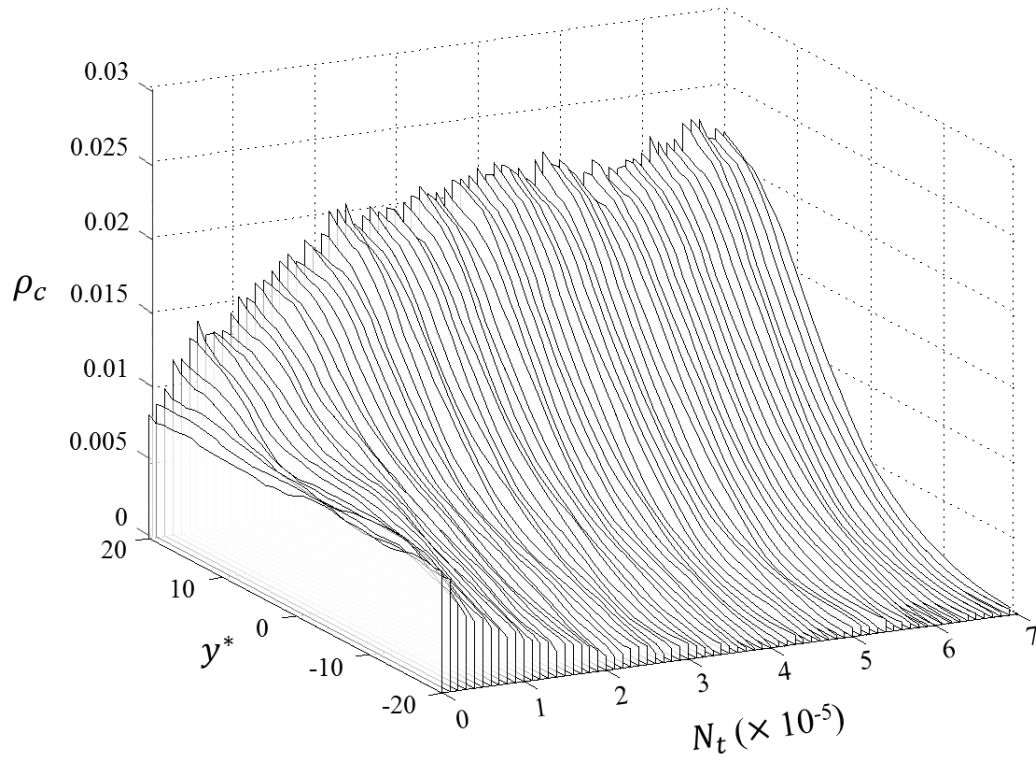
Figure 23. Progression of the particle number density profile ($\lambda = 3$, $R_{\mathrm{m}} = 50$). Number density remains nonzero across the entire system volume, implying partial separation.

By amplifying the strength of particle-particle interactions with an augmented value of λ, one can observe elevated number densities nearest the magnetic source and a noticeable deficit of particle population near the bottom portion of the channel as time elapses and before steady-state is achieved. The PND profile in Figure 24 provides a visualization. However, though the number densities have shifted upwards, the PND profiles corroborate with the commentary stated of Figure 21. The number density around $y = -5a$ never acquires a zero concentration, which verifies that this parameter set does not exemplify a suspension that would operate in profitable separation applications.
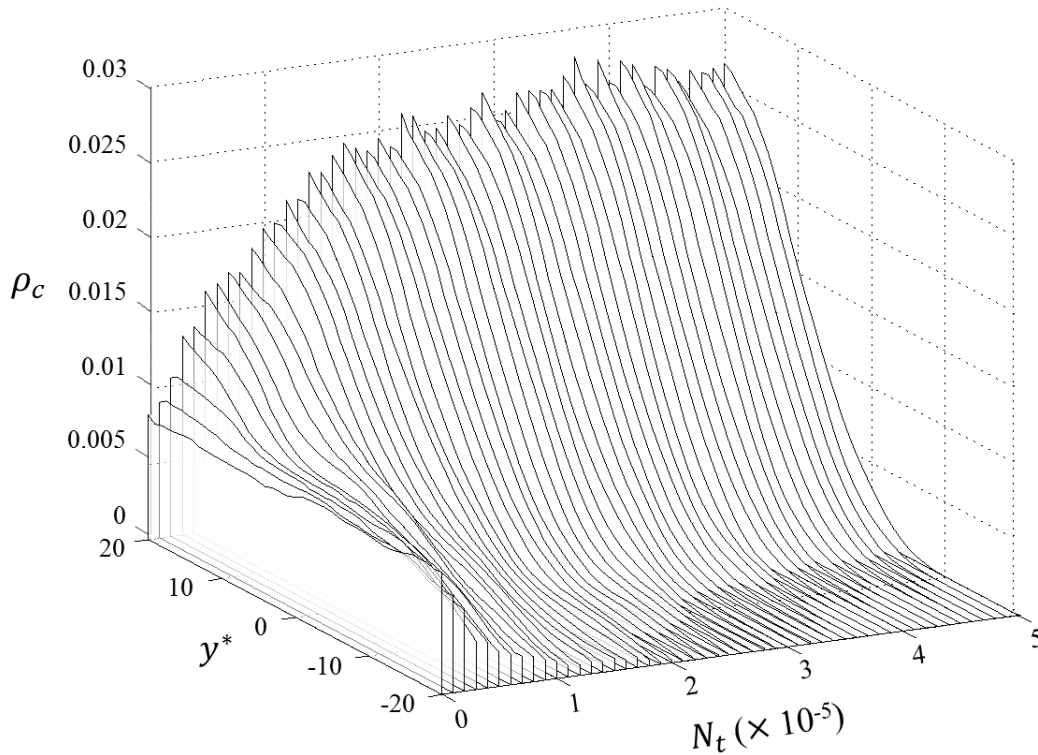
Figure 24. Progression of the particle number density profile ($\lambda = 5$, $R_m = 50$). At the topmost wall boundary, number density has acquired a steady-state quantity surpassing that for $\lambda = 3$.

With the greatest value of λ that this study considers, the PND profiles of Figure 22 are visible in Figure 25. Again, there is a distinctly larger number density near the upper half of the channel (and minimal concentrations for the bottom half) than the preceding sets of parameters produced. Also, the diffusion in the lower bisection insinuates a rapid separation time. Thus, efficient magnetic separation has been replicated with the least possible degrees of Brownian fluctuations and steric particle effects.
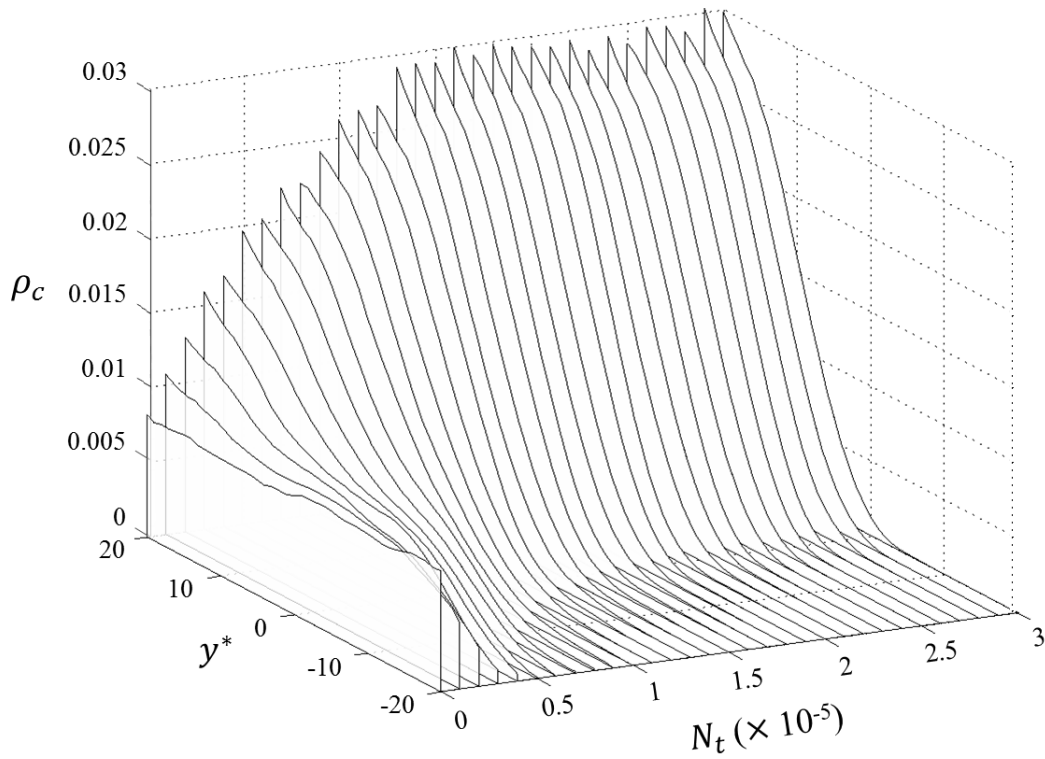
Figure 25. Progression of the particle number density profile ($\lambda = 9$, $R_{\mathrm{m}} = 50$). Along $y^* = 20$, the greatest number density is attained at steady-state due to strong magnetophoresis.

By reducing R_m to a relatively low quantity, one can produce a model under dominating

shear flow. Figure 26 characterizes the PND trends for this idea. One should discern that the

diffusion ensues much slower and arrives at a steady-state level at the top of the channel much

later than that of Figure 25. The denseness of the profiles alludes to the lengthy duration that the

parameter sets undergo. But even under the shear flow rate and in combination with the negligible

Brownian and steric influences, separation is still similar to that when $R_\mathrm{m} = 50$ in Figure 25. Since

the trends are of similar structure and number densities, one can deduce that the PND curves must

be similar in shape though separation may develop at differing rates. This conjecture will be

substantiated in a subsequent section.
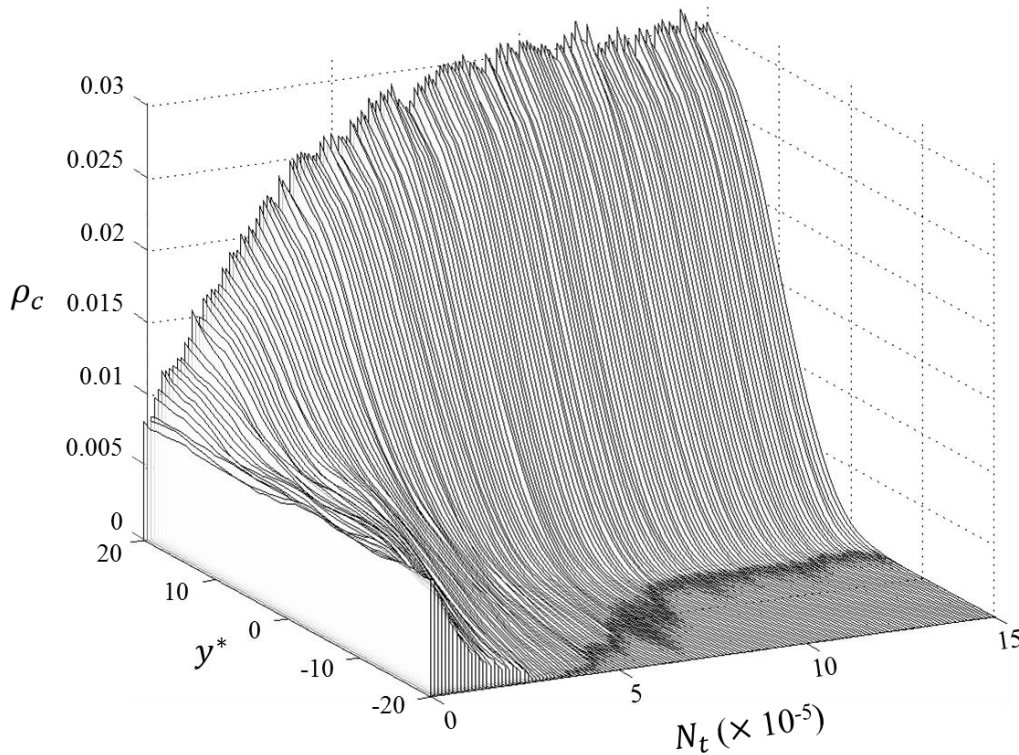
Figure 26. Progression of the particle number density profile ($\lambda = 9$, $R_\mathrm{m} = 10$). Despite substantial shear flow activity hampering particle diffusion, strong magnetophoresis produces effective separation.

5.3.3   **Separation Efficiency**

To confirm the validity of MP and success of the resultant magnetic separation, separation efficiency is continuously tracked while the simulation runs. The separation efficiency monitors the upper third of the channel volume and any particles within this designated span contribute to the total separation efficiency. Under the current conditions, total separation is accomplished when 90% of PND is within the stipulated section. Since the particles will migrate towards the top of the channel, this ensures a standard of magnetic separation for this model. Also note that separation efficiency does not commence at zero because the particles are first arranged as a randomized, equally-spaced distribution throughout the entirety of the system volume. Hence, a set fraction (about 15 to 20%, depending on the randomization) of the particles will initially be situated in the active separation zone at $t = 0$.

Figure 27 plots the separation efficiencies over time for $\lambda = 3$, $\lambda = 5$, $\lambda = 7$, and $\lambda = 9$, each under constant R_{m}. The trends certainly attain distinct yet unique steady-state levels, which correspond to the predetermined extent of separation in this research. Though these results reveal that the separation time scarcely differed over varying magnitudes of particle-particle interactions, the researchers are confident that the study is absent of any unrelated noncooperative MP effects. Conclusively, one can detect that only above a certain value of λ (in this case, $\lambda = 7$) will separation go to completion.
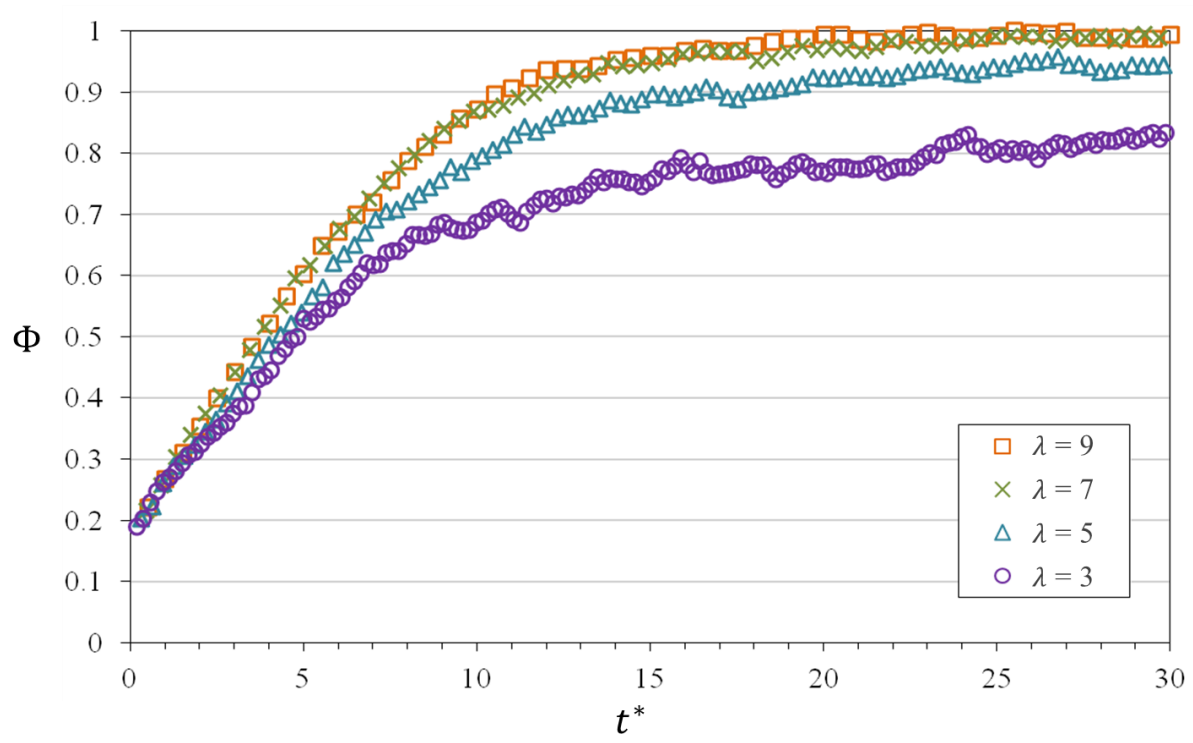
Figure 27. Separation efficiency trends for several degrees of particle-particle interaction ($R_\mathrm{m} = 50$).

For constant λ, Figure 28 exhibits the separation efficiencies over time for $R_m = 1$, $R_m = 25$, $R_m = 50$, and $R_m = 100$. Effective and complete separation is examined for all four of the parameter sets. Examination of the results in Figure 28 reveals that as the shearing rises, the slower diffusion becomes and hence, separation time is further delayed. By comparing these findings to those of Figure 27, one can surmise that the separation efficiency is dependent on Brownian motion and particle-particle interplay rather than shearing effects. Thus, it can be understood that in this research, particle-particle interactions manipulate the extent of the separation efficiency while shear flowing permits regulation of the separation time. Further analysis of the separation times should provide better confirmation of these phenomena.
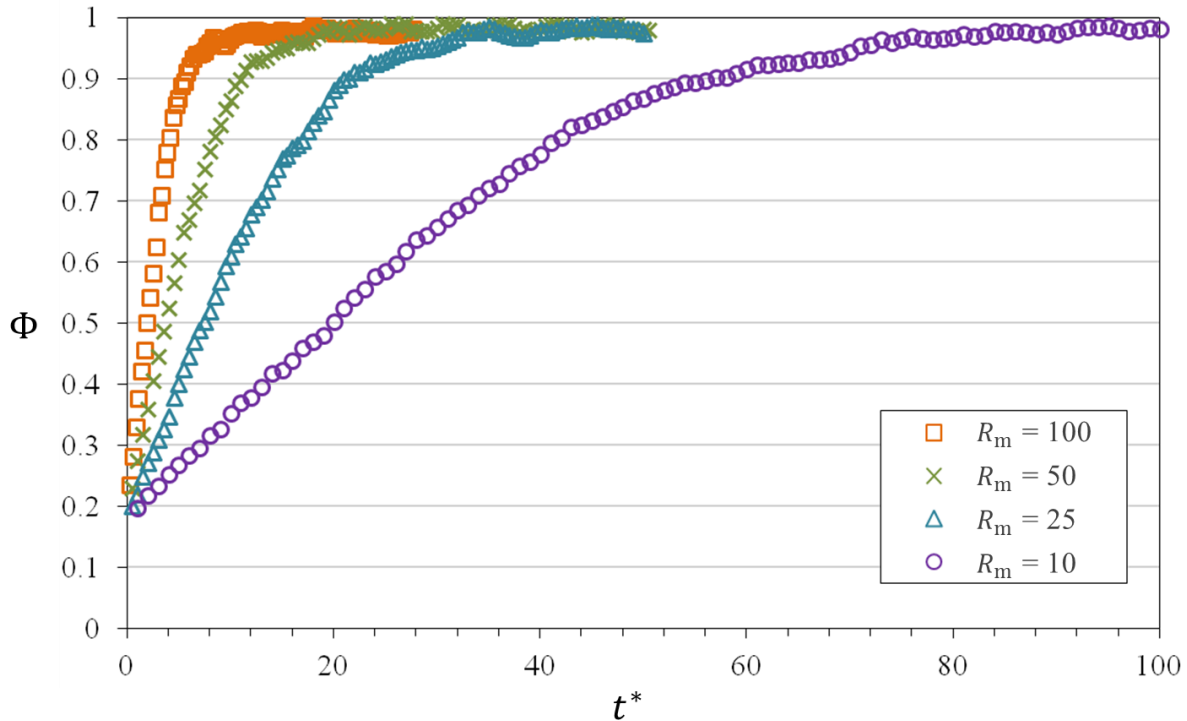
Figure 28. Separation efficiency trends for various intensities of shear flow effect ($\lambda = 9$).

5.3.4 **Separation Times**

By overseeing the separation efficiency to steady-state, the separation time can be derived. It is directly estimated by following the change of separation efficiency over time until the rate converges towards (and remains) zero. A simple technique that experimentalists tend to employ for ascertaining separation time is to meticulously monitor the dense ferrofluidic suspension under magnetic separation until a prearranged fraction of its initial opacity is reached. Typically, researchers operate setups that magnetically-extract particles from solution while simultaneously recording the opacity. The current study implements a similar analysis by conducting the procedure in reverse. Figure 29 plots the times that the separation efficiencies in Figure 28 take to approach their respective steady-state measures for different R_m values. The separation times from the runs with activated constraints (appearing as squares) nearly coincide with findings from De Las Cuevas *et al*. (2007) (expressed as circular outlines) while the unconstrained estimations (rendered as triangular characters) diverged from both. The faded line in Figure 29 correlates to a power law trend that fits the experimental data in the aforementioned literature. The model in this investigation seems fit to determine magnetic separation times under explicit conditions and assumptions for research in magnetophoresis of ferrofluidic particles.
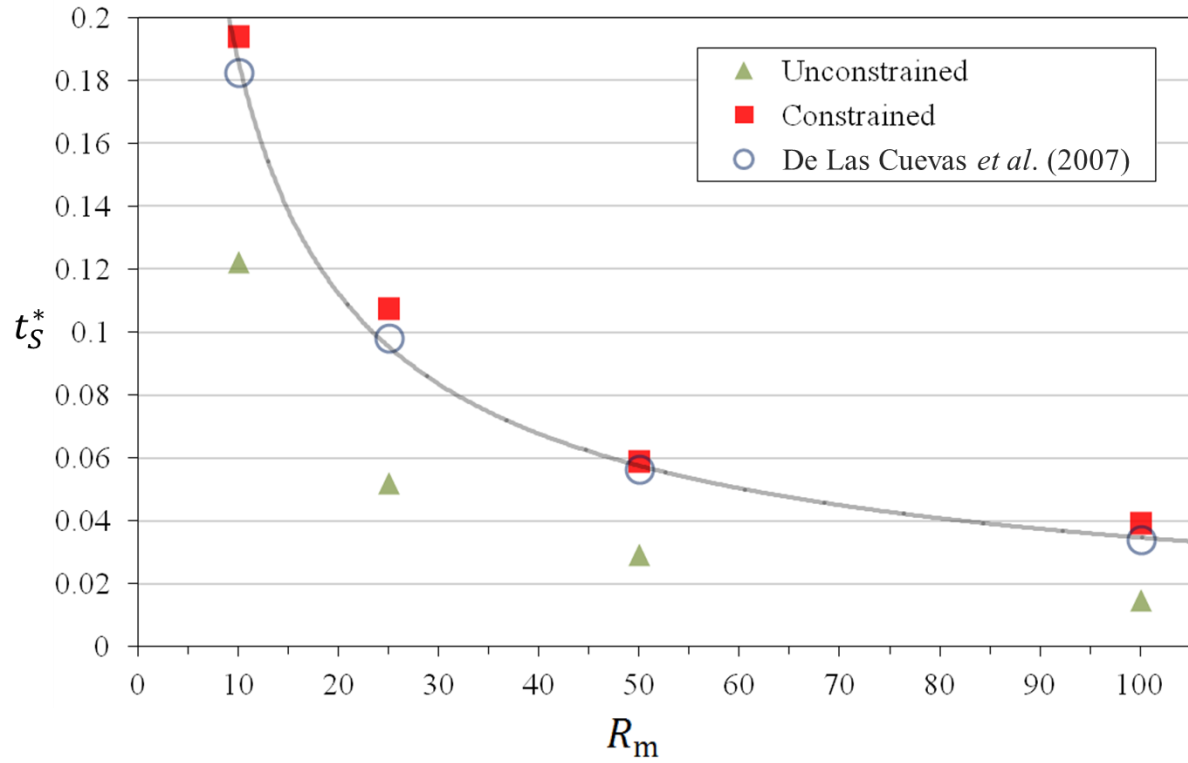
Figure 29. Dependence of separation time on shear flow effect ($\lambda = 9$). The faded line indicates the power law trend that fits De Las Cuevas *et al*. (2007).

6. CONCLUSIONS AND FUTURE WORK

The conducted research described in this thesis represents a significant step forward in the simulation of ferromagnetic fluids with magnetostatic properties. The approach is sufficient for the integrated flow and field conditions and a pseudo steady-state treatment of the magnetostatic forms of Maxwell's equations has been intentionally satisfied. By observing the movement of nanoscale ferrofluid particles over time, one can examine the magnetophoresis, the effect on characteristic times, and non-Newtonian fluid properties while satisfying the Maxwell's equations that are constrained by the proposed constraint algorithm.

Suspensions under uniformly applied magnetic fields explored the aggregation behavior of ferromagnetic particles by applying the magnetic field to the particulate system and urging it toward a steady-state. Pair correlation graphs supplied representations of particle grouping probability and chain compliance with the magnetic field. When not impacted by energetic Brownian motion, heavy shearing, or intense steric effects, pair correlation functions exhibited substantial spikes in sectors equating to likely chaining activity. This was associated with a combination of high λ and R_m. Time-averaged magnetoviscosity, a non-Newtonian fluid property characteristic of ferromagnetic colloidal suspensions, was assessed at steady-state to detect the impact that chaining had on the flow behavior. It increased over rising degrees of particle-particle interplay, low shear flow, and dwindling Brownian fluctuations. The results were then analyzed with experimental data from a published study. The trials with activated constraints were interpreted to agree with data from cited literature while the unconstrained runs did not. Then, to examine the diffusion behavior of a ferrofluid under magnetic field gradients, a nonuniformly applied field was applied to the particle system and allowed to run toward a suitable steady-state. This was accomplished by applying the nonuniform external magnetic field to a system setup

initially at random. Concentration profiles versus time assisted in determining when steady-state separation had occurred. Once the ferrofluid reached a steady-state in which the particles achieved a continuous agglomeration rate at the top of the microchannel, separation efficiencies were evaluated to assess the extent of magnetic separation. These were then wielded to estimate separation times, an aspect of magnetophoresis that is vital toward predicting separation behavior. Derived properties and characteristic behaviors (i.e. accumulating concentrations and characteristic times of magnetophoretic separation) aided in validating the simulations when compared to existing numbers from experiments. The pair correlation graphs remained closely similar to those of systems under uniform magnetic fields since the chaining behavior was not modified, unlike the particle diffusion. The ensuing results were compared to available data in order to justify a model capable of simulating magnetophoresis. The researchers trust that the findings accurately predict the behavior of ferrofluids in magnetic separation processes, which is an essential operation in the realm of ferromagnetic fluids. And finally, since the task of simulating systems of ferrofluid particles under uniformly and nonuniformly applied magnetic fields in a volume with shear flow and wall boundaries has been accomplished, the focus can now be diverted toward modeling other aspects that arise when utilizing ferrofluids, such as polydispersity or multiphase systems.

The proposed computational methodology should advance engineering fundamentals to unlock efficient three-dimensional simulations of ferromagnetic materials in various geometries. It should also increasingly exploit coupling between different transport and reactive phenomena and the interaction between fluids and any encompassing microfabricated systems. The simplifications of the past (particularly lumped parameter representation and separate treatment of phenomena) do not apply to increasingly integrated microprocesses, where geometric

details, surface properties, and boundary effects assume a dominant and determining role. Convoluted channel geometries can now be acknowledged, as blood vessels and other biosystems do not exist as flawless ideal cylinders. A byproduct of this effort should be a considerable savings in costly experimental trials, as new concepts and optimization variables can be first tried and vetted for feasibility and effectiveness on computers. The projected research stands poised to contribute fundamentals, simulation, and design capability to the field of ferrofluids and magnetostatics. Accurately validated computational simulations of microfluidic processes will help accumulate the requisite knowledge base.

CITED LITERATURE

Aminfar, H., Mohammadpourfard, M., and Zonouzi, S. A.: "Numerical Study of the Ferrofluid Flow and Heat Transfer through a Rectangular Duct in the Presence of a Non-uniform Transverse Magnetic Field." *Journal of Magnetism and Magnetic Materials*, 327: 31-42, 2013.

Andreu, J. S., Camacho, J., and Faraudo, J.: "Aggregation of Superparamagnetic Colloids in Magnetic Fields: The Quest for the Equilibrium State." *Soft Matter*, 7.6: 2336-2339, 2011.

Arsalani, N., Fattahi, H., Laurent, S., Burtea, C., Elst, L. V., and Muller, R. N.: "Polyglycerol-grafted Superparamagnetic Iron Oxide Nanoparticles: Highly Efficient MRI Contrast Agent for Liver and Kidney Imaging and Potential Scaffold for Cellular and Molecular Imaging." *Contrast Media & Molecular Imaging*, 7.2: 185-194, 2012.

Bird, R. B., Stewart, W. E., and Lightfoot, E. N.: *Transport Phenomena*. 2nd edition, New York, J. Wiley, 2002.

Chen, G., Ma, Y., Su, P., and Fang, B.: "Direct Binding Glucoamylase onto Carboxyl-functioned Magnetic Nanoparticles." *Biochemical Engineering Journal*, 67: 120-125, 2012.

De Las Cuevas, G., Faraudo, J., and Camacho, J.: "Low-Gradient Magnetophoresis through Field-Induced Reversible Aggregation." *The Journal of Physical Chemistry C*, 112.4: 945-950, 2008.

Dubina, S. H. and Wedgewood, L. E.: "A Brownian Dynamics Study on Ferrofluid Colloidal Dispersions Using an Iterative Constraint Method to Satisfy Maxwell's Equations." *Physics of Fluids*, 28.7: 072001, 2016.

Ermak, D. L. and McCammon, J. A.: "Brownian Dynamics with Hydrodynamic Interactions." *The Journal of Chemical Physics*, 69.4: 1352-1360, 1978.

Evans, D. J. and Murad, S.: "Singularity Free Algorithm for Molecular Dynamics Simulation of Rigid Polyatomics." *Molecular Physics*, 34.2: 327-331, 1977.

Faraudo, J., Andreu, J. S., and Camacho, J.: "Understanding Diluted Dispersions of Superparamagnetic Particles under Strong Magnetic Fields: A Review of Concepts, Theory and Simulations." *Soft Matter*, 9.29: 6654-6664, 2013.

Friedman, G., and Yellen, B.: "Magnetic Separation, Manipulation and Assembly of Solid Phase in Fluids." *Current Opinion in Colloid & Interface Science*, 10.3-4: 158-166, 2005.

Furlani, E. P.: "Magnetic Biotransport: Analysis and Applications." *Materials*, 3.4: 2412-2446, 2010.

CITED LITERATURE (continued)

Ganguly, R., Gaind, A. P., Sen, S., and Puri, I. K.: "Analyzing Ferrofluid Transport for Magnetic Drug Targeting." *Journal of Magnetism and Magnetic Materials*, 289: 331-334, 2005.

Goldstein, H.: *Classical Mechanics*. Reading, Addison-Wesley, 1971.

Heyes, D. M. and Melrose, J. R.: "Brownian Dynamics Simulations of Model Hard-sphere Suspensions." *Journal of Non-Newtonian Fluid Mechanics*, 46.1: 1-28, 1993.

Kim, D. K. and Dobson, J.: "Nanomedicine for Targeted Drug Delivery." *Journal of Materials Chemistry*, 19.35: 6294-6307, 2009.

Kim, S. and Karrila, S. J.: *Microhydrodynamics: Principles and Selected Applications*. Mineola, Dover Publications, 2005.

Kružík, M. and Prohl, A.: "Recent Developments in the Modeling, Analysis, and Numerics of Ferromagnetism." *SIAM Review*, 48.3: 439-483, 2006.

Kumar, D., Chandra, P., and Sinha, P.: "Ferrofluid Lubrication of Externally Pressurized Circular Plates and Conical Bearings." *International Journal of Engineering Science*, 31.4: 593-604, 1993.

Lai, D., Deng, L., Li, J., Liao, B., Guo, Q., and Fu, Y.: "Hydrolysis of Cellulose into Glucose by Magnetic Solid Acid." *ChemSusChem*, 4.1: 55-58, 2011.

Lebedev, V. T., Török, G., and Toperverg, B. P.: "Neutron Magnetic Tomography of Ferrofluids." *Journal of Magnetism and Magnetic Materials*, 252: 95-97, 2002.

Lim, J., Yeap, S. P., and Low, S. C.: "Challenges Associated to Magnetic Separation of Nanomaterials at Low Field Gradient." *Separation and Purification Technology*, 123: 171-174, 2014.

Liu, T. W.: "Flexible Polymer Chain Dynamics and Rheological Properties in Steady Flows." *The Journal of Chemical Physics*, 90.10: 5826-5842, 1989.

Miguel, M. and Pastor-Satorras, R.: "Kinetic Growth of Field-oriented Chains in Dipolar Colloidal Solutions." *Physical Review E*, 59.1: 826-834, 1999.

Mizuno, M., Yamada, M., Mitamura, R., Ike, K., Toyama, K., and Seki, M.: "Magnetophoresis-Integrated Hydrodynamic Filtration System for Size- and Surface Marker-Based Two-Dimensional Cell Sorting." *Analytical Chemistry*, 85.16: 7666-7673, 2013.

Moeser, G. D., Roach, K. A., Green, W. H., Hatton, T. A., and Laibinis, P. E.: "High-gradient Magnetic Separation of Coated Magnetic Nanoparticles." *AIChE Journal*, 50.11: 2835-2848, 2004.

CITED LITERATURE (continued)

Newbower, R. S.: "Magnetic Fluids in the Blood." *IEEE Transactions on Magnetics*, 9.3: 447-450, 1973.

Nguyen, N.: "Micro-magnetofluidics: Interactions between Magnetism and Fluid Flow on the Microscale." *Microfluidics and Nanofluidics*, 12.1-4: 1-16, 2011.

Nitsche, L. C. and Zhang, W.: "Atomistic SPH and a Link between Diffusion and Interfacial Tension." *AIChE Journal*, 48.2: 201-211, 2002.

Odenbach, S.: *Magnetoviscous Effects in Ferrofluids*. Berlin, Springer, 2002.

Odenbach, S., and Störk, H.: "Shear Dependence of Field-induced Contributions to the Viscosity of Magnetic Fluids at Low Shear Rates." *Journal of Magnetism and Magnetic Materials*, 183.1-2: 188-194, 1998.

Öttinger, H. C.: *Stochastic Processes in Polymeric Fluids: Tools and Examples for Developing Simulation Algorithms*. Berlin, Springer, 1996.

Papadopoulos, P. K., Vafeas, P. and Hatzikonstantinou, P. M.: "Ferrofluid Pipe Flow under the Influence of the Magnetic Field of a Cylindrical Coil." *Physics of Fluids*, 24.12: 122002, 2012.

Pourjavadi, A., Hosseini, S. H., Doulabi, M., Fakoorpoor, S. M., and Seidi, F.: "Multi-Layer Functionalized Poly(Ionic Liquid) Coated Magnetic Nanoparticles: Highly Recoverable and Magnetically Separable Brønsted Acid Catalyst." *ACS Catalysis*, 2.6: 1259-1266, 2012.

Raj, K., Moskowitz, B., and Casciari, R.: "Advances in Ferrofluid Technology." *Journal of Magnetism and Magnetic Materials*, 149.1-2: 174-180, 1995.

Ravaud, R., Lemarquand, G., and Lemarquand, V.: "Mechanical Properties of Ferrofluid Applications: Centering Effect and Capacity of a Seal." *Tribology International*, 43.1-2: 76-82, 2010.

Rosensweig, R. E.: *Ferrohydrodynamics*. Cambridge, Cambridge University Press, 1985.

Rosensweig, R. E.: "Process Concepts Using Field-stabilized Two-phase Fluidized Flow." *Journal of Electrostatics*, 34.2-3: 163-187, 1995.

Rümenapp, C., Gleich, B., and Haase, A.: "Magnetic Nanoparticles in Magnetic Resonance Imaging and Diagnostics." *Pharmaceutical Research*, 29.5: 1165-1179, 2012.

CITED LITERATURE (continued)

Ryckaert, J., Ciccotti, G., and Berendsen, H. J.: "Numerical Integration of the Cartesian Equations of Motion of a System with Constraints: Molecular Dynamics of N-alkanes." *Journal of Computational Physics*, 23.3: 327-341, 1977.

Satoh, A., Chantrell, R. W., and Coverdale, G. N.: "Brownian Dynamics Simulations of Ferromagnetic Colloidal Dispersions in a Simple Shear Flow." *Journal of Colloid and Interface Science*, 209.1: 44-59, 1999.

Satoh, A., Chantrell, R. W., Coverdale, G. N. and Kamiyama, S.: "Stokesian Dynamics Simulations of Ferromagnetic Colloidal Dispersions in a Simple Shear Flow." *Journal of Colloid and Interface Science*, 203.2: 233-248, 1998.

Schaller, V., Kräling, U., Rusu, C., Petersson, K., Wipenmyr, J., Krozer, A., Wahnström, G., Sanz-Velasco, A., Enoksson, P., and Johansson, C.: "Motion of Nanometer Sized Magnetic Particles in a Magnetic Field Gradient." *Journal of Applied Physics*, 104.9: 093918, 2008.

Schinteie, G., Palade, P., Vekas, L., Iacob, N., Bartha, C., and Kuncser, V.: "Volume Fraction Dependent Magnetic Behaviour of Ferrofluids for Rotating Seal Applications." *Journal of Physics D: Applied Physics*, 46.39: 395501, 2013.

Shliomis, M. I.: "Magnetic Fluids." *Soviet Physics Uspekhi*, 17.2: 153-169, 1974.

Sinha, A., Ganguly, R., De, A. K., and Puri, I. K.: "Single Magnetic Particle Dynamics in a Microchannel." *Physics of Fluids*, 19.11: 117102, 2007.

Suwa, M. and Watarai, H.: "Magnetoanalysis of Micro/nanoparticles: A Review." *Analytica Chimica Acta*, 690.2: 137-147, 2011.

Tiberto, P., Barrera, G., Celegato, F., Coïsson, M., Chiolerio, A., Martino, P., Pandolfi, P., and Allia, P.: "Magnetic Properties of Jet-printer Inks Containing Dispersed Magnetite Nanoparticles." *The European Physical Journal B*, 86.4: 173, 2013.

Watarai, H., Suwa, M., and Iiguni, Y.: "Magnetophoresis and Electromagnetophoresis of Microparticles in Liquids." *Analytical and Bioanalytical Chemistry*, 378.7: 1693-1699, 2004.

Wu, X., Wu, H., and Hu, Y.: "Enhancement of Separation Efficiency on Continuous Magnetophoresis by Utilizing L/T-shaped Microchannels." *Microfluidics and Nanofluidics*, 11.1: 11-24, 2011.

Yavuz, C. T., Mayo, J. T., Yu, W. W., Prakash, A., Falkner, J. C., Yean, S., Cong, L., Shipley, H. J., Kan, A., Tomson, M., Natelson, D., and Colvin, V. L.: "Low-Field Magnetic Separation of Monodisperse Fe3O4 Nanocrystals." *Science*, 314.5801: 964-967, 2006.

CITED LITERATURE (continued)

Yavuz, C. T., Prakash, A., Mayo, J. T. and Colvin, V. L.: "Magnetic Separations: From Steel Plants to Biotechnology." *Chemical Engineering Science*, 64.10: 2510-2521, 2009.

Zeng, J., Deng, Y., Vedantam, P., Tzeng, T., and Xuan, X.: "Magnetic Separation of Particles and Cells in Ferrofluid Flow through a Straight Microchannel Using Two Offset Magnets." *Journal of Magnetism and Magnetic Materials*, 346: 118-123, 2013.

Zubarev, A. Y.: "On the Theory of Transport Phenomena in Ferrofluids. Effect of Chain-like Aggregates." *Physica A: Statistical Mechanics and Its Applications*, 392.1: 72-78, 2013.

BIBLIOGRAPHY

Bossis, G. and Brady, J. F.: "Self-diffusion of Brownian Particles in Concentrated Suspensions under Shear." *The Journal of Chemical Physics*, 87.9: 5437-5448, 1987.

Bou-Reslan, D.: "Brownian Dynamics Simulation of Ferromagnetic Fluid in the Vicinity of a Solid Wall in Shear Flow." Master's thesis, University of Illinois at Chicago, Chicago, 2002.

Brady, J. F., Phillips, R. J., Lester, J. C., and Bossis, G.: "Dynamic Simulation of Hydrodynamically Interacting Suspensions." *Journal of Fluid Mechanics*, 195.1: 257-280, 1988.

Brady, J. F.: "The Rheological Behavior of Concentrated Colloidal Dispersions." *The Journal of Chemical Physics*, 99.1: 567-581, 1993.

Kim, S. and Mifflin, R. T.: "The Resistance and Mobility Functions of Two Equal Spheres in Low-Reynolds-number Flow." *Physics of Fluids*, 28.7: 2033-2045, 1985.

Müller, H. W. and Liu, M.: "Structure of Ferrofluid Dynamics." *Physical Review*, 64.6: 1-7, 2001.

APPENDICES

Appendix A

Mobility Functions

Here, the mobility functions introduced in Chapter 3 are defined:

$$\mathbf{a}_{ij}^{(\alpha\beta)} = x_{\alpha\beta}^{\mathrm{a}} d_i d_j + y_{\alpha\beta}^{\mathrm{a}} (\delta_{ij} - d_i d_j) \qquad [\text{A.1}]$$

$$\mathbf{b}_{ij}^{(\alpha\beta)} = y_{\alpha\beta}^{\mathrm{b}} \varepsilon_{ijk} d_k \qquad [\text{A.2}]$$

$$\mathbf{c}_{ij}^{(\alpha\beta)} = x_{\alpha\beta}^{\mathrm{c}} d_i d_j + y_{\alpha\beta}^{\mathrm{c}} (\delta_{ij} - d_i d_j) \qquad [\text{A.3}]$$

$$\mathbf{g}_{ijk}^{(\alpha\beta)} = x_{\alpha\beta}^{\mathrm{g}} \left(d_i d_j - \frac{1}{3}\delta_{ij} \right) d_k + y_{\alpha\beta}^{\mathrm{g}} (d_i \delta_{jk} + d_j \delta_{ik} - 2d_i d_j d_k) \qquad [\text{A.4}]$$

$$\mathbf{h}_{ijk}^{(\alpha\beta)} = y_{\alpha\beta}^{\mathrm{h}} (\varepsilon_{ikl} d_l d_j + \varepsilon_{jkl} d_l d_i) \qquad [\text{A.5}]$$

where $x_{\alpha\beta}^{\mathrm{a}}$, $y_{\alpha\beta}^{\mathrm{a}}$, $y_{\alpha\beta}^{\mathrm{b}}$, $x_{\alpha\beta}^{\mathrm{c}}$, $y_{\alpha\beta}^{\mathrm{c}}$, $x_{\alpha\beta}^{\mathrm{g}}$, $y_{\alpha\beta}^{\mathrm{g}}$, and $y_{\alpha\beta}^{\mathrm{h}}$ are scalar mobility functions, $\boldsymbol{d}$ is the unit direction vector from particle α to β, and the permutation symbol is:

$$\varepsilon_{ijk} = \begin{cases} +1 & if\ ijk = 123,231,312 \\ -1 & if\ ijk = 321,132,213 \\ 0 & if\ i = j, i = k, j = k \end{cases} \qquad [\text{A.6}]$$

Also, $\varepsilon_{ijk} = \frac{1}{2}(i-j)(j-k)(k-i)$. Values for the scalar mobility functions are tabulated by Kim and Karilla (1991). They can also be nondimensionalized. To do so, scaling parameters must be used: $6\pi a$ is for the functions of second-rank tensor $\mathbf{a}$, $4\pi a^2$ is for those of second-rank tensor $\mathbf{b}$, $8\pi a^3$ is for those of second-rank tensor $\mathbf{c}$, and $2a$ is for those of third-rank tensor $\mathbf{g}$.

The near-field mobility functions are dependent on the dimensionless parameter:

$$\xi_n = \frac{2(r - a - b)}{a + b} \qquad [\text{A.7}]$$

while the far-field mobility functions are dependent on:

$$\xi_f = \frac{a}{2r} \qquad\qquad \text{[A.8]}$$

For particles with uniform radii ($a = b$) and by nondimensionalizing the distances, $\xi_n = r^* - 2$ and $\xi_f = (2r^*)^{-1}$.

Appendix B

Constraint Derivatives

As seen in equation [3.79], the derivatives of the constraints with respect to position and orientation are required. As for the Gauss's Law constraints, the derivatives of the first term in equation [3.86] are as follows:

$$
\frac{\partial \sigma_G}{\partial r_{\alpha x}} = \Delta S \sum_k \frac{6}{h^2} \left[n_{Sx} \sum_\alpha n_{\alpha x}(r_{\alpha x} - r_{kx}) \left(\frac{N_{k\alpha}}{h} - 1 \right) \right.
$$
$$
+ n_{Sy} \sum_\alpha n_{\alpha y}(r_{\alpha x} - r_{kx}) \left(\frac{N_{k\alpha}}{h} - 1 \right)
$$
$$
\left. + n_{Sz} \sum_\alpha n_{\alpha z}(r_{\alpha x} - r_{kx}) \left(\frac{N_{k\alpha}}{h} - 1 \right) \right] \tag{B.1}
$$

$$
\frac{\partial \sigma_G}{\partial r_{\alpha y}} = \Delta S \sum_k \frac{6}{h^2} \left[n_{Sx} \sum_\alpha n_{\alpha x}(r_{\alpha y} - r_{ky}) \left(\frac{N_{k\alpha}}{h} - 1 \right) \right.
$$
$$
+ n_{Sy} \sum_\alpha n_{\alpha y}(r_{\alpha y} - r_{ky}) \left(\frac{N_{k\alpha}}{h} - 1 \right)
$$
$$
\left. + n_{Sz} \sum_\alpha n_{\alpha z}(r_{\alpha y} - r_{ky}) \left(\frac{N_{k\alpha}}{h} - 1 \right) \right] \tag{B.2}
$$

$$
\frac{\partial \sigma_G}{\partial r_{\alpha z}} = \Delta S \sum_k \frac{6}{h^2} \left[n_{Sx} \sum_\alpha n_{\alpha x}(r_{\alpha z} - r_{kz}) \left(\frac{N_{k\alpha}}{h} - 1 \right) \right.
$$
$$
+ n_{Sy} \sum_\alpha n_{\alpha y}(r_{\alpha z} - r_{kz}) \left(\frac{N_{k\alpha}}{h} - 1 \right)
$$
$$
\left. + n_{Sz} \sum_\alpha n_{\alpha z}(r_{\alpha z} - r_{kz}) \left(\frac{N_{k\alpha}}{h} - 1 \right) \right] \tag{B.3}
$$

$$
\frac{\partial \sigma_G}{\partial n_{\alpha x}} = n_{Sx} \Delta S \sum_k \sum_\alpha W_{k\alpha} \tag{B.4}
$$

$$
\frac{\partial \sigma_G}{\partial n_{\alpha y}} = n_{Sy} \Delta S \sum_k \sum_\alpha W_{k\alpha} \tag{B.5}
$$

$$
\frac{\partial \sigma_G}{\partial n_{\alpha z}} = n_{Sz} \Delta S \sum_k \sum_\alpha W_{k\alpha} \tag{B.6}
$$

In the above constraint derivatives, $N_{k\alpha}$ represents the norm of the $\boldsymbol{r}_\alpha - \boldsymbol{r}_k$ vector, $\boldsymbol{r}_k$ denotes the position vector of node k, and $W_{k\alpha}$ is the weighting function in equation [3.73]. Also, the normal vector $\boldsymbol{n}_S$ will be either -1 or 1, depending on which surface the kth node is present. As for the second term in equation [3.86], the constraint derivatives are as follows:

$$
\begin{aligned}
\frac{\partial \sigma_G}{\partial r_{\alpha x}} = \frac{1}{4\pi} \sum_l \frac{1}{|\boldsymbol{r}_{l\alpha}|^5} \Big\{ & n_{Sx}\Big[3[\boldsymbol{n}_\alpha \cdot \boldsymbol{r}_{l\alpha} + n_{x\alpha}(r_{x\alpha} - r_{xl})] \\
& - \frac{15}{|\boldsymbol{r}_{l\alpha}|^2}(\boldsymbol{n}_\alpha \cdot \boldsymbol{r}_{l\alpha})(r_{x\alpha} - r_{xl})^2 + 3(r_{x\alpha} - r_{xl})n_{x\alpha}\Big] \\
& + n_{Sy}\Big[3n_{x\alpha}(r_{y\alpha} - r_{yl}) \\
& - \frac{15}{|\boldsymbol{r}_{l\alpha}|^2}(\boldsymbol{n}_\alpha \cdot \boldsymbol{r}_{l\alpha})(r_{x\alpha} - r_{xl})(r_{y\alpha} - r_{yl}) \\
& + 3(r_{x\alpha} - r_{xl})n_{y\alpha}\Big] \\
& + n_{Sz}\Big[3n_{x\alpha}(r_{z\alpha} - r_{zl}) \\
& - \frac{15}{|\boldsymbol{r}_{l\alpha}|^2}(\boldsymbol{n}_\alpha \cdot \boldsymbol{r}_{l\alpha})(r_{x\alpha} - r_{xl})(r_{z\alpha} - r_{zl}) \\
& + 3(r_{x\alpha} - r_{xl})n_{z\alpha}\Big] \Big\}
\end{aligned}
\tag{B.7}
$$

$$
\begin{aligned}
\frac{\partial \sigma_G}{\partial r_{\alpha y}} = \frac{1}{4\pi} \sum_l \frac{1}{|\boldsymbol{r}_{l\alpha}|^5} \Big\{ & n_{Sx}\Big[3n_{y\alpha}(r_{x\alpha} - r_{xl}) \\
& - \frac{15}{|\boldsymbol{r}_{l\alpha}|^2}(\boldsymbol{n}_\alpha \cdot \boldsymbol{r}_{l\alpha})(r_{y\alpha} - r_{yl})(r_{x\alpha} - r_{xl}) \\
& + 3(r_{y\alpha} - r_{yl})n_{x\alpha}\Big] \\
& + n_{Sy}\Big[3[\boldsymbol{n}_\alpha \cdot \boldsymbol{r}_{l\alpha} + n_{y\alpha}(r_{y\alpha} - r_{yl})] \\
& - \frac{15}{|\boldsymbol{r}_{l\alpha}|^2}(\boldsymbol{n}_\alpha \cdot \boldsymbol{r}_{l\alpha})(r_{y\alpha} - r_{yl})^2 + 3(r_{y\alpha} - r_{yl})n_{y\alpha}\Big] \\
& + n_{Sz}\Big[3n_{y\alpha}(r_{z\alpha} - r_{zl}) \\
& - \frac{15}{|\boldsymbol{r}_{l\alpha}|^2}(\boldsymbol{n}_\alpha \cdot \boldsymbol{r}_{l\alpha})(r_{y\alpha} - r_{yl})(r_{z\alpha} - r_{zl}) \\
& + 3(r_{y\alpha} - r_{yl})n_{z\alpha}\Big] \Big\}
\end{aligned}
\tag{B.8}
$$

$$\frac{\partial \sigma_G}{\partial r_{\alpha z}} = \frac{1}{4\pi} \sum_l \frac{1}{|\boldsymbol{r}_{l\alpha}|^5} \Bigg\{ n_{Sx} \Big[3n_{z\alpha}(r_{x\alpha} - r_{xl})$$

$$- \frac{15}{|\boldsymbol{r}_{l\alpha}|^2} (\boldsymbol{n}_\alpha \cdot \boldsymbol{r}_{l\alpha})(r_{z\alpha} - r_{zl})(r_{x\alpha} - r_{xl})$$

$$+ 3(r_{z\alpha} - r_{zl})n_{x\alpha} \Big]$$

$$+ n_{Sy} \Big[3n_{z\alpha}(r_{y\alpha} - r_{yl})$$

$$- \frac{15}{|\boldsymbol{r}_{l\alpha}|^2} (\boldsymbol{n}_\alpha \cdot \boldsymbol{r}_{l\alpha})(r_{z\alpha} - r_{zl})(r_{y\alpha} - r_{yl})$$

$$+ 3(r_{z\alpha} - r_{zl})n_{y\alpha} \Big]$$

$$+ n_{Sz} \Big[3[\boldsymbol{n}_\alpha \cdot \boldsymbol{r}_{l\alpha} + n_{z\alpha}(r_{z\alpha} - r_{zl})]$$

$$- \frac{15}{|\boldsymbol{r}_{l\alpha}|^2} (\boldsymbol{n}_\alpha \cdot \boldsymbol{r}_{l\alpha})(r_{z\alpha} - r_{zl})^2 + 3(r_{z\alpha} - r_{zl})n_{z\alpha} \Big] \Bigg\} \qquad \text{[B.9]}$$

$$\frac{\partial \sigma_G}{\partial n_{\alpha x}} = \frac{1}{4\pi} \sum_l \frac{1}{|\boldsymbol{r}_{l\alpha}|^3} \Bigg\{ \frac{3(r_{x\alpha} - r_{xl})}{|\boldsymbol{r}_{l\alpha}|^2} \big[(r_{x\alpha} - r_{xl})n_{Sx} + (r_{y\alpha} - r_{yl})n_{Sy}$$

$$+ (r_{z\alpha} - r_{zl})n_{Sz} \big] - n_{Sx} \Bigg\} \qquad \text{[B.10]}$$

$$\frac{\partial \sigma_G}{\partial n_{\alpha y}} = \frac{1}{4\pi} \sum_l \frac{1}{|\boldsymbol{r}_{l\alpha}|^3} \Bigg\{ \frac{3(r_{y\alpha} - r_{yl})}{|\boldsymbol{r}_{l\alpha}|^2} \big[(r_{x\alpha} - r_{xl})n_{Sx} + (r_{y\alpha} - r_{yl})n_{Sy}$$

$$+ (r_{z\alpha} - r_{zl})n_{Sz} \big] - n_{Sy} \Bigg\} \qquad \text{[B.11]}$$

$$\frac{\partial \sigma_G}{\partial n_{\alpha z}} = \frac{1}{4\pi} \sum_l \frac{1}{|\boldsymbol{r}_{l\alpha}|^3} \Bigg\{ \frac{3(r_{z\alpha} - r_{zl})}{|\boldsymbol{r}_{l\alpha}|^2} \big[(r_{x\alpha} - r_{xl})n_{Sx} + (r_{y\alpha} - r_{yl})n_{Sy}$$

$$+ (r_{z\alpha} - r_{zl})n_{Sz} \big] - n_{Sz} \Bigg\} \qquad \text{[B.12]}$$

In the preceding constraint derivatives, $r_{l\alpha}$ is the distance from node l to particle α.

The derivatives for the Ampère's Law constraints are as follows:

$$\frac{\partial \sigma_A}{\partial r_{\alpha x}} = \sum_k \sum_l \frac{6}{h^2} \frac{1}{|\boldsymbol{r}_{lk}|^3} (r_{\alpha x} - r_{kx}) \left(\frac{N_{k\alpha}}{h} - 1 \right) \Bigg[\frac{3(\boldsymbol{n}_\alpha \cdot \boldsymbol{r}_{lk})}{|\boldsymbol{r}_{lk}|^2} (\boldsymbol{r}_{lk} \cdot \Delta \boldsymbol{l})$$

$$- (\boldsymbol{n}_\alpha \cdot \Delta \boldsymbol{l}) \Bigg] \qquad \text{[B.13]}$$

$$\frac{\partial \sigma_A}{\partial r_{\alpha y}} = \sum_k \sum_l \frac{6}{h^2} \frac{1}{|\boldsymbol{r}_{lk}|^3} (r_{\alpha y} - r_{ky}) \left(\frac{N_{k\alpha}}{h} - 1\right) \left[\frac{3(\boldsymbol{n}_\alpha \cdot \boldsymbol{r}_{lk})}{|\boldsymbol{r}_{lk}|^2} (\boldsymbol{r}_{lk} \cdot \Delta \boldsymbol{l})\right.$$
$$\left. - (\boldsymbol{n}_\alpha \cdot \Delta \boldsymbol{l})\right] \qquad \text{[B.14]}$$

$$\frac{\partial \sigma_A}{\partial r_{\alpha z}} = \sum_k \sum_l \frac{6}{h^2} \frac{1}{|\boldsymbol{r}_{lk}|^3} (r_{\alpha z} - r_{kz}) \left(\frac{N_{k\alpha}}{h} - 1\right) \left[\frac{3(\boldsymbol{n}_\alpha \cdot \boldsymbol{r}_{lk})}{|\boldsymbol{r}_{lk}|^2} (\boldsymbol{r}_{lk} \cdot \Delta \boldsymbol{l})\right.$$
$$\left. - (\boldsymbol{n}_\alpha \cdot \Delta \boldsymbol{l})\right] \qquad \text{[B.15]}$$

$$\frac{\partial \sigma_A}{\partial n_{\alpha x}} = \sum_k \sum_l \frac{W_{k\alpha}}{|\boldsymbol{r}_{lk}|^3} \left[\frac{3}{|\boldsymbol{r}_{lk}|^2} (\boldsymbol{r}_{lk} \cdot \Delta \boldsymbol{l}) r_{lkx} - \Delta l_x\right] \qquad \text{[B.16]}$$

$$\frac{\partial \sigma_A}{\partial n_{\alpha y}} = \sum_k \sum_l \frac{W_{k\alpha}}{|\boldsymbol{r}_{lk}|^3} \left[\frac{3}{|\boldsymbol{r}_{lk}|^2} (\boldsymbol{r}_{lk} \cdot \Delta \boldsymbol{l}) r_{lky} - \Delta l_y\right] \qquad \text{[B.17]}$$

$$\frac{\partial \sigma_A}{\partial n_{\alpha z}} = \sum_k \sum_l \frac{W_{k\alpha}}{|\boldsymbol{r}_{lk}|^3} \left[\frac{3}{|\boldsymbol{r}_{lk}|^2} (\boldsymbol{r}_{lk} \cdot \Delta \boldsymbol{l}) r_{lkz} - \Delta l_z\right] \qquad \text{[B.18]}$$

In these constraint derivatives, r_{lk} is the distance from node l to node k. The node index of k' was replaced with l to avoid confusion with the subscripts.

Appendix C

FORTRAN Code for the Constraint Algorithm

```fortran
!################################################################################
!Subroutine to satisfy Maxwell's equations using an iterative constraint method
    SUBROUTINE M_E_CONST(rs_x,rs_y,rs_z,ns_x,ns_y,ns_z,rc_x,rc_y,rc_z, &
                    nc_x,nc_y,nc_z,L,tlrc_a,tlrc_b,k,N1,N7,drcn,Nc,Ncs,Ns_int, &
                    rcnv_x,rcnv_y,rcnv_z,ncnv_x,ncnv_y,ncnv_z,Nca,Nsl,Ncnl,Ncnl4, &
                    rcnl_x,rcnl_y,rcnl_z,ncnl_x,ncnl_y,ncnl_z,w_swtch)
!Constraint properties for Maxwell's equations (Gauss' law)
    INTEGER :: Nc,Ncs,Ns_int
    DOUBLE PRECISION, DIMENSION(Ns_int*Ncs*Nc) :: rcnv_x,rcnv_y,rcnv_z
    DOUBLE PRECISION, DIMENSION(Ns_int*Ncs*Nc) :: ncnv_x,ncnv_y,ncnv_z
    DOUBLE PRECISION, DIMENSION(Ns_int*Ncs*Nc) :: Mnt,M_x,M_y,M_z
    DOUBLE PRECISION, DIMENSION(Ns_int*Ncs*Nc) :: Md_x,Md_y,Md_z
    DOUBLE PRECISION, DIMENSION(Nc*2) :: Mnt_x,Mnt_y,Mnt_z,Hnt_x,Hnt_y,Hnt_z
!Constraint properties for Maxwell's equations (Ampere's law)
    INTEGER :: Nca,Ncnl,Ncnl4,Nsl
    DOUBLE PRECISION, DIMENSION(Nca) :: Hdl_x,Hdl_y,Hdl_z
    DOUBLE PRECISION, DIMENSION(4*Nsl*Nca) :: Hdlt_x,Hdlt_y,Hdlt_z
    DOUBLE PRECISION, DIMENSION(Ncnl4*Nsl*Nca) :: rcnl_x,rcnl_y,rcnl_z
    DOUBLE PRECISION, DIMENSION(Ncnl4*Nsl*Nca) :: ncnl_x,ncnl_y,ncnl_z
    DOUBLE PRECISION, DIMENSION(Ncnl4*Nsl*Nca) :: Mda_x,Mda_y,Mda_z
!Other Constraint parameters
    INTEGER :: N1,N7
    DOUBLE PRECISION, DIMENSION(Nc+Nca) :: sgm,sgm_t,Lmbd,b_arr,x_tmp
    DOUBLE PRECISION, DIMENSION(0:N1,Nc+Nca) :: drs_x,drs_y,drs_z
    DOUBLE PRECISION, DIMENSION(0:N1,Nc+Nca) :: dns_x,dns_y,dns_z
    DOUBLE PRECISION, DIMENSION(0:N1,Nc+Nca) :: drc_x,drc_y,drc_z
    DOUBLE PRECISION, DIMENSION(0:N1,Nc+Nca) :: dnc_x,dnc_y,dnc_z
    DOUBLE PRECISION, DIMENSION(Nc+Nca,Nc+Nca+1) :: c_tmp
    DOUBLE PRECISION, DIMENSION(Nc+Nca,Nc+Nca) :: g_arr,mod_G,mod_Gt
    DOUBLE PRECISION, DIMENSION(Nc+Nca,Nc+Nca) :: b_arr_tmp,Lmt,U_tmp
    DOUBLE PRECISION, DIMENSION(0:N7), INTENT(INOUT) :: rs_x,rs_y,rs_z
    DOUBLE PRECISION, DIMENSION(0:N7), INTENT(INOUT) :: rc_x,rc_y,rc_z
    DOUBLE PRECISION, DIMENSION(0:N7), INTENT(INOUT) :: ns_x,ns_y,ns_z
    DOUBLE PRECISION, DIMENSION(0:N7), INTENT(INOUT) :: nc_x,nc_y,nc_z
    DOUBLE PRECISION, DIMENSION(0:N1) :: Cff,rct_x,rct_y,rct_z,nct_x,nct_y,nct_z
    DOUBLE PRECISION, DIMENSION(0:N1) :: Tc_x,Tc_y,Tc_z,Fc_x,Fc_y,Fc_z
    DOUBLE PRECISION, DIMENSION(3) :: h_app
    DOUBLE PRECISION, PARAMETER :: PI=3.14159265358979323846264D0
    DOUBLE PRECISION :: CPdma_x,CPdma_y,CPdma_z,CPdmb_x,CPdmb_y,CPdmb_z
    DOUBLE PRECISION :: L,drcn,W_fnc,Vk,Cw,dx,dy,dz
    DOUBLE PRECISION :: dtm,nDOTrli,tlrc_a,tlrc_b,N_ki,nrm
    INTEGER :: Nc_tot,k,sgm_f,sgm_i,w_swtch,itr
```

```fortran
      INTEGER :: count,f_count,Fc_count,dnc_count,h,i,j,ll,f,g,n,m
      CHARACTER(LEN=2) :: sgm_c
!-----------------------------------------------------------------------------------

      Nc_tot=Nc+Nca
      sgm_i=130
      DO i = 1,Nc_tot
         sgm_f=sgm_i+i*10
         WRITE(sgm_c,'(i2)') i
         OPEN (unit=sgm_f,file='C/Sig'//sgm_c//'_chck.txt',action="write",position="append")
      END DO
      OPEN (unit=109,file='C/Mnt_x.txt',action="write",position="append")
      OPEN (unit=110,file='C/Mnt_y.txt',action="write",position="append")
      OPEN (unit=111,file='C/Mnt_z.txt',action="write",position="append")
      OPEN (unit=112,file='C/Hnt_x.txt',action="write",position="append")
      OPEN (unit=113,file='C/Hnt_y.txt',action="write",position="append")
      OPEN (unit=114,file='C/Hnt_z.txt',action="write",position="append")
      OPEN (unit=115,file='C/Hdl_x.txt',action="write",position="append")
      OPEN (unit=116,file='C/Hdl_y.txt',action="write",position="append")
      OPEN (unit=117,file='C/Hdl_z.txt',action="write",position="append")
      OPEN (unit=118,file='C/Sigs.txt',action="write",position="append")
      OPEN (unit=119,file='Sgms_alt.txt',action="write",position="append")
      Vk=(4.0D0/3.0D0)*PI*drcn*drcn*drcn
      Cw=5.0D0
      DO i=0,N1-1
         Cff(i)=1.0D0
         rct_x(i)=rc_x(i)
         rct_y(i)=rc_y(i)
         rct_z(i)=rc_z(i)
         nct_x(i)=nc_x(i)
         nct_y(i)=nc_y(i)
         nct_z(i)=nc_z(i)
      END DO
      Fc_count=0
 61   CONTINUE
      drs_x=0.0D0
      drs_y=0.0D0
      drs_z=0.0D0
      dns_x=0.0D0
      dns_y=0.0D0
      dns_z=0.0D0
      DO f=1,Nc
         DO j = 1,Ns_int*Ncs
```

```
          IF (w_swtch==1 .AND. ABS(rcnv_y(j+(f-1)*Ns_int*Ncs))>=L/2.0D0-0.1D0) THEN
              Vk=0.5D0*(4.0D0/3.0D0)*PI*drcn*drcn*drcn
          ELSE
              Vk=(4.0D0/3.0D0)*PI*drcn*drcn*drcn
          END IF


!Constraint derivatives are calculated
          DO i = 0,N1-1
              dx = rs_x(i) - rcnv_x(j+(f-1)*Ns_int*Ncs)
              dy = rs_y(i) - rcnv_y(j+(f-1)*Ns_int*Ncs)
              dz = rs_z(i) - rcnv_z(j+(f-1)*Ns_int*Ncs)
              CALL PBC_CHCK(dx,dy,dz,L,N_ki,w_swtch)
              IF (N_ki <= drcn) THEN
                  drs_x(i,f) = drs_x(i,f) + Cff(i)*(Cw/Vk)*((ncnv_x(j+(f-1)*Ns_int*Ncs) &
                                  *6.0D0 / (drcn**3)) * ns_x(i) * dx * (N_ki - drcn)) &
                              + Cff(i)*(Cw/Vk)*((ncnv_y(j+(f-1)*Ns_int*Ncs) &
                                  *6.0D0 / (drcn**3)) * ns_y(i) * dx * (N_ki - drcn)) &
                              + Cff(i)*(Cw/Vk)*((ncnv_z(j+(f-1)*Ns_int*Ncs) &
                                  *6.0D0 / (drcn**3)) * ns_z(i) * dx * (N_ki - drcn))
                  drs_y(i,f) = drs_y(i,f) + Cff(i)*(Cw/Vk)*((ncnv_x(j+(f-1)*Ns_int*Ncs) &
                                  *6.0D0 / (drcn**3)) * ns_x(i) * dy * (N_ki - drcn)) &
                              + Cff(i)*(Cw/Vk)*((ncnv_y(j+(f-1)*Ns_int*Ncs) &
                                  *6.0D0 / (drcn**3)) * ns_y(i) * dy *(N_ki - drcn)) &
                              + Cff(i)*(Cw/Vk)*((ncnv_z(j+(f-1)*Ns_int*Ncs) &
                                  *6.0D0 / (drcn**3)) * ns_z(i) * dy * (N_ki - drcn))
                  drs_z(i,f) = drs_z(i,f) + Cff(i)*(Cw/Vk)*((ncnv_x(j+(f-1)*Ns_int*Ncs) &
                                  *6.0D0 / (drcn**3)) * ns_x(i) * dz * (N_ki - drcn)) &
                              + Cff(i)*(Cw/Vk)*((ncnv_y(j+(f-1)*Ns_int*Ncs) &
                                  *6.0D0 / (drcn**3)) * ns_y(i) * dz * (N_ki - drcn)) &
                              + Cff(i)*(Cw/Vk)*((ncnv_z(j+(f-1)*Ns_int*Ncs) &
                                  *6.0D0 / (drcn**3)) * ns_z(i) * dz * (N_ki - drcn))
                  dns_x(i,f) = dns_x(i,f) + Cff(i)*(Cw/Vk) *(ncnv_x(j+(f-1)*Ns_int*Ncs) &
                                  *W_fnc(N_ki,drcn))
                  dns_y(i,f) = dns_y(i,f) + Cff(i)*(Cw/Vk)*(ncnv_y(j+(f-1)*Ns_int*Ncs) &
                                  *W_fnc(N_ki,drcn))
                  dns_z(i,f) = dns_z(i,f) + Cff(i)*(Cw/Vk)*(ncnv_z(j+(f-1)*Ns_int*Ncs) &
                                  *W_fnc(N_ki,drcn))
                  nDOTrli = ns_x(i)*dx+ns_y(i)*dy+ns_z(i)*dz
                  drs_x(i,f) = drs_x(i,f) &
    +    Cff(i)*(ncnv_x(j+(f-1)*Ns_int*Ncs)/(4.0D0*PI*N_ki**5)) * (3.0D0*(nDOTrli &
         *ns_x(i)*dx)-(15.0D0/N_ki**2)*nDOTrli*dx*dx+3.0D0*dx*ns_x(i)) &
    +    Cff(i)*(ncnv_y(j+(f-1)*Ns_int*Ncs)/(4.0D0*PI*N_ki**5)) * (3.0D0 &
         *ns_x(i)*dy-(15.0D0/N_ki**2)*nDOTrli*dx*dy+3.0D0*dx*ns_y(i)) &
    +    Cff(i)*(ncnv_z(j+(f-1)*Ns_int*Ncs)/(4.0D0*PI*N_ki**5)) * (3.0D0 &
         *ns_x(i)*dz-(15.0D0/N_ki**2)*nDOTrli*dx*dz+3.0D0*dx*ns_z(i))
```

```
                    drs_y(i,f) = drs_y(i,f) &
+    Cff(i)*(ncnv_x(j+(f-1)*Ns_int*Ncs)/(4.0D0*PI*N_ki**5)) * (3.0D0 &
       *ns_y(i)*dx-(15.0D0/N_ki**2)*nDOTrli*dy*dx+3.0D0*dy*ns_x(i)) &
+    Cff(i)*(ncnv_y(j+(f-1)*Ns_int*Ncs)/(4.0D0*PI*N_ki**5)) * (3.0D0*(nDOTrli &
       +ns_y(i)*dy)-(15.0D0/N_ki**2)*nDOTrli*dy*dy+3.0D0*dy*ns_y(i)) &
+    Cff(i)*(ncnv_z(j+(f-1)*Ns_int*Ncs)/(4.0D0*PI*N_ki**5)) * (3.0D0 &
       *ns_y(i)*dz-(15.0D0/N_ki**2)*nDOTrli*dy*dz+3.0D0*dy*ns_z(i))
                    drs_z(i,f) = drs_z(i,f) &
+    Cff(i)*(ncnv_x(j+(f-1)*Ns_int*Ncs)/(4.0D0*PI*N_ki**5)) * (3.0D0 &
       *ns_z(i)*dx-(15.0D0/N_ki**2)*nDOTrli*dz*dx+3.0D0*dz*ns_x(i)) &
+    Cff(i)*(ncnv_y(j+(f-1)*Ns_int*Ncs)/(4.0D0*PI*N_ki**5)) * (3.0D0 &
       *ns_z(i)*dy-(15.0D0/N_ki**2)*nDOTrli*dz*dy+3.0D0*dz*ns_y(i)) &
+    Cff(i)*(ncnv_z(j+(f-1)*Ns_int*Ncs)/(4.0D0*PI*N_ki**5)) * (3.0D0*(nDOTrli &
       +ns_z(i)*dz)-(15.0D0/N_ki**2)*nDOTrli*dz*dz+3.0D0*dz*ns_z(i))
                    dns_x(i,f) = dns_x(i,f) &
+    Cff(i)*(ncnv_x(j+(f-1)*Ns_int*Ncs)/(4.0D0*PI*N_ki**3)) * (3.0D0 &
       *dx/(N_ki*N_ki)*dx-1.0D0) &
+    Cff(i)*(ncnv_y(j+(f-1)*Ns_int*Ncs)/(4.0D0*PI*N_ki**3)) * (3.0D0 &
       *dx/(N_ki*N_ki)*dy) &
+    Cff(i)*(ncnv_z(j+(f-1)*Ns_int*Ncs)/(4.0D0*PI*N_ki**3)) * (3.0D0 &
       *dx/(N_ki*N_ki)*dz)
                    dns_y(i,f) = dns_y(i,f) &
+    Cff(i)*(ncnv_x(j+(f-1)*Ns_int*Ncs)/(4.0D0*PI*N_ki**3)) * (3.0D0 &
       *dy/(N_ki*N_ki)*dx) &
+    Cff(i)*(ncnv_y(j+(f-1)*Ns_int*Ncs)/(4.0D0*PI*N_ki**3)) * (3.0D0 &
       *dy/(N_ki*N_ki)*dy-1.0D0) &
+    Cff(i)*(ncnv_z(j+(f-1)*Ns_int*Ncs)/(4.0D0*PI*N_ki**3)) * (3.0D0 &
       *dy/(N_ki*N_ki)*dz)
                    dns_z(i,f) = dns_z(i,f) &
+    Cff(i)*(ncnv_x(j+(f-1)*Ns_int*Ncs)/(4.0D0*PI*N_ki**3)) * (3.0D0 &
       *dz/(N_ki*N_ki)*dx) &
+    Cff(i)*(ncnv_y(j+(f-1)*Ns_int*Ncs)/(4.0D0*PI*N_ki**3)) * (3.0D0 &
       *dz/(N_ki*N_ki)*dy) &
+    Cff(i)*(ncnv_z(j+(f-1)*Ns_int*Ncs)/(4.0D0*PI*N_ki**3)) * (3.0D0 &
       *dz/(N_ki*N_ki)*dz-1.0D0)
                END IF
              END DO
            END DO
          END DO
          DO f = Nc+1,Nc_tot
            DO h = 1,Ncnl4*Nsl
              DO i = 0,N1-1
                dx = rs_x(i) - rcnl_x(h+(f-Nc-1)*Ncnl4*Nsl)
                dy = rs_y(i) - rcnl_y(h+(f-Nc-1)*Ncnl4*Nsl)
                dz = rs_z(i) - rcnl_z(h+(f-Nc-1)*Ncnl4*Nsl)
                N_ki=SQRT((dx*dx) + (dy*dy) + (dz*dz))
```

```fortran
            IF (N_ki <= drcn) THEN
                nDOTrli = ns_x(i)*dx+ns_y(i)*dy+ns_z(i)*dz
                drs_x(i,f) = drs_x(i,f) &
+ Cff(i)*(ncnl_x(h+(f-Nc-1)*Ncnl4*Nsl)/(4.0D0*PI*N_ki**5)) * (3.0D0 *(nDOTrli*ns_x(i) &
        *dx)-(15.0D0/N_ki**2)*nDOTrli*dx*dx+3.0D0*dx*ns_x(i)) &
+ Cff(i)*(ncnl_y(h+(f-Nc-1)*Ncnl4*Nsl)/(4.0D0*PI*N_ki**5)) * (3.0D0*ns_x(i) &
        *dy-(15.0D0/N_ki**2)*nDOTrli*dx*dy+3.0D0*dx*ns_y(i)) &
+ Cff(i)*(ncnl_z(h+(f-Nc-1)*Ncnl4*Nsl)/(4.0D0*PI*N_ki**5)) * (3.0D0*ns_x(i) &
        *dz-(15.0D0/N_ki**2)*nDOTrli*dx*dz+3.0D0*dx*ns_z(i))
                drs_y(i,f) = drs_y(i,f) &
+ Cff(i)*(ncnl_x(h+(f-Nc-1)*Ncnl4*Nsl)/(4.0D0*PI*N_ki**5)) * (3.0D0*ns_y(i) &
        *dx-(15.0D0/N_ki**2)*nDOTrli*dy*dx+3.0D0*dy*ns_x(i)) &
+ Cff(i)*(ncnl_y(h+(f-Nc-1)*Ncnl4*Nsl)/(4.0D0*PI*N_ki**5)) * (3.0D0*(nDOTrli+ns_y(i) &
        *dy)-(15.0D0/N_ki**2)*nDOTrli*dy*dy+3.0D0*dy*ns_y(i)) &
+ Cff(i)*(ncnl_z(h+(f-Nc-1)*Ncnl4*Nsl)/(4.0D0*PI*N_ki**5)) * (3.0D0*ns_y(i) &
        *dz-(15.0D0/N_ki**2)*nDOTrli*dy*dz+3.0D0*dy*ns_z(i))
                drs_z(i,f) = drs_z(i,f) &
+ Cff(i)*(ncnl_x(h+(f-Nc-1)*Ncnl4*Nsl)/(4.0D0*PI*N_ki**5)) * (3.0D0*ns_z(i) &
        *dx-(15.0D0/N_ki**2)*nDOTrli*dz*dx+3.0D0*dz*ns_x(i)) &
+ Cff(i)*(ncnl_y(h+(f-Nc-1)*Ncnl4*Nsl)/(4.0D0*PI*N_ki**5)) * (3.0D0*ns_z(i) &
        *dy-(15.0D0/N_ki**2)*nDOTrli*dz*dy+3.0D0*dz*ns_y(i)) &
+ Cff(i)*(ncnl_z(h+(f-Nc-1)*Ncnl4*Nsl)/(4.0D0*PI*N_ki**5)) * (3.0D0*(nDOTrli+ns_z(i) &
        *dz)-(15.0D0/N_ki**2)*nDOTrli*dz*dz+3.0D0*dz*ns_z(i))
                dns_x(i,f) = dns_x(i,f) &
+ Cff(i)*(ncnl_x(h+(f-Nc-1)*Ncnl4*Nsl)/(4.0D0*PI*N_ki**3)) * (3.0D0 &
        *dx/(N_ki*N_ki)*dx-1.0D0) &
+ Cff(i)*(ncnl_y(h+(f-Nc-1)*Ncnl4*Nsl)/(4.0D0*PI*N_ki**3)) * (3.0D0 &
        *dx/(N_ki*N_ki)*dy) &
+ Cff(i)*(ncnl_z(h+(f-Nc-1)*Ncnl4*Nsl)/(4.0D0*PI*N_ki**3)) * (3.0D0 &
        *dx/(N_ki*N_ki)*dz)
                dns_y(i,f) = dns_y(i,f) &
+ Cff(i)*(ncnl_x(h+(f-Nc-1)*Ncnl4*Nsl)/(4.0D0*PI*N_ki**3)) * (3.0D0 &
        *dy/(N_ki*N_ki)*dx) &
+ Cff(i)*(ncnl_y(h+(f-Nc-1)*Ncnl4*Nsl)/(4.0D0*PI*N_ki**3)) * (3.0D0 &
        *dy/(N_ki*N_ki)*dy-1.0D0) &
+ Cff(i)*(ncnl_z(h+(f-Nc-1)*Ncnl4*Nsl)/(4.0D0*PI*N_ki**3)) * (3.0D0 &
        *dy/(N_ki*N_ki)*dz)
                dns_z(i,f) = dns_z(i,f) &
+ Cff(i)*(ncnl_x(h+(f-Nc-1)*Ncnl4*Nsl)/(4.0D0*PI*N_ki**3)) * (3.0D0 &
        *dz/(N_ki*N_ki)*dx) &
+ Cff(i)*(ncnl_y(h+(f-Nc-1)*Ncnl4*Nsl)/(4.0D0*PI*N_ki**3)) * (3.0D0 &
        *dz/(N_ki*N_ki)*dy) &
+ Cff(i)*(ncnl_z(h+(f-Nc-1)*Ncnl4*Nsl)/(4.0D0*PI*N_ki**3)) * (3.0D0 &
        *dz/(N_ki*N_ki)*dz-1.0D0)
            END IF
```

```
            END DO
         END DO
      END DO
      Lmbd = 0.0D0
      DO itr=1,100
         M_x=0.0D0
         M_y=0.0D0
         M_z=0.0D0
         Md_x=0.0D0
         Md_y=0.0D0
         Md_z=0.0D0
         Mda_x=0.0D0
         Mda_y=0.0D0
         Mda_z=0.0D0

!Fields at nodes are found by sliding weight function
         DO j = 1,Ns_int*Ncs*Nc
            IF (w_swtch == 1 .AND. ABS(rcnv_y(j)) >= L/2.0D0-0.1D0) THEN
               Vk=0.5D0*(4.0D0/3.0D0)*PI*drcn*drcn*drcn
            ELSE
               Vk=(4.0D0/3.0D0)*PI*drcn*drcn*drcn
            END IF
            DO i = 0,N1-1
               dx = rc_x(i) - rcnv_x(j)
               dy = rc_y(i) - rcnv_y(j)
               dz = rc_z(i) - rcnv_z(j)
               CALL PBC_CHCK(dx,dy,dz,L,N_ki,w_swtch)
               IF (N_ki <= drcn) THEN
                  M_x(j) = M_x(j) + Cff(i)*(Cw/Vk) *nc_x(i) * W_fnc(N_ki,drcn)
                  M_y(j) = M_y(j) + Cff(i)*(Cw/Vk) *nc_y(i) * W_fnc(N_ki,drcn)
                  M_z(j) = M_z(j) + Cff(i)*(Cw/Vk) *nc_z(i) * W_fnc(N_ki,drcn)
                  nDOTrli=nc_x(i)*dx+nc_y(i)*dy+nc_z(i)*dz
                  Md_x(j) = Md_x(j) + Cff(i)*(1.0D0/(4.0D0*PI*N_ki**3)) &
                                   * (3.0D0*nDOTrli*dx/(N_ki*N_ki) - nc_x(i))
                  Md_y(j) = Md_y(j) + Cff(i)*(1.0D0/(4.0D0*PI*N_ki**3)) &
                                   * (3.0D0*nDOTrli*dy/(N_ki*N_ki) - nc_y(i))
                  Md_z(j) = Md_z(j) + Cff(i)*(1.0D0/(4.0D0*PI*N_ki**3)) &
                                   * (3.0D0*nDOTrli*dz/(N_ki*N_ki) - nc_z(i))
               END IF
            END DO
         END DO
         DO h = 1,Ncnl4*Nsl*Nca
            DO i = 0,N1-1
               dx = rc_x(i) - rcnl_x(h)
               dy = rc_y(i) - rcnl_y(h)
               dz = rc_z(i) - rcnl_z(h)
```

```
                N_ki=SQRT((dx*dx) + (dy*dy) + (dz*dz))
                IF (N_ki <= drcn) THEN
                    nDOTrli=nc_x(i)*dx+nc_y(i)*dy+nc_z(i)*dz
                    Mda_x(h)=Mda_x(h) + (1.0D0/(4.0D0*PI*N_ki**3)) &
                                    * (3.0D0*nDOTrli*dx/(N_ki*N_ki) - nc_x(i))
                    Mda_y(h)=Mda_y(h) + (1.0D0/(4.0D0*PI*N_ki**3)) &
                                    * (3.0D0*nDOTrli*dy/(N_ki*N_ki) - nc_y(i))
                    Mda_z(h)=Mda_z(h) + (1.0D0/(4.0D0*PI*N_ki**3)) &
                                    * (3.0D0*nDOTrli*dz/(N_ki*N_ki) - nc_z(i))
                END IF
            END DO
        END DO

!Maxwell's equations are calculated
        Mnt_y=0.0D0
        Mnt_x=0.0D0
        Mnt_z=0.0D0
        Hnt_y=0.0D0
        Hnt_x=0.0D0
        Hnt_z=0.0D0
        DO f=1,Nc
            DO m=1,2
                DO j=1,Ns_int
                    Mnt_x(2*f+m-2) = Mnt_x(2*f+m-2) &
                        + ncnv_x(j+(Ncs*(f-1)+m+1)*Ns_int)*M_x(j+(Ncs*(f-1)+m+1)*Ns_int)
                    Mnt_y(2*f+m-2) = Mnt_y(2*f+m-2) &
                        + ncnv_y(j+(Ncs*(f-1)+m-1)*Ns_int)*M_y(j+(Ncs*(f-1)+m-1)*Ns_int)
                    Hnt_x(2*f+m-2) = Hnt_x(2*f+m-2) &
                        + ncnv_x(j+(Ncs*(f-1)+m+1)*Ns_int)*Md_x(j+(Ncs*(f-1)+m+1)*Ns_int)
                    Hnt_y(2*f+m-2) = Hnt_y(2*f+m-2) &
                        + ncnv_y(j+(Ncs*(f-1)+m-1)*Ns_int)*Md_y(j+(Ncs*(f-1)+m-1)*Ns_int)
                END DO
            END DO
        END DO
        DO f=1,Nc*Ncs
            DO j=1,Ns_int
                Mnt_x(f) = Mnt_x(f) + ncnv_x(j+(f-1)*Ns_int)*M_x(j+(f-1)*Ns_int)
                Mnt_y(f) = Mnt_y(f) + ncnv_y(j+(f-1)*Ns_int)*M_y(j+(f-1)*Ns_int)
                Hnt_x(f) = Hnt_x(f) + ncnv_x(j+(f-1)*Ns_int)*Md_x(j+(f-1)*Ns_int)
                Hnt_y(f) = Hnt_y(f) + ncnv_y(j+(f-1)*Ns_int)*Md_y(j+(f-1)*Ns_int)
            END DO
        END DO
        DO f=1,Nc
            DO m=1,2
```

```fortran
        DO j=1,Ns_int
            Mnt_z(2*f+m-2) = Mnt_z(2*f+m-2) &
                + ncnv_z(j+(Ncs*(f-1)+m+3)*Ns_int)*M_z(j+(Ncs*(f-1)+m+3)*Ns_int)
            Hnt_z(2*f+m-2) = Hnt_z(2*f+m-2) &
                + ncnv_z(j+(Ncs*(f-1)+m+3)*Ns_int)*Md_z(j+(Ncs*(f-1)+m+3)*Ns_int)
        END DO
    END DO
END DO
Hdl_x =0.0D0
Hdl_y=0.0D0
Hdl_z=0.0D0
Hdlt_x =0.0D0
Hdlt_y =0.0D0
Hdlt_z =0.0D0
DO g=1,Nca
    DO h = (g-1)*Ncnl4*Nsl+1,g*Ncnl4*Nsl
        Hdl_x(g)= Hdl_x(g)+ncnl_x(h)*Mda_x(h)
        Hdl_y(g)= Hdl_y(g)+ncnl_y(h)*Mda_y(h)
        Hdl_z(g)= Hdl_z(g)+ncnl_z(h)*Mda_z(h)
    END DO
END DO
DO g=1,Nca *4
    DO h = (g-1)*Ncnl+1,g*Ncnl
        Hdlt_x(g)= Hdlt_x(g)+ncnl_x(h)*Mda_x(h)
        Hdlt_y(g)= Hdlt_y(g)+ncnl_y(h)*Mda_y(h)
        Hdlt_z(g)= Hdlt_z(g)+ncnl_z(h)*Mda_z(h)
    END DO
END DO


!Iterative constraint scheme is applied via Lagrange multiplier method
    sgm=0.0D0
    sgm_t=0.0D0
    DO f=1,Nc
        sgm(f) = sgm(f) + Mnt_x(f*2-1) + Mnt_x(f*2) + Hnt_x(f*2-1) + Hnt_x(f*2) &
                        + Mnt_y(f*2-1) + Mnt_y(f*2) + Hnt_y(f*2-1) + Hnt_y(f*2) &
                        + Mnt_z(f*2-1) + Mnt_z(f*2) + Hnt_z(f*2-1) + Hnt_z(f*2)
    END DO
    DO g=Nc+1,Nc_tot
        sgm(g) = sgm(g) + Hdl_x(g-Nc) + Hdl_y(g-Nc) + Hdl_z(g-Nc)
        DO h=1,4
            sgm_t(g) = sgm_t(g) + Hdlt_x(h+4*(g-Nc-1)) + Hdlt_y(h+4*(g-Nc-1)) &
                              + Hdlt_z(h+4*(g-Nc-1))
        END DO
    END DO
    f_count=Nc_tot
```

```
DO f=1,Nc_tot
    sgm_f=sgm_i+f*10
    IF (ABS(sgm(f)) < tlrc_a) THEN
        f_count=f_count-1
    END IF
END DO
IF (f_count == 0) THEN
    DO f=1,Nc_tot
        sgm_f=sgm_i+f*10
        WRITE(sgm_f,37) 'Sig = ',sgm(f),',Lmbd=',Lmbd(f),' @ itr = ',itr,', &
                            time_step(k) = ',k,' *done'
    END DO
    WRITE(109,’(a11,i6,i5,60(f19.10))’) 'done ',k,itr,Mnt_x
    WRITE(110,’(a11,i6,i5,60(f19.10))’) 'done ',k,itr,Mnt_y
    WRITE(111,’(a11,i6,i5,60(f19.10))’) 'done ',k,itr,Mnt_z
    WRITE(112,’(a11,i6,i5,60(f19.10))’) 'done ',k,itr,Hnt_x
    WRITE(113,’(a11,i6,i5,60(f19.10))’) 'done ',k,itr,Hnt_y
    WRITE(114,’(a11,i6,i5,60(f19.10))’) 'done ',k,itr,Hnt_z
    WRITE(115,’(a11,i6,i5,60(f19.10))’) 'done ',k,itr,Hdl_x
    WRITE(116,’(a11,i6,i5,60(f19.10))’) 'done ',k,itr,Hdl_y
    WRITE(117,’(a11,i6,i5,60(f19.10))’) 'done ',k,itr,Hdl_z
    WRITE(118,’(a11,i6,i5,60(f19.10))’) 'done ',k,itr,sgm
    WRITE(119,’(a11,i6,i5,60(f19.10))’) 'done ',k,itr,sgm
    GO TO 62
END IF
drc_x=0.0D0
drc_y=0.0D0
drc_z=0.0D0
dnc_x=0.0D0
dnc_y=0.0D0
dnc_z=0.0D0
DO f=1,Nc
    DO j = 1,Ns_int*Ncs
        IF (w_swtch == 1 .AND. ABS(rcnv_y(j+(f-1)*Ns_int*Ncs)) &
                                    >= L/2.0D0-0.1D0) THEN
            Vk=0.5D0*(4.0D0/3.0D0)*PI*drcn*drcn*drcn
        ELSE
            Vk=(4.0D0/3.0D0)*PI*drcn*drcn*drcn
        END IF
        DO i = 0,N1-1
            dx = rc_x(i) - rcnv_x(j+(f-1)*Ns_int*Ncs)
            dy = rc_y(i) - rcnv_y(j+(f-1)*Ns_int*Ncs)
            dz = rc_z(i) - rcnv_z(j+(f-1)*Ns_int*Ncs)
            CALL PBC_CHCK(dx,dy,dz,L,N_ki,w_swtch)
            IF (N_ki <= drcn) THEN
```

```
                    drc_x(i,f) = drc_x(i,f) &
+ Cff(i)*(Cw/Vk) *((ncnv_x(j+(f-1)*Ns_int*Ncs)*6.0D0 / (drcn**3)) * nc_x(i) &
        * dx * (N_ki - drcn)) &
+ Cff(i)*(Cw/Vk)*((ncnv_y(j+(f-1)*Ns_int*Ncs)*6.0D0 / (drcn**3)) * nc_y(i) &
        * dx * (N_ki - drcn)) &
+ Cff(i)*(Cw/Vk)*((ncnv_z(j+(f-1)*Ns_int*Ncs)*6.0D0 / (drcn**3)) * nc_z(i) &
        * dx * (N_ki - drcn))
                    drc_y(i,f) = drc_y(i,f) &
+ Cff(i)*(Cw/Vk)*((ncnv_x(j+(f-1)*Ns_int*Ncs)*6.0D0 / (drcn**3)) * nc_x(i) &
        * dy * (N_ki - drcn)) &
+ Cff(i)*(Cw/Vk)*((ncnv_y(j+(f-1)*Ns_int*Ncs)*6.0D0 / (drcn**3)) * nc_y(i) &
        * dy * (N_ki - drcn)) &
+ Cff(i)*(Cw/Vk)*((ncnv_z(j+(f-1)*Ns_int*Ncs)*6.0D0 / (drcn**3)) * nc_z(i) &
        * dy * (N_ki - drcn))
                    drc_z(i,f) = drc_z(i,f) &
+ Cff(i)*(Cw/Vk)*((ncnv_x(j+(f-1)*Ns_int*Ncs)*6.0D0 / (drcn**3)) * nc_x(i) &
        * dz * (N_ki - drcn)) &
+ Cff(i)*(Cw/Vk)*((ncnv_y(j+(f-1)*Ns_int*Ncs)*6.0D0 / (drcn**3)) * nc_y(i) &
        * dz * (N_ki - drcn)) &
+ Cff(i)*(Cw/Vk)*((ncnv_z(j+(f-1)*Ns_int*Ncs)*6.0D0 / (drcn**3)) * nc_z(i) &
        * dz * (N_ki - drcn))
                    dnc_x(i,f) = dnc_x(i,f) &
                        + Cff(i)*(Cw/Vk)*(ncnv_x(j+(f-1)*Ns_int*Ncs)*W_fnc(N_ki,drcn))
                    dnc_y(i,f) = dnc_y(i,f) &
                        + Cff(i)*(Cw/Vk)*(ncnv_y(j+(f-1)*Ns_int*Ncs)*W_fnc(N_ki,drcn))
                    dnc_z(i,f) = dnc_z(i,f) &
                        + Cff(i)*(Cw/Vk)*(ncnv_z(j+(f-1)*Ns_int*Ncs)*W_fnc(N_ki,drcn))
                    nDOTrli=nc_x(i)*dx+nc_y(i)*dy+nc_z(i)*dz
                    drc_x(i,f) = drc_x(i,f) &
+ Cff(i)*(ncnv_x(j+(f-1)*Ns_int*Ncs)/(4.0D0*PI*N_ki**5)) * (3.0D0*(nDOTrli*nc_x(i) &
        *dx)-(15.0D0/N_ki**2)*nDOTrli*dx*dx+3.0D0*dx*nc_x(i)) &
+ Cff(i)*(ncnv_y(j+(f-1)*Ns_int*Ncs)/(4.0D0*PI*N_ki**5)) * (3.0D0*nc_x(i) &
        *dy-(15.0D0/N_ki**2)*nDOTrli*dx*dy+3.0D0*dx*nc_y(i)) &
+ Cff(i)*(ncnv_z(j+(f-1)*Ns_int*Ncs)/(4.0D0*PI*N_ki**5)) * (3.0D0*nc_x(i) &
        *dz-(15.0D0/N_ki**2)*nDOTrli*dx*dz+3.0D0*dx*nc_z(i))
                    drc_y(i,f) = drc_y(i,f) &
+ Cff(i)*(ncnv_x(j+(f-1)*Ns_int*Ncs)/(4.0D0*PI*N_ki**5)) * (3.0D0*nc_y(i) &
        *dx-(15.0D0/N_ki**2)*nDOTrli*dy*dx+3.0D0*dy*nc_x(i)) &
+ Cff(i)*(ncnv_y(j+(f-1)*Ns_int*Ncs)/(4.0D0*PI*N_ki**5)) * (3.0D0*(nDOTrli+nc_y(i) &
        *dy)-(15.0D0/N_ki**2)*nDOTrli*dy*dy+3.0D0*dy*nc_y(i)) &
+ Cff(i)*(ncnv_z(j+(f-1)*Ns_int*Ncs)/(4.0D0*PI*N_ki**5)) * (3.0D0*nc_y(i) &
        *dz-(15.0D0/N_ki**2)*nDOTrli*dy*dz+3.0D0*dy*nc_z(i))
```

```
                    drc_z(i,f) = drc_z(i,f) &
+ Cff(i)*(ncnv_x(j+(f-1)*Ns_int*Ncs)/(4.0D0*PI*N_ki**5)) * (3.0D0*nc_z(i) &
        *dx-(15.0D0/N_ki**2)*nDOTrli*dz*dx+3.0D0*dz*nc_x(i)) &
+ Cff(i)*(ncnv_y(j+(f-1)*Ns_int*Ncs)/(4.0D0*PI*N_ki**5)) * (3.0D0*nc_z(i) &
        *dy-(15.0D0/N_ki**2)*nDOTrli*dz*dy+3.0D0*dz*nc_y(i)) &
+ Cff(i)*(ncnv_z(j+(f-1)*Ns_int*Ncs)/(4.0D0*PI*N_ki**5)) * (3.0D0*(nDOTrli+nc_z(i) &
        *dz)-(15.0D0/N_ki**2)*nDOTrli*dz*dz+3.0D0*dz*nc_z(i))
                    dnc_x(i,f) = dnc_x(i,f) &
                        + Cff(i)*(ncnv_x(j+(f-1)*Ns_int*Ncs)/(4.0D0*PI*N_ki**3)) &
                            * (3.0D0*dx/(N_ki*N_ki)*dx-1.0D0)
                        + Cff(i)*(ncnv_y(j+(f-1)*Ns_int*Ncs)/(4.0D0*PI*N_ki**3)) &
                            * (3.0D0*dx/(N_ki*N_ki)*dy) &
                        + Cff(i)*(ncnv_z(j+(f-1)*Ns_int*Ncs)/(4.0D0*PI*N_ki**3)) &
                            * (3.0D0*dx/(N_ki*N_ki)*dz)
                    dnc_y(i,f) = dnc_y(i,f) &
                        + Cff(i)*(ncnv_x(j+(f-1)*Ns_int*Ncs)/(4.0D0*PI*N_ki**3)) &
                            * (3.0D0*dy/(N_ki*N_ki)*dx) &
                        + Cff(i)*(ncnv_y(j+(f-1)*Ns_int*Ncs)/(4.0D0*PI*N_ki**3)) &
                            * (3.0D0*dy/(N_ki*N_ki)*dy-1.0D0) &
                        + Cff(i)*(ncnv_z(j+(f-1)*Ns_int*Ncs)/(4.0D0*PI*N_ki**3)) &
                            * (3.0D0*dy/(N_ki*N_ki)*dz)
                    dnc_z(i,f) = dnc_z(i,f) &
                        + Cff(i)*(ncnv_x(j+(f-1)*Ns_int*Ncs)/(4.0D0*PI*N_ki**3)) &
                            * (3.0D0*dz/(N_ki*N_ki)*dx) &
                        + Cff(i)*(ncnv_y(j+(f-1)*Ns_int*Ncs)/(4.0D0*PI*N_ki**3)) &
                            * (3.0D0*dz/(N_ki*N_ki)*dy) &
                        + Cff(i)*(ncnv_z(j+(f-1)*Ns_int*Ncs)/(4.0D0*PI*N_ki**3)) &
                            * (3.0D0*dz/(N_ki*N_ki)*dz-1.0D0)
                END IF
            END DO
        END DO
    END DO
    DO f = Nc+1,Nc_tot
        DO h = 1,Ncnl4*Nsl
            DO i = 0,N1-1
                dx = rc_x(i) - rcnl_x(h+(f-Nc-1)*Ncnl4*Nsl)
                dy = rc_y(i) - rcnl_y(h+(f-Nc-1)*Ncnl4*Nsl)
                dz = rc_z(i) - rcnl_z(h+(f-Nc-1)*Ncnl4*Nsl)
                N_ki=SQRT((dx*dx) + (dy*dy) + (dz*dz))
                IF (N_ki <= drcn) THEN
                    nDOTrli = nc_x(i)*dx+nc_y(i)*dy+nc_z(i)*dz
```

```
                    drc_x(i,f) = drc_x(i,f) &
 + Cff(i)*(ncnl_x(h+(f-Nc-1)*Ncnl4*Nsl)/(4.0D0*PI*N_ki**5)) * (3.0D0*(nDOTrli*nc_x(i) &
        *dx)-(15.0D0/N_ki**2)*nDOTrli*dx*dx+3.0D0*dx*nc_x(i)) &
 + Cff(i)*(ncnl_y(h+(f-Nc-1)*Ncnl4*Nsl)/(4.0D0*PI*N_ki**5)) * (3.0D0*nc_x(i) &
        *dy-(15.0D0/N_ki**2)*nDOTrli*dx*dy+3.0D0*dx*nc_y(i)) &
 + Cff(i)*(ncnl_z(h+(f-Nc-1)*Ncnl4*Nsl)/(4.0D0*PI*N_ki**5)) * (3.0D0*nc_x(i) &
        *dz-(15.0D0/N_ki**2)*nDOTrli*dx*dz+3.0D0*dx*nc_z(i))
                    drc_y(i,f) = drc_y(i,f) &
 + Cff(i)*(ncnl_x(h+(f-Nc-1)*Ncnl4*Nsl)/(4.0D0*PI*N_ki**5)) * (3.0D0*nc_y(i) &
        *dx-(15.0D0/N_ki**2)*nDOTrli*dy*dx+3.0D0*dy*nc_x(i)) &
 + Cff(i)*(ncnl_y(h+(f-Nc-1)*Ncnl4*Nsl)/(4.0D0*PI*N_ki**5)) * (3.0D0*(nDOTrli+nc_y(i) &
        *dy)-(15.0D0/N_ki**2)*nDOTrli*dy*dy+3.0D0*dy*nc_y(i)) &
 + Cff(i)*(ncnl_z(h+(f-Nc-1)*Ncnl4*Nsl)/(4.0D0*PI*N_ki**5)) * (3.0D0*nc_y(i) &
        *dz-(15.0D0/N_ki**2)*nDOTrli*dy*dz+3.0D0*dy*nc_z(i))
                    drc_z(i,f) = drc_z(i,f) &
 + Cff(i)*(ncnl_x(h+(f-Nc-1)*Ncnl4*Nsl)/(4.0D0*PI*N_ki**5)) * (3.0D0*nc_z(i) &
        *dx-(15.0D0/N_ki**2)*nDOTrli*dz*dx+3.0D0*dz*nc_x(i)) &
 + Cff(i)*(ncnl_y(h+(f-Nc-1)*Ncnl4*Nsl)/(4.0D0*PI*N_ki**5)) * (3.0D0*nc_z(i) &
        *dy-(15.0D0/N_ki**2)*nDOTrli*dz*dy+3.0D0*dz*nc_y(i)) &
 + Cff(i)*(ncnl_z(h+(f-Nc-1)*Ncnl4*Nsl)/(4.0D0*PI*N_ki**5)) * (3.0D0*(nDOTrli+nc_z(i) &
        *dz)-(15.0D0/N_ki**2)*nDOTrli*dz*dz+3.0D0*dz*nc_z(i))
                    dnc_x(i,f) = dnc_x(i,f) &
                        + Cff(i)*(ncnl_x(h+(f-Nc-1)*Ncnl4*Nsl)/(4.0D0*PI*N_ki**3)) &
                            * (3.0D0*dx/(N_ki*N_ki)*dx-1.0D0) &
                        + Cff(i)*(ncnl_y(h+(f-Nc-1)*Ncnl4*Nsl)/(4.0D0*PI*N_ki**3)) &
                            * (3.0D0*dx/(N_ki*N_ki)*dy) &
                        + Cff(i)*(ncnl_z(h+(f-Nc-1)*Ncnl4*Nsl)/(4.0D0*PI*N_ki**3)) &
                            * (3.0D0*dx/(N_ki*N_ki)*dz)
                    dnc_y(i,f) = dnc_y(i,f) &
                        + Cff(i)*(ncnl_x(h+(f-Nc-1)*Ncnl4*Nsl)/(4.0D0*PI*N_ki**3)) &
                            * (3.0D0*dy/(N_ki*N_ki)*dx) &
                        + Cff(i)*(ncnl_y(h+(f-Nc-1)*Ncnl4*Nsl)/(4.0D0*PI*N_ki**3)) &
                            * (3.0D0*dy/(N_ki*N_ki)*dy-1.0D0) &
                        + Cff(i)*(ncnl_z(h+(f-Nc-1)*Ncnl4*Nsl)/(4.0D0*PI*N_ki**3)) &
                            * (3.0D0*dy/(N_ki*N_ki)*dz)
                    dnc_z(i,f) = dnc_z(i,f) &
                        + Cff(i)*(ncnl_x(h+(f-Nc-1)*Ncnl4*Nsl)/(4.0D0*PI*N_ki**3)) &
                                * (3.0D0*dz/(N_ki*N_ki)*dx) &
                        + Cff(i)*(ncnl_y(h+(f-Nc-1)*Ncnl4*Nsl)/(4.0D0*PI*N_ki**3)) &
                            * (3.0D0*dz/(N_ki*N_ki)*dy) &
                        + Cff(i)*(ncnl_z(h+(f-Nc-1)*Ncnl4*Nsl)/(4.0D0*PI*N_ki**3)) &
                            * (3.0D0*dz/(N_ki*N_ki)*dz-1.0D0)
                END IF
              END DO
            END DO
          END DO
```

```fortran
Lmbd = 0.0D0
mod_G  = 0.0D0
DO f=1,Nc_tot
    DO g=1,Nc_tot
        DO i = 0,N1-1
            mod_G(f,g) = mod_G(f,g) &
                    + (drc_x(i,f)*drs_x(i,g) +drc_y(i,f)*drs_y(i,g)+drc_z(i,f)*drs_z(i,g) &
                    + dnc_x(i,f)*dns_x(i,g)+dnc_y(i,f)*dns_y(i,g)+dnc_z(i,f)*dns_z(i,g))
        END DO
    END DO
END DO
mod_Gt=0.0D0
b_arr_tmp=0.0D0
DO i=1,Nc_tot
    b_arr_tmp(i,i)=1.0D0
    DO j=1,Nc_tot
        mod_Gt(i,j)=mod_G(i,j)
    END DO
END DO
DO j=1,Nc_tot
    DO i=1,Nc_tot
        b_arr(i)=b_arr_tmp(i,j)
    END DO
    CALL  RWPVT(Nc_tot,mod_Gt,b_arr,1,x_tmp,dtm,Lmt,U_tmp,c_tmp)
    DO i=1,Nc_tot
        g_arr(i,j)=x_tmp(i)
    END DO
END DO
IF (MOD(itr,10) == 1) THEN
    b_arr_tmp = MATMUL(mod_G,g_arr)
END IF
DO f=1,Nc_tot
    DO g=1,Nc_tot
        Lmbd(f) = Lmbd(f) + g_arr(f,g)* sgm(g)
    END DO
END DO
Fc_x=0.0D0
Fc_y=0.0D0
Fc_z=0.0D0
Tc_x=0.0D0
Tc_y=0.0D0
Tc_z=0.0D0
DO i = 0,N1-1
```

```
      DO f=1,Nc_tot
         Fc_x(i)= Fc_x(i) - Lmbd(f)*drs_x(i,f)
         Fc_y(i)= Fc_y(i) - Lmbd(f)*drs_y(i,f)
         Fc_z(i)= Fc_z(i) - Lmbd(f)*drs_z(i,f)
      END DO
      IF (ABS(rc_x(i)+Fc_x(i))*Cff(i) > L .OR. ABS(rc_y(i)+Fc_y(i))*Cff(i) > L/2.0D0 &
                                     .OR. ABS(rc_z(i)+Fc_z(i))*Cff(i) > L) THEN
         Cff(i)=0.0D0
         Fc_count=Fc_count+1
         IF (Fc_count == 10) THEN
            DO g = 0,N1-1
               rc_x(g)=rct_x(g)
               rc_y(g)=rct_y(g)
               rc_z(g)=rct_z(g)
               nc_x(g)=nct_x(g)
               nc_y(g)=nct_y(g)
               nc_z(g)=nct_z(g)
            END DO
            GO TO 62
         END IF
         GO TO 61
      END IF
   END DO
   Fc_x=0.0D0
   Fc_y=0.0D0
   Fc_z=0.0D0
   Tc_x=0.0D0
   Tc_y=0.0D0
   Tc_z=0.0D0
   DO i = 0,N1-1
      DO f=1,Nc_tot
         Fc_x(i)= Fc_x(i) - Lmbd(f)*drs_x(i,f)
         Fc_y(i)= Fc_y(i) - Lmbd(f)*drs_y(i,f)
         Fc_z(i)= Fc_z(i) - Lmbd(f)*drs_z(i,f)
         Tc_x(i)= Tc_x(i) - Lmbd(f)*dns_x(i,f)
         Tc_y(i)= Tc_y(i) - Lmbd(f)*dns_y(i,f)
         Tc_z(i)= Tc_z(i) - Lmbd(f)*dns_z(i,f)
      END DO
      CPdma_x=ns_y(i)*Tc_z(i) - ns_z(i)*Tc_y(i)
      CPdma_y=ns_z(i)*Tc_x(i) - ns_x(i)*Tc_z(i)
      CPdma_z=ns_x(i)*Tc_y(i) - ns_y(i)*Tc_x(i)
      CPdmb_x=CPdma_y*ns_z(i) - CPdma_z*ns_y(i)
      CPdmb_y=CPdma_z*ns_x(i) - CPdma_x*ns_z(i)
      CPdmb_z=CPdma_x*ns_y(i) - CPdma_y*ns_x(i)
```

```
      nc_x(i) = nc_x(i) + CPdmb_x*(3.0D0/4.0D0)*Cff(i)
      nc_y(i) = nc_y(i) + CPdmb_y*(3.0D0/4.0D0)*Cff(i)
      nc_z(i) = nc_z(i) + CPdmb_z*(3.0D0/4.0D0)*Cff(i)
      nrm = SQRT((nc_x(i)*nc_x(i))+(nc_y(i)*nc_y(i))+(nc_z(i)*nc_z(i)))
      nc_x(i)=nc_x(i)/nrm
      nc_y(i)=nc_y(i)/nrm
      nc_z(i)=nc_z(i)/nrm
      rc_x(i)=rc_x(i) + Fc_x(i)*Cff(i)
      rc_y(i)=rc_y(i) + Fc_y(i)*Cff(i)
      rc_z(i)=rc_z(i) + Fc_z(i)*Cff(i)
      IF (rc_x(i) > L/2.0D0) THEN
          rc_x(i) = rc_x(i) - L
      END IF
      IF (rc_z(i) > L/2.0D0) THEN
          rc_z(i) = rc_z(i) - L
      END IF
      IF (rc_x(i) < -L/2.0D0) THEN
          rc_x(i) = rc_x(i) + L
      END IF
      IF (rc_z(i) < -L/2.0D0) THEN
          rc_z(i) = rc_z(i) + L
      END IF
      IF (rc_y(i) > L/2.0D0 .AND. w_swtch == 0) THEN
          rc_y(i) = rc_y(i) - L
      END IF
      IF (rc_y(i) < -L/2.0D0 .AND. w_swtch == 0) THEN
          rc_y(i) = rc_y(i) + L
      END IF
    END DO
END DO
dnc_count=0
DO f=1,Nc_tot
    sgm_f=sgm_i+f*10
    IF (ABS(sgm(f)) < tlrc_b) THEN
        WRITE(sgm_f,37) 'Sig = ',sgm(f),',Lmbd=',Lmbd(f),' @ itr = ',itr,', &
                          time_step(k) = ',k,' *close'
    ELSE
        WRITE(sgm_f,37) 'Sig = ',sgm(f),',Lmbd=',Lmbd(f),' @ itr = ',itr,', &
                          time_step(k) = ',k,' *dnc'
        dnc_count=dnc_count+1
    END IF
END DO
IF (dnc_count > 0) THEN
```

```
    DO i = 0,N1-1
        rc_x(i)=rct_x(i)
        rc_y(i)=rct_y(i)
        rc_z(i)=rct_z(i)
        nc_x(i)=nct_x(i)
        nc_y(i)=nct_y(i)
        nc_z(i)=nct_z(i)
    END DO
 END IF
 WRITE(109,'(a11,i6,i5,60(f19.10))') 'n/a_f',k,itr,Mnt_x
 WRITE(110,'(a11,i6,i5,60(f19.10))') 'n/a_f',k,itr,Mnt_y
 WRITE(111,'(a11,i6,i5,60(f19.10))') 'n/a_f',k,itr,Mnt_z
 WRITE(112,'(a11,i6,i5,60(f19.10))') 'n/a_f',k,itr,Hnt_x
 WRITE(113,'(a11,i6,i5,60(f19.10))') 'n/a_f',k,itr,Hnt_y
 WRITE(114,'(a11,i6,i5,60(f19.10))') 'n/a_f',k,itr,Hnt_z
 WRITE(115,'(a11,i6,i5,60(f19.10))') 'n/a_f',k,itr,Hdl_x
 WRITE(116,'(a11,i6,i5,60(f19.10))') 'n/a_f',k,itr,Hdl_y
 WRITE(117,'(a11,i6,i5,60(f19.10))') 'n/a_f',k,itr,Hdl_z
 WRITE(118,'(a11,i6,i5,60(f19.10))') 'n/a_f',k,itr,sgm
 WRITE(119,'(a11,i6,i5,60(f19.10))') 'n/a_f',k,itr,sgm
62 CONTINUE
 DO i=N1,N7-1-w_swtch*N1*2
     nc_x(i) = nc_x(i-N1)
     nc_y(i) = nc_y(i-N1)
     nc_z(i) = nc_z(i-N1)
 END DO
 DO i=0,N1-1
     rc_x(i+N1)  = rc_x(i)-L
     rc_x(i+N1*2) = rc_x(i)+L
     rc_x(i+N1*3) = rc_x(i)
     rc_x(i+N1*4) = rc_x(i)
     rc_y(i+N1)  = rc_y(i)
     rc_y(i+N1*2) = rc_y(i)
     rc_y(i+N1*3) = rc_y(i)
     rc_y(i+N1*4) = rc_y(i)
     rc_z(i+N1)  = rc_z(i)
     rc_z(i+N1*2) = rc_z(i)
     rc_z(i+N1*3) = rc_z(i)-L
     rc_z(i+N1*4) = rc_z(i)+L
 END DO
 IF (w_swtch == 0) THEN
```

```fortran
      DO i=0,N1-1
          rc_x(i+N1*5) = rc_x(i)
          rc_x(i+N1*6) = rc_x(i)
          rc_y(i+N1*5) = rc_y(i)-L
          rc_y(i+N1*6) = rc_y(i)+L
          rc_z(i+N1*5) = rc_z(i)
          rc_z(i+N1*6) = rc_z(i)
      END DO
   END IF
   DO f=1,Nc_tot
      sgm_f=sgm_i+f*10
      CLOSE(sgm_f)
   END DO
   DO f=109,119
      CLOSE(f)
   END DO
37 FORMAT(a12,f20.11,a10,e15.7,a8,i3,a17,i5,a13)
   RETURN
END SUBROUTINE M_E_CONST
!###############################################################################
```

Appendix D

Proof of Permission from American Institute of Physics (AIP) Publishing

AIP PUBLISHING LLC LICENSE
TERMS AND CONDITIONS

Nov 28, 2016

This Agreement between Sean Dubina ("You") and AIP Publishing LLC ("AIP Publishing LLC") consists of your license details and the terms and conditions provided by AIP Publishing LLC and Copyright Clearance Center.

License Number	3997850322476
License date	Nov 28, 2016
Licensed Content Publisher	AIP Publishing LLC
Licensed Content Publication	Physics of Fluids
Licensed Content Title	A Brownian dynamics study on ferrofluid colloidal dispersions using an iterative constraint method to satisfy Maxwell's equations
Licensed Content Author	Sean Hyun Dubina,Lewis Edward Wedgewood
Licensed Content Date	Jul 5, 2016
Licensed Content Volume Number	28
Licensed Content Issue Number	7
Type of Use	Thesis/Dissertation
Requestor type	Author (original article)
Format	Print and electronic
Portion	Figure/Table
Number of figures/tables	14
Title of your thesis / dissertation	Brownian Dynamics Study on Ferrofluids using Iterative Constraints to Satisfy Maxwell's Equations
Expected completion date	Dec 2016
Estimated size (number of pages)	150
Requestor Location	Sean Dubina 810 S Clinton St CHICAGO, IL 60607 United States Attn: Sean Dubina
Billing Type	Invoice
Billing Address	Sean Dubina 810 S Clinton St CHICAGO, IL 60607 United States Attn: Sean Dubina
Total	0.00 USD

VITA

NAME: Sean Hyun Dubina

EDUCATION: B.S., Chemical Engineering, University of Maryland, College Park, Maryland, 2009

HONORS: Xerox Technical Minority Scholarship Recipient, 2015

       Charles E. and Joan M. Waggner Endowed Scholarship Recipient, 2008-2009

PROFESSIONAL American Institute of Chemical Engineers
MEMBERSHIPS: The Society of Rheology
       Graduate Association of Chemical Engineers

PUBLICATIONS: Dubina, S. H. and Wedgewood, L. E.: "Application of Nonuniform Magnetic Fields in a Brownian Dynamics Model of Ferrofluids with an Iterative Constraint Scheme to Fulfill Maxwell's Equations." In preparation.

       Dubina, S. H. and Wedgewood, L. E.: "A Brownian Dynamics Study on Ferrofluid Colloidal Dispersions using an Iterative Constraint Method to Satisfy Maxwell's Equations." *Physics of Fluids*, 28.7: 072001, 2016.

PRESENTATIONS: Dubina, S. H. and Wedgewood, L. E.: "A Brownian Dynamics Study on Ferrofluids under Nonuniform Magnetic Fields using an Iterative Constraint Method to Satisfy Maxwell's Equations." *AIChE 9th Annual Midwest Regional Conference*, University of Illinois at Chicago, 2017.

       Dubina, S. H. and Wedgewood, L. E.: "A Brownian Dynamics Study on Ferrofluid Colloidal Dispersions using an Iterative Constraint Method to Satisfy Maxwell's Equations." *AIChE 8th Annual Midwest Regional Conference*, Illinois Institute of Technology, 2016.

       Wedgewood, L. E. and Dubina, S. H.: "Application of Non-uniform Magnetic Fields on Ferrofluid Colloidal Dispersions using an Iterative Constraint Method: A Brownian Dynamics Study." *The Society of Rheology 86th Annual Meeting*, Philadelphia, PA, 2014.